Protein adsorption at functionalized surfaces

by

Christoph Bernhard

Dissertation zur Erlangung des Grades eines Doctor rerum naturalium (Dr. rer. nat.) der Fachbereiche:

08 - Physik, Mathematik und Informatik,

09 - Chemie, Pharmazie, Geographie und Geowissenschaften,

10 - Biologie und Universitätsmedizin

der Johannes Gutenberg-Universität Mainz.

Supervisors:

Declaration

I hereby declare that I wrote the dissertation submitted without any unauthorized external assistance and used only sources acknowledged in the work. All textual passages which are appropiated verbatim or paraphrased from published and unpublished texts as well as all information obtained from oral sources are duly indicated and listed in accordance with bibliographical rules. In carrying out this research, I complied with the rules of standard scientific practice as formulated in the statutes of Johannes Gutenberg-University Mainz to insure standard scientific practice.

(Christoph Bernhard)

This thesis is based on the following publications

Repelling and Ordering: The Influence of Poly(ethylene glycol) on Protein Adsorption.
C. Bernhard, S. J. Roeters, J. Franz, T. Weidner, M. Bonn and G. Gonella. Phys. Chem. Chem. Phys., 2017, 19, 29182. DOI: 10.1039/C7CP05445A

Interfacial Conformation of Hydrophilic Polyphosphoesters Affects Blood Protein Adsorption.
C. Bernhard, K. N. Bauer, M. Bonn, F. R. Wurm and G. Gonella. ACS Appl. Mater. Interfaces, 2019, 11, 1624. DOI: 10.1021/acsami.8b17146

Both poly(ethylene glycol) and poly(methyl ethylene phosphate) can guide specific protein adsorption
C. Bernhard, S. J. Roeters, K. N. Bauer, T. Weidner, M. Bonn, F. R. Wurm and G. Gonella. *In preparation*

Quantification of Protein Adsorption on Nanoparticle Surfaces
C. Bernhard, A. Bunn, M. Bonn, and G. Gonella. *In preparation*

Other publications

Surface Potential of a Planar Charged Lipid-Water Interface - What do vibrating plate methods, second harmonic and sum frequency measure?
L. B. Dreier, **C. Bernhard**, G. Gonella, E. H. G. Backus, M. Bonn. J. Phys. Chem. Lett., 2018, 9, 5685. DOI: 10.1021/acs.jpclett.8b02093

Abstract

The PhD work covered in this thesis, addresses protein adsorption on functionalized nanoparticle surfaces for biomedical applications. More specifically, we use two different approaches to study the protein adsorption: In the first part of this thesis, we use planar model systems at the air/water interface to mimic the nanoparticle surface and employ surface sensitive optical methods in reflection geometry to investigate them. Within this approach, we investigate the underlying protein-repelling mechanism of polymer materials and how these materials influence protein adsorption and orientation. However, studying nanoparticle surfaces *in situ* is quite challenging due to the turbidity of the particle dispersions and requires techniques such as nonlinear optical light scattering (NLS). To overcome this challenge, we develop a NLS method to investigate protein adsorption on nanoparticle dispersions *in situ* in the second part of this thesis.

In chapter 1, we introduce the scientific questions behind this study and discuss the theoretical background for this thesis. Afterward, we explain the experimental setups in detail together with additional information on data treatment in chapter 2.

In chapter 3, a model phospholipid monolayer system at the air/water interface is introduced to investigate the influence of poly(ethylene glycol) (PEG), the prototypical nanoparticle functionalization agent in biomedical applications, on the adsorption of bovine serum albumin (BSA) and human fibrinogen (Fbg). Here, we find that the interfacial PEG density influences both the amount and the orientational ordering of the adsorbed Fbg. Furthermore, comparison between the experimental observations with calculations indicates that the interfacial protein conformation is mainly preserved upon adsorption.

Following, in chapter 4, we explore the protein-repelling mechanism in polyphosphoester (PPE) polymers, a recently introduced class of materials to replace PEG in

protein-repelling functionalization. Thus, we use monolayer systems at the air/water interface consisting of three different PPE surfactants (obtained by modifying the polymers with a C18 alkyl chain) with slight variations in their monomer structure. By combining different surface sensitive techniques, we study the protein-repelling origin of these polymers towards human serum albumin (HSA) and Fbg.

Moreover, we compare PEG and a PPE polymer, namely poly(methyl ethylene phosphate) (PMEP), in their protein specific repellency and their influence on the interfacial protein orientation in chapter 5. We study the adsorption behavior of various proteins and find that the same proteins are repelled by both polymers. However, some proteins still adsorb and they appear to do so with a specific orientation. Additionally, the observations suggest that proteins are not repelled by the two materials based on the protein size and/or net surface charge.

Finally, in chapter 6, we describe the development of a non-resonant NLS method, called second harmonic light scattering, to study the adsorption of proteins on functionalized polystyrene (PS) nanoparticles. To this end, we vary the size and the functionalization of the PS nanoparticles and study the effects on the adsorption of blood proteins. We apply a modified Langmuir adsorption model to retrieve information on the amount of adsorbed protein per particle and the apparent binding constant. From that, we further calculate the Gibbs free adsorption energy upon protein adsorption.

Zusammenfassung

Diese Dissertation beschäftigt sich mit der Adsorption von Proteinen an der Oberfläche von funktionalisierten Nanopartikeln für biomedizinische Anwendungen. Dabei benutzen wir zwei unterschiedliche Modellansätze um Proteinadsorption zu untersuchen: Im ersten Teil dieser Arbeit benutzen wir planare Modelle an der Luft/Wasser Grenzfläche, welche die Oberfläche von Nanopartikeln nachbilden, und untersuchen diese mit Hilfe von oberflächensensitiven optischen Methoden in Reflektionsgeometrie. Hierbei ergründen wir den proteinabweisenden Mechanismus von polymerbasierten Materialien und erforschen wie diese das Adsorptionsverhalten und die Orientierung von Proteinen beeinflussen. Allerdings ist es grundsätzlich aufgrund der Trübung der Partikeldispersionen technisch sehr anspruchsvoll *in situ* Messungen an Nanopartikeloberflächen durchzuführen, weshalb spezielle Methoden wie beispielsweise nichtlineare Lichtstreuung dafür benötigt werden. Dementsprechend nutzen wir im zweiten Ansatz dieser Arbeit nichtlineare Lichtstreuung und entwickeln eine Methode, die es erlaubt Proteinadsorption an Nanopartikeln *in situ* zu erforschen.

Im ersten Kapitel stellen wir die wissenschaftlichen Fragestellungen vor und beschreiben die theoretischen Hintergründe, welche dieser Arbeit zugrunde liegen. Anschließend werden die experimentellen Aufbauten, sowie die Datenanalyse detailliert im zweiten Kapitel vorgestellt.

In Kapitel drei stellen wir ein Modell einer Lipidmonolage an der Luft/Wasser Grenzfläche vor, um den Einfluss von Polyethylenglycol (PEG), einer typischen proteinabweisenden Funktionalisierung in biomedizinischen Anwendungen, auf die Adsorption von Rinderserumalbumin und menschlichem Fibrinogen zu untersuchen. Dabei stellen wir fest, dass PEG an der Grenzfläche Einfluss sowohl auf die Menge, als auch die Orientierung des adsorbierten Fibrinogens hat. Darüber hinaus zeigt ein Vergleich von den experimentellen Beobachtungen mit theoretischen Berechnungen, dass die Proteinkonformation an der Grenzfläche bei der Adsorption erhalten bleibt.

Im Anschluss erforschen wir in Kapitel vier den proteinabweisenden Mechanismus von Polyphosphoester (PPE) Polymeren, einer kürzlich eingeführten alternativen Materialklasse für PEG als proteinabweisende Funktionalisierung. Dafür nutzen wir Monolagen an der Luft/Wasser Grenzfläche aus drei verschiedenen PPE Tensiden (die durch Modifikation der Polymere mit einer C18 Alkylkette hergestellt wurden), welche kleine Unterschiede in ihrer Monomerstruktur aufweisen. Durch Kombination von verschiedenen oberflächensensitiven Methoden erhalten wir Einblick in die proteinabweisende Wirkung dieser Polymere auf Rinderserumalbumin und Fibrinogen.

Darüber hinaus vergleichen wir in Kapitel fünf PEG mit einem PPE Polymer, namentlich Polymethylethylenphosphat (PMEP), in ihren Fähigkeiten spezifische Proteine abzuweisen und ihrem Einfluss auf die Orientierung der Proteine an der Grenzfläche. Wir erforschen das Adsorptionsverhalten unterschiedlicher Proteine und stellen fest, dass die gleichen Proteine von den beiden Materialien abgewiesen werden. Allerdings können manche Proteine dennoch unter einen gewissen Orientierung adsorbieren. Darüber hinaus deuten die Ergebnisse darauf hin, dass die Proteine nicht anhand ihrer Größe oder ihrer netto Oberflächenladung von den zwei Materialien abgewiesen werden.

Abschließend beschreiben wir in Kapitel sechs die Entwicklung einer Methode basierend auf nicht resonanter, nicht linearer Lichtsstreuung, namentlich zweite harmonische Lichtstreuung, um die Adsorption von Proteinen an funktionalisierten Polystyrol (PS) Nanopartikeln zu untersuchen. Hierfür nutzen wir Partikel mit verschiedenen Größen und Funktionalisierungen und untersuchen den Einfluss auf das Adsorptionsverhalten von Blutproteinen. Mit Hilfe eines modifizierten Langmuir Adsorptionsmodells erhalten wir Informationen über die Menge der adsorbierten Proteine pro Partikel und die scheinbare Bindungskontate, woraus wir wiederum die Gibbs-Energie berechnen können.

Contents

Contents

1 Introduction

1.1 Protein corona and protein-repelling approaches

Proteins are involved in many biological processes, such as transport of molecules, enzymatic reactions, and mechanical stabilization of the cytoskeleton.[1] Within these processes, proteins perform a huge variety of functions, which are enabled by their three-dimensional structure.[2] As a consequence, proteins and their interaction with their environment control big parts of our life. However, not all protein interactions are necessarily good. A prominent example of such undesirable interactions is *fouling*, where an accumulation of biomass occurs. Fouling can happen at many different surfaces and affects materials used for medical devices, pipelines, and ship hulls, to name a few.[3–5] In general, this process may involve many different species such as bacteria, diatoms, dust or organic liquids, but within this thesis, the focus is on proteins as adsorbates.[5]

Protein adsorption is of particular interest in the field of biomedical applications, where nanoparticles are commonly used as diagnostic agents and for drug delivery.[6–9] Nanoparticles offer two main advantages: they can be loaded with high drug dosage and can be engineered to offer site-specific targeting.[7–9] However, upon contact with a biological medium, the nanoparticle surface will rapidly be covered with proteins,[10] forming the so-called *protein corona* (as schematically represented in figure 1.1).[11–13] The protein corona has been shown to alter the targeting efficiency and effectively dictates the fate of the drug nanocarriers in the body.[14] This explains why the protein corona has been the focus of many studies in the past years.[8,11–13,15–21]

Furthermore, it has been found that nanoparticles with reduced protein adsorption possess so-called *stealth* properties: they show a lower unspecific cellular uptake, which in turn increases their blood circulation lifetime.[6,21] Consequently, in recent years, the holy grail of nano drugcarrier synthesis is not to prevent protein adsorption, but rather control of their surface properties such that the protein adsorption can be reduced and the biodistribution of the drug nanocarriers regulated.[9] This
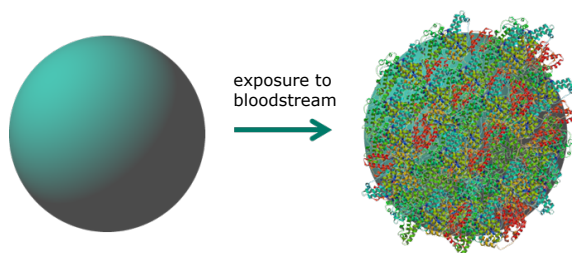
Figure 1.1: Scheme of protein adsorption onto the nanoparticle surface after injection into the bloodstream, giving rise to the formation of the protein corona.

is usually achieved by the use of protein-repelling materials and surface functionalizations,[*] exploiting self-assembled monolayers or polymer films of hydrophilic (uncharged) or zwitterionic materials.[22–24]

Among those materials, poly(ethylene glycol) (PEG) is by far most frequently used.[3,22,24] Even though the protein adsorption cannot be fully prevented using PEG, the nonspecific cellular uptake of the nanoparticles is effectively reduced.[6,25] In a recent publication, however, it was shown that the nonspecific cellular uptake for PEGylated particles is only lowered after exposure to blood plasma.[25] This indicates, that not the underlying functionalization is responsible for the stealth effect of the particles, but rather the proteins present at the surface. Moreover, the proteins appear to have a different abundance on the particles than in blood itself.

As a consequence, further improvement of the nanocarrier design, requires a better understanding of the protein-nanoparticle interaction. For this it is necessary to unravel the physico-chemical mechanisms which influence protein adsorption. Having this in mind, two key questions have to be answered: First, what is the driving mechanism through which protein adsorption is prevented? And second, which proteins adsorb and how do they adsorb? More specifically, what is their ordering and conformation on the surface? The aim of this PhD thesis is to garner an insight into these two questions on interactions of proteins with functionalized surfaces.

For PEG, steric repulsion[26–28] and hydration[29–31] have been proposed to be responsible for its protein-repelling properties. Therefore, it seems that the protein-repelling properties of a material are intrinsically linked, for instance, to the ability to tune the hydration and/or conformation of the polymer used for functionalization. These two

---

[*]Materials which prevent protein adsorption are often referred to as *antifouling*, *nonfouling*, *protein-resistent* or *protein-repelling* materials. Throughout this work, we will use the name protein-repelling materials.

parameters depend mainly on the chemical characteristics of the polymer, namely its interaction with the aqueous medium and the neighboring polymer chains and thus being able to control such chemistry becomes of paramount importance. However, these chemical modifications are very challenging using PEG, and a recent approach for protein-repelling functionalization of nanoparticles uses polyphosphoester (PPE) polymers instead.

PPEs offer the possibility to tune the polymer properties by changing the chemical structure and at the same time have shown protein-repelling properties comparable to those of PEG.[25,32–34] PPE-functionalized nanoparticles show reduced nonspecific cellular uptake, similar to PEGylated ones.[25] Additionally, chemical modification of the PPEs enables variations in hydrophilicity and degradation time of the polymers, which allows further fine-adjustment of the protein-repelling properties.[32,33]

Within this thesis, we investigate the influence of PEGylation on the protein adsorption behavior, and we compare the adsorption behavior of several blood proteins onto PEGylated surfaces with that on PPE functionalized surfaces. Moreover, we investigate the underlying microscopic protein-repelling mechanism of the PPE materials. The overarching aim is to reveal whether different functionalizations induce different adsorption behavior of the same proteins and when they do adsorb, to study the influence of the polymer on the protein ordering at the different surfaces.

1.2 Outline of this thesis

In chapter 1 the background concerning protein-repelling mechanisms of polymer films, protein structure, and nonlinear optical spectroscopy is described. Chapter 2 contains the description of the experimental setups, their calibration, and some information on the data treatment. In chapters 3-5, we study the protein adsorption behavior onto model surfaces, whereas in chapter 6 we move towards nanoparticle systems. In more detail, chapter 3 focuses on the influence of PEG on protein adsorption. More specifically, how the PEG concentration in a monolayer affects not only the amount of adsorbed protein, but also its ordering. Next, in chapter 4 various PPE surfactant monolayers are investigated in order to unravel their underlying protein-repelling mechanism. Chapter 5 focuses on the similarities and differences of a PPE and PEG by looking at the adsorption behavior of various blood proteins. Moreover, we investigate the ordering effect of the surfaces on the adsorbed proteins. In chapter 6, we use functionalized polystyrene particles instead of model planar sys-
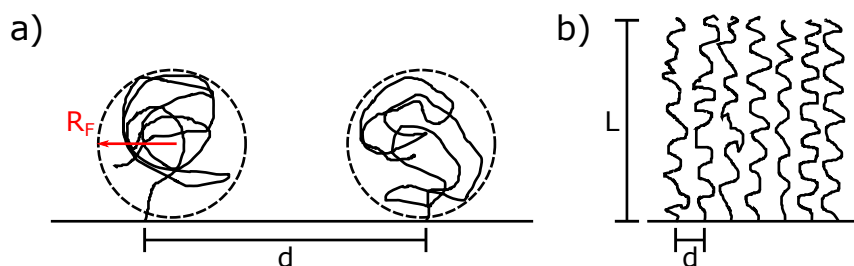
Figure 1.2: Scheme of the polymer confirmation for a grafted surface in the a) mushroom and b) brush regime.

tems. The aim of this chapter is to get an insight into the thermodynamic properties of protein adsorption using second harmonic light scattering. Finally, chapter 7 gives an outlook into potential future research regarding the protein corona.

1.3 Protein-repelling mechanisms and polymer conformation

PEG and zwitterionic materials have shown good protein-repelling properties in the past and are heavily used to prevent protein adsorption. As mentioned above, two possible mechanisms for their protein-repelling properties have been suggested: namely steric hindrance and hydration. For long PEG-brushes with sufficient packing density the protein-repelling properties were explained by steric repulsion.[26–28] Long PEG chains grafted to a surface form a flexible brush-like structure. As proteins approach the PEGylated surface, the PEG-chains are compressed thus decreasing their conformational freedom and therefore the entropy of the system. This, in turn, leads to an increase in free energy and consequently to protein repulsion. However, this cannot be transferred to short PEG chain monolayer model systems, as established in the early 1990s by the Whitesides group.[35,36] The Grunze group suggested, that, for short PEG-chain monolayers without conformational flexibility, the binding of interfacial water to the surface plays an important role for protein-repelling properties.[29,30] The hydration water molecules create an energetic and physical barrier and therefore render protein adsorption unfavorable. Furthermore, this group found that the protein-repelling behavior is highly dependent on the conformation of the PEG-chains[29] and showed that both the terminal and internal hydrophilicity of short PEG-chain monolayers influences the protein adsorption.[30] The same trend was also found for other hydrophilic monolayers on gold.[37] Altogether, these results from the Grunze group are in line with the findings from other groups, which have

suggested that other physical parameters such as hydrophilicity, electric neutrality, and hydrogen-bond donors/acceptors can play an important role on the protein-repelling properties of surfaces, for a variety of different materials.[31,38–40]

As pointed out already above, the conformation of the protein-repelling material influences the protein adsorption behavior. The conformation of long polymer chains depends mainly on the chain length and grafting density at the surface.[41–43] To get a grasp on the overall conformation of a polymer, usually two scenarios are considered: i) very low and ii) very high grafting densities. These regimes are also referred to as *mushroom* and *brush* regimes, respectively.[41,42,44,45] Theories from Alexander[46] and de Gennes[41] are used to describe the polymer chain properties. The mushroom regime of the polymer is relevant for low grafting densities, where the headgroups of the polymer are far away from each other and not in contact, as shown in figure 1.2a. In this case, the polymer chain behaves like a free polymer chain in solution (given a good solvent) and adopts a random configuration. The size of this polymer is then defined by the Flory radius R_F, which depends on the degree of polymerization N and the monomer unit size a:

$$R_F = aN^{3/5}. \tag{1.1}$$

This regime is usually reached, when the distance between two grafting sites d is bigger than the coil size of the polymer R_F. In the second case, where $d \ll R_F$, the headgroups of the polymer are relatively close to each other, interact, and the coils are stretched out, forming polymer brushes, as depicted in figure 1.2b. The thickness L of the brush depends, in this case, linearly on the degree of polymerization:

$$L = Na(\frac{a}{d})^{2/3}. \tag{1.2}$$

It has previously been observed that polymer brushes tend to be more effective in protein-repelling as compared to polymers in mushroom conformation.[44,47] The transition from mushroom to brush regime is not sharp and occurs as soon as the grafting density is high enough to induce overlap of the polymer coils. At this point the chains start to interact and stretch out. This intermediate state is relevant for the packing densities reported within this thesis.

1.4 Protein structure

Proteins carry out a manifold of tasks in every living system and are therefore of utmost importance for life. They are linear polymers, which consist of amino acid monomer units.[1] These amino acid monomer units are commonly linked in a trans-configuration via peptide bonds to polypeptides. Overall there are 20 different natural amino acids. These amino acids are usually divided into four different classes according to their side chains: hydrophobic, uncharged polar, negatively and positively charged. This variety of side chains of the amino acids is responsible for the diversity of protein functions. Every protein has a unique sequence of amino acids, which is called the *primary structure* of the protein. Within the protein, the peptide bonds of the amino acids form the main chain, or (amide) backbone. The peptide bonds in the backbone are planar, as they have a partial double-bond character. Consequently, the protein backbone is a sequence of rigid amide planes.[1,2] The side chains of the individual amino acids are arranged in an alternating pattern in order to reduce steric repulsion, as shown in figure 1.3. The peptide chain is limited in its rotation by repulsive interactions of the adjacent side chains. Therefore, for every backbone plane, there is only a range of possible dihedral angles φ and ψ, which ultimately are responsible for the folding of the protein. Depending on the amino acid sequence, the polypeptide chain can form several structural motifs with a well-defined folding, which is usually stabilized through hydrogen bonding.[1,2] These structural motifs of amino acid residues in close proximity are called the *secondary structure* of the protein. Pauling and coworkers were the first to postulate the existence of those structures in 1951.[48,49] The most common secondary structures in proteins are α-helices, β-sheets and coils. These structural motifs are briefly described below.

Some amino acid sequences can form rod-like structures, such as α-helices. An example of a α-helix is shown in figure 1.4a. In this case, the twist angle for several subsequent peptide planes is constant ($\varphi, \psi \sim -57°, -47°$). Theoretically, the main chain rotation can be right-handed or left-handed. However, since the right-handed rotation is energetically more favorable (collisions of the side chains are less likely) all α-helices found in nature are right-handed.[1,2] A full turn of the α-helix corresponds to 3.6 amino acid residues. The helix is further stabilized by hydrogen bonds in the main chain. Every nth C=O group of the backbone forms a hydrogen bond with the $(n + 4)$th N-H group of the polypeptide chain.[1,2] The side chains of the
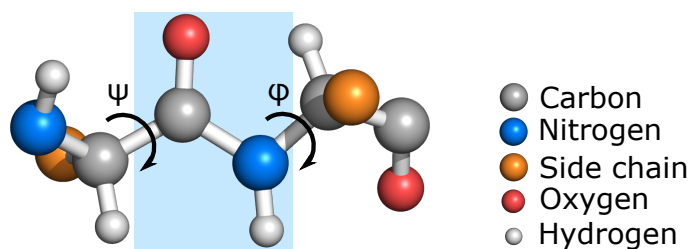
Figure 1.3: Illustration of the peptide bond. The backbone plane is highlighted in light blue, and the two rotation angles φ and ψ are explicitly indicated.

polypeptide point to the outside of the helix, in order to reduce steric repulsion. In β-strands, the main chain of the polypeptide can be fully stretched ($\varphi, \psi \sim -120°, -120°$), as shown in figure 1.4b.[50] Within a β-strand there is no stabilization from hydrogen bonds in the main chain. However, neighboring β-strands can align in either a parallel or an antiparallel manner. Here, hydrogen bonds are formed between the C=O group of one strand and the N-H group of another strand. Together, the bonded β-strands form the β-pleated sheet.[50] In a parallel β-sheet the individual strands have the same orientation from N-terminus to C-terminus, while in antiparallel β-sheets the strands have the opposite orientation.

The last major class of secondary structures are summarized as *coils* or *loops*. Oftentimes they are labeled as random coils or unstructured, because they have no regular repetitive structure. In contrast to α-helices and β-sheets the peptide bonds are not involved in the hydrogen bonding within the protein. However, these structures provide flexibility to the protein and are often important for interactions with other molecules, such as water, ligands or other proteins.[2,50]

The spatial assembly of secondary structures within the whole protein is called the *tertiary structure* of the protein. This overall arrangement is determined by several interactions, such as hydrophobic interactions of the side chains, hydrogen bonds, or disulfide bonds.

Last but not least, proteins have a *quarternary structure*. In fact, proteins can consist of several polypeptide chains, which are subunits of the whole protein. The spatial arrangement of these subunits is commonly referred to as the quarternary structure of the protein.[1,2]

Spectroscopic techniques which measure molecular vibrations are frequently used to investigate the structure of proteins. Prominent examples of such techniques are in-
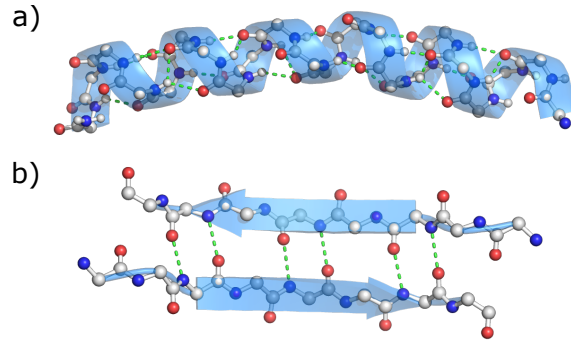
Figure 1.4: Examples of polypeptide main chains forming (a) an α-helical and (b) an antiparallel β-sheet structure. The hydrogen bonds are highlighted with the green dashed line.

frared (IR) absorption spectroscopy and Raman scattering.[51–54] The characteristic vibrations of individual chemical species allow for example insights in the structure of the proteins. Any nonlinear molecule has 3N-6 vibrational modes (linear molecules have 3N-5), or normal modes. Figure 1.5 shows the vibrational modes for the example of a water molecule. The actual frequency at which the vibrational mode appears depends strongly on the mass of the involved atoms, as well as the strength of the chemical bonds involved. These modes can be described as harmonic oscillations with the frequencies ν_i:

$$\nu_i = \frac{1}{2\pi} \cdot \sqrt{\frac{k_i}{m_i^*}}. \tag{1.3}$$

With the force constant k_i and the reduced mass m_i^*.[54] Here, the force constant reflects the strength of the chemical bond. For proteins, the mode of interest is often the amide I band, which appears at around 1600-1700 cm^{-1}. The main contribution of this vibrational mode comes from the C=O stretching resonance of the peptide carbonyl group in the protein backbone. This normal mode is very insensitive to the side chain of the amino acid residue, while it is at the same time influenced by the secondary structure of the protein backbone.[52] Thus, this vibration is commonly used for structural analysis of proteins. The resonance frequency of this vibrational mode is shifted due to coupling of vibrations of neighboring peptide groups.[52,54] Generally, the resonances of α-helical structures is close to the one of unstructured conformations at $\sim$1650 cm^{-1}, while for β-sheets the mode is split due to the coupling in a main band at $\sim$1620 cm^{-1} and a sideband at $\sim$1690 cm^{-1}.[53]
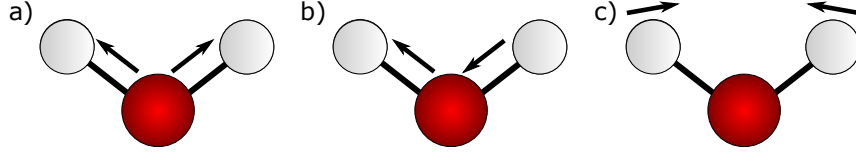
Figure 1.5: Scheme of the normal modes of a water molecule: a) Symmetric stretching, b) asymmetric stretching, and c) bending mode.

1.5 Nonlinear optical spectroscopy

Light-matter interactions are frequently used to gain insight into the properties of matter, by matching the frequency of electromagnetic waves with quantum transitions of the material. In this way it is possible to probe, for example, spin transitions, molecular rotations, molecular vibrations, and electronic transitions. As mentioned before, the aim of this thesis is to investigate the adsorption behavior of proteins at functionalized surfaces. Unfortunately, for linear spectroscopic methods, the signal which is generated in the bulk of the material dominates over the surface contributions, simply due to the amount of probed molecules. This limitation can be overcome to some extent using for instance total internal reflection IR spectroscopy. However, a class of techniques that are intrinsically surface-specific are second-order optical spectroscopies. These are, under the electric-dipole approximation, surface-specific due to the symmetry selection rules.[55–57] Therefore, within this thesis, we chose sum-frequency generation (SFG) and second harmonic generation (SHG) processes to study proteins at interfaces.

Generally, light-matter interactions are described by Maxwell's equations:[†]

$$\nabla \cdot \mathbf{D} = \rho$$
$$\nabla \cdot \mathbf{B} = 0$$
$$\nabla \times \mathbf{E} = -\frac{\partial}{\partial t}\mathbf{B} \tag{1.4}$$
$$\nabla \times \mathbf{H} = \mathbf{j} + \frac{\partial}{\partial t}\mathbf{D}$$

[†]Please note that the Maxwell's equations in this thesis are written using the SI-convention. Furthermore, for simplicity and to improve the readability, vector values are written as bold letters where the symbols for the spatial and temporal dependencies are omitted, e.g., $\mathbf{E}(r,t) = \mathbf{E}$. Tensors are represented with the superscript $\leftrightarrow$ symbol.

where $\mathbf{D}$ is the electric displacement field, $\mathbf{B}$ the magnetic flux density, $\mathbf{H}$ the magnetic field, and $\mathbf{E}$ the electric field. The two fields $\mathbf{D}$ and $\mathbf{B}$ take the dielectric and magnetic properties of the material into account. This is shown in the constitutive relations:

$$\mathbf{D} = \epsilon_0 \mathbf{E} + \mathbf{P}$$
$$\mathbf{B} = \mu_0 \mathbf{H} + \mathbf{M}. \tag{1.5}$$

Here, $\mathbf{P}$ and $\mathbf{M}$ depict the macroscopic polarization and magnetization of the material, respectively. Furthermore, ϵ_0 is the permittivity of free space and μ_0 the vacuum permeability. In optics, it is usually assumed that the electromagnetic waves travel in regions of space without free charges ($\rho = 0$) and currents ($\mathbf{j} = 0$). Moreover, the material is assumed to be nonmagnetic ($\mathbf{M} = 0$). With these assumptions, we can obtain the so-called *wave equation* by taking the curl of the curl-$\mathbf{E}$ Maxwell equation and simplifying:

$$\nabla^2 \mathbf{E} - \frac{1}{c^2} \frac{\partial^2}{\partial t^2} \mathbf{E} = \frac{1}{\epsilon_0 c^2} \frac{\partial^2}{\partial t^2} \mathbf{P} \tag{1.6}$$

with c the speed of light in vacuum, which is defined as $c = (\epsilon_0 \mu_0)^{-1/2}$. Here, the polarization $\mathbf{P}$ on the right-hand side of the wave equation acts as the source of radiation and represents the response of the material to the applied electric field $\mathbf{E}$. $\mathbf{P}$ will then generate an electric field $\mathbf{E}$ oscillating at the same frequency. The polarization is defined as the dipole moment per unit volume and can be described with a power series:[55,56]

$$\mathbf{P} = \epsilon_0 (\overleftrightarrow{\chi}^{(1)} \mathbf{E} + \overleftrightarrow{\chi}^{(2)} \mathbf{E}^2 + \overleftrightarrow{\chi}^{(3)} \mathbf{E}^3 + \dots)$$
$$= \mathbf{P}^{(1)} + \mathbf{P}^{(2)} + \mathbf{P}^{(3)} + \cdots \tag{1.7}$$

Where $\overleftrightarrow{\chi}^{(1)}$ is the linear susceptibility, while $\overleftrightarrow{\chi}^{(2)}$ is the second-order and $\overleftrightarrow{\chi}^{(3)}$ the third-order nonlinear susceptibility of the material. The polarization can act as a source of new radiation components (see equation 1.6) and is therefore important for the description of nonlinear optical phenomena. In most cases, the nonlinear contributions of the polarization become significant only for high amplitudes of the electric field.[55,56] This is the main reason why nonlinear optical phenomena were only systematically studied after the invention of the laser, which enables the generation of such strong fields. For example, the first SHG process was observed in 1961 by Franken et al.[58] following the first laser invented by Maiman[59] a year earlier. The

first experimental SFG spectra were published by Zhu et al. in 1987.[60] The physical origin of both SHG and SFG processes will be explained in the following.

1.5.1 Sum-frequency generation spectroscopy

We consider two different incident fields with amplitudes $\mathbf{E}_1$, $\mathbf{E}_2$ and frequencies ω_1, ω_2, respectively. The field incident on a medium can then be written as:

$$\mathbf{E} = \mathbf{E}_1 \cos(\omega_1 t) + \mathbf{E}_2 \cos(\omega_2 t). \tag{1.8}$$

The second-order nonlinear polarization according to equation 1.7 can then be written as:

$$\mathbf{P}^{(2)} = \epsilon_0 \overleftrightarrow{\chi}^{(2)} \mathbf{E}^2 = \epsilon_0 \overleftrightarrow{\chi}^{(2)} [\mathbf{E}_1 \cos(\omega_1 t) + \mathbf{E}_2 \cos(\omega_2 t)]^2 =$$

$$= \frac{1}{2} \epsilon_0 \overleftrightarrow{\chi}^{(2)} [\mathbf{E}_1^2 + \mathbf{E}_2^2 + \mathbf{E}_1^2 \cos(2\omega_1 t) + \mathbf{E}_2^2 \cos(2\omega_2 t)+ \tag{1.9}$$

$$+ 2\mathbf{E}_1\mathbf{E}_2 \cos((\omega_1 + \omega_2)t) + 2\mathbf{E}_1\mathbf{E}_2 \cos((\omega_1 - \omega_2)t)].$$

Consequently, the second-order nonlinear polarization $\mathbf{P}^{(2)}$ can give rise to several physical processes. The first two terms describe static fields (also called optical rectification), the next two terms are fields at twice the incoming frequencies $2\omega_1$ and $2\omega_2$ (SHG). The last two terms describe a field at the sum-frequency of the incoming fields (SFG) and another field at the difference-frequency of the incoming fields (difference frequency generation, DFG). The SFG component of the second-order nonlinear polarization can then be extracted and is given by:

$$\mathbf{P}^{(2)}_{SFG} = \epsilon_0 \overleftrightarrow{\chi}^{(2)} \mathbf{E}_1 \mathbf{E}_2 \cos((\omega_1 + \omega_2)t). \tag{1.10}$$

Experimentally the other second-order nonlinear contributions from equation 1.9 can be eliminated as they have different emission frequencies and directionality. In the case of vibrational sum-frequency generation spectroscopy, it is common to use a visible (VIS) and an IR beam as incoming electric fields. The signal becomes strongly enhanced, if the frequency of the IR beam is resonant with a vibrational mode of the sample molecules.[57] As shown in equation 1.6 the nonlinear polarization acts as a source for an electromagnetic wave at the sum of both frequencies and the intensity of that field is measured in the SFG spectroscopy experiments:

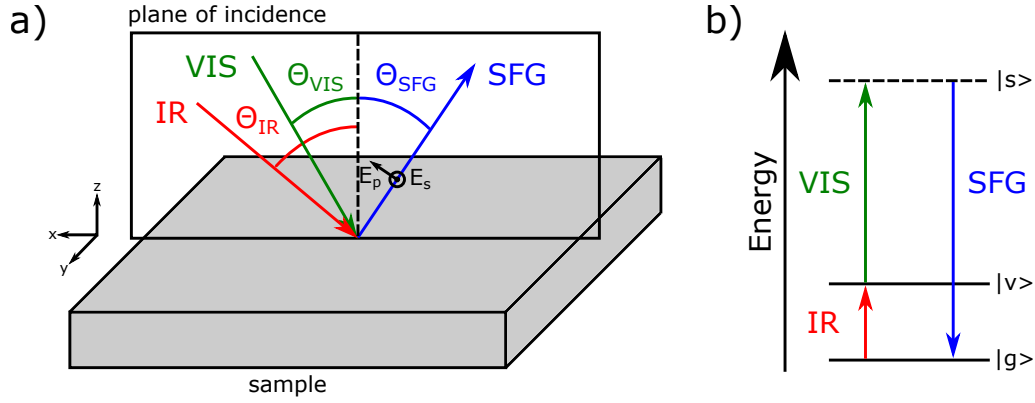$$\mathbf{I}_{SFG} \propto |\overleftrightarrow{\chi}^{(2)}|^2 \mathbf{I}_{VIS} \mathbf{I}_{IR} \tag{1.11}$$

Figure 1.6: a) Schematics of the sum-frequency generation process and the *p*- and *s*-polarization according to the plane of incidence. b) Energy level diagram for vibrational sum-frequency generation, where |g> depicts the ground state, |v> the vibrationally excited state and |s> a virtual state.

where $\mathbf{I}_{VIS}$ and $\mathbf{I}_{IR}$ depict the intensities of the incoming VIS and IR beams. The generated coherent SFG signal is emitted in the phase-matching direction, with the phase-matching condition being:

$$\mathbf{k}_{SFG} = \mathbf{k}_{VIS} + \mathbf{k}_{IR} \tag{1.12}$$

Here, $\mathbf{k}_i$ are the wavevectors of the SFG, VIS and IR fields, respectively.[55]
The second-order susceptibility links the incident electric fields to the induced polarization in the medium, thus, $\overleftrightarrow{\chi}^{(2)}$ is a third-rank tensor consisting of 27 cartesian components. Considering these cartesian components of the tensor, equation 1.10 can be rewritten as:

$$\mathbf{P}^{(2)}_{i,SFG} = \epsilon_0 \chi^{(2)}_{ijk} \mathbf{E}_{j,1} \mathbf{E}_{k,2} \tag{1.13}$$

As mentioned above, second-order nonlinear optical processes are surface selective. More specifically, these processes are forbidden in centrosymmetric media, but can occur whenever the symmetry is broken. In centrosymmetric media the nonlinear optical susceptibility $\overleftrightarrow{\chi}^{(2)}$ is invariant for the inversion transformation, where all coordinates are replaced with their negative counterparts:

$$\chi^{(2)}_{ijk} = \chi^{(2)}_{-i-j-k} \tag{1.14}$$

However, under electric dipole approximation the susceptibility tensor transforms as the threefold product of the coordinates, therefore it changes sign upon inversion:

$$\chi^{(2)}_{-i-j-k} = (-1)^3 \chi^{(2)}_{ijk} \tag{1.15}$$

Both equations 1.14 and 1.15 can only be simultaneously fulfilled for a vanishing $\chi^{(2)}_{ijk}$.[55–57] Therefore, in a bulk with inversion symmetry no SFG signal is generated. But the symmetry is necessarily broken at the interface and SFG signal can be produced. Moreover, the molecules at the surface must achieve an overall net polar orientation in order to generate SFG signal, as the responses from molecules with opposing orientation cancel each other out.

For most isotropic media the number of unique and non-vanishing tensor elements can be reduced to four, simply by applying symmetry operations:[55,57] $\chi^{(2)}_{zxx}(= \chi^{(2)}_{zyy})$, $\chi^{(2)}_{xzx}(= \chi^{(2)}_{yzy})$, $\chi^{(2)}_{xxz}(= \chi^{(2)}_{yyz})$ and $\chi^{(2)}_{zzz}$. By selecting different polarization combinations of the SFG signal, as well as VIS and IR beams, it is thus possible to probe different components of the $\chi^{(2)}_{ijk}$ tensor. Table 1.1 summarizes the different tensor elements accessible with different polarization combinations. In this notation *p*-polarization represents light polarized parallel to the plane of incidence and *s*-polarization light polarized perpendicular (from the German word *senkrecht*) to the plane of incidence (see Figure 1.6). By probing different polarization combinations, it is possible to infer the molecular orientation at interfaces.[57,61,62]

The nonlinear optical susceptibility $\chi^{(2)}_{ijk}$ is a macroscopic property of the material

Table 1.1: Possible polarization combinations and the probed $\chi^{(2)}_{ijk}$ tensor elements. The polarization combinations are denoted with increasing wavelength in order SFG, VIS and IR.

Polarization combination	Probed $\chi^{(2)}_{ijk}$ elements
ssp	$\chi^{(2)}_{yyz}$
ppp	$\chi^{(2)}_{zzz},\ \chi^{(2)}_{zxx},\ \chi^{(2)}_{xzx},\ \chi^{(2)}_{xxz}$
sps	$\chi^{(2)}_{yzy}$
pss	$\chi^{(2)}_{zyy}$

including information on the molecular hyperpolarizability β_{abc}. $\chi_{ijk}^{(2)}$ reflects a summation over all molecules in a given volume, as shown in equation 1.16.

$$\chi_{ijk}^{(2)} = \frac{N}{\epsilon_0} \sum_{abc} \langle R(\psi)R(\theta)R(\phi)\beta_{abc}\rangle \tag{1.16}$$

$R(\psi), R(\theta)$, and $R(\phi)$ are rotational matrices which convert the molecular frame to the experimental laboratory frame, where N is the number of molecules per unit volume and the $\langle\rangle$ brackets indicate an ensemble average. An expression for β_{abc} can be derived with quantum mechanics using perturbation theory.[55,57] However, a simplification can be used when the frequency of the IR laser beam is close to a vibrational transition:

$$\beta_{abc} = \frac{1}{2\hbar}\frac{M_{ab}A_c}{\omega_\nu - \omega_{IR} - i\Gamma} \tag{1.17}$$

where M_{ab}, A_c, ω_ν, ω_{IR} and Γ^{-1} stand for the Raman transition moment, infrared transition moment, the vibrational transition frequency, the frequency of the incoming IR beam and the relaxation time of the vibrational state, respectively.[57,63] Therefore, in vibrational SFG spectroscopy, in order to obtain a resonant SFG signal the transition must be both Raman and IR allowed.

Additionally, the experimentally observed $\overleftrightarrow{\chi}^{(2)}$ contains not only resonant contributions (R) from the probed molecules, but also a nonresonant contribution (NR):

$$\overleftrightarrow{\chi}^{(2)} = \overleftrightarrow{\chi}_R^{(2)} + \overleftrightarrow{\chi}_{NR}^{(2)} \tag{1.18}$$

The nonresonant background can be attributed to electronic transitions and electric quadrupole contributions.[56,64,65] The NR background is therefore especially strong for metallic surfaces, but also contributes for dielectric media. However, the nonresonant background is to a great extent frequency-independent. Since the measured SFG intensity is proportional to the square of the sum of the individual $\overleftrightarrow{\chi}^{(2)}$ components, interference can occur. Because of this, quantitative information from the SFG spectra can only be retrieved by fitting of the spectra. The most common approach to fit experimental results uses Lorentzian lineshapes (as shown in equation 1.17) for the resonant contributions and an additional frequency-independent nonresonant contribution.
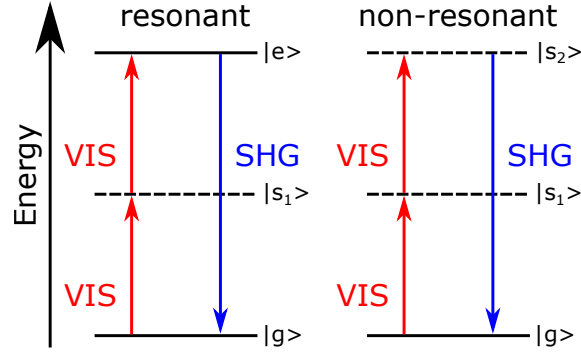
Figure 1.7: Energy level diagram for the two most commonly used SHG excitation schemes. The diagram on the left shows the case where the SHG is in resonance with an electronic state |e>. On the right hand side, both interactions with the fundamental beam are non-resonant. |s₁> and |s₂> are virtual states and |g> is the ground state of the system.

1.5.2 Second harmonic generation

As shown in the previous section, SHG is also a second-order nonlinear process, similar to SFG. More specifically, SHG represents a special case of SFG, where the two incoming beams have the same frequency (and usually same direction). Consequently, the nonlinear polarization from equation 1.9 reduces to:

$$\mathbf{P}^{(2)} = \epsilon_0 \overset{\leftrightarrow}{\chi}^{(2)} \mathbf{E}^2 = \epsilon_0 \overset{\leftrightarrow}{\chi}^{(2)} [\mathbf{E}_1 \cos(\omega_1 t) + \mathbf{E}_1 \cos(\omega_1 t)]^2$$
$$= 2\epsilon_0 \overset{\leftrightarrow}{\chi}^{(2)} [\mathbf{E}_1^2 + \mathbf{E}_1^2 \cos(2\omega_1 t)] \tag{1.19}$$

Thus, only optical rectification and second-harmonic generation occur. Apart from that, SHG follows the same selection rules as SFG. SHG can be used in both a resonant and a non-resonant scheme, as shown in figure 1.7. Usually, the fundamental beam is in the VIS range and either the SHG is in resonance with an electronic state or both interactions with the fundamental beam are non-resonant. In contrast to SFG spectroscopy, resonant SHG is often used to probe electronic transitions rather than vibrational transitions, in particular for biological molecules.[66–68] The non-resonant version, on the other hand, is mainly used to probe interfacial potentials.[67,69–71] Additionally, the $\overset{\leftrightarrow}{\chi}^{(2)}$ tensor is further simplified as compared to the SFG case, due to the fact that $\chi_{ijk}^{(2)}$ is equal to $\chi_{ikj}^{(2)}$.
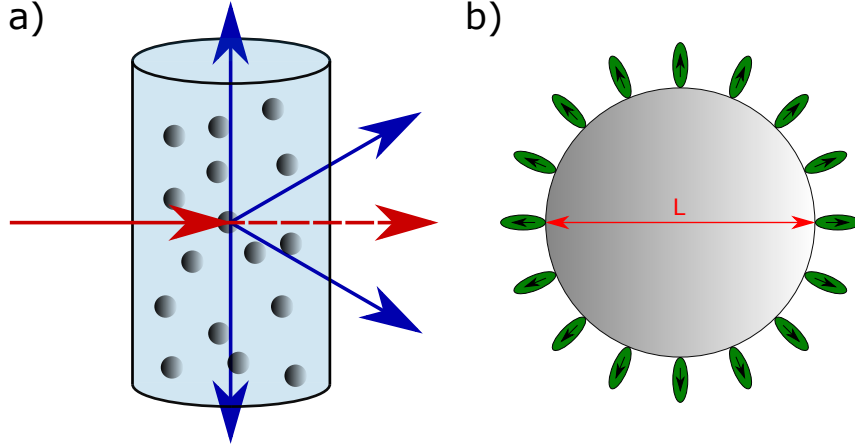
Figure 1.8: a) Scheme of SHS generation from a particle dispersion. b) Molecules adsorbed to the surface of a particle. The distance between two molecules with opposite orientation is L.

1.5.3 Second harmonic light scattering

Second harmonic light scattering combines the nonlinear optical process of SHG with light scattering and therefore enables the investigation of colloidal systems such as, e.g., nanoparticle dispersions. Figure 1.8a shows a scheme for SHS generated by a particle dispersion. As stated above, it is generally assumed that (under electric-dipole approximation) centrosymmetric media do not generate second harmonic light from bulk. However, SHG can still be experimentally observed from isotropic media, which can have two different origins. In order to illustrate this, we consider two scattering objects separated by a distance L, which have opposite orientation (see Figure 1.8b). The resulting detected second harmonic field $\mathbf{E}_{det}(2\omega)$ depends on the phase mismatch $\Delta k \cdot L$:[72,73]

$$\mathbf{E}_{det}(2\omega) \propto \mathbf{E}_i(2\omega)[1 - e^{i\Delta k \cdot L}] \tag{1.20}$$

with

$$\Delta k = k(2\omega) - 2k(\omega) = \frac{2\omega}{c}[n(2\omega) - n(\omega)] \tag{1.21}$$

where $\mathbf{E}_i(2\omega)$ is the second harmonic field generated by the individual scattering objects. If the distance between the objects is small compared to the incident wavelength ($L \ll \lambda$, for visible light this is roughly $L \leq 10\ nm$), the phase difference becomes negligible ($\Delta k \cdot L \approx 0$) leading to an effectively centrosymmetric media.[72–74]

In this case, symmetry selection rules predict a vanishing SHG from the system. However, fluctuations in the molecular orientation and/or density can break this symmetry and produce incoherent second harmonic light, which is referred to as hyper-Rayleigh scattering (HRS).[75] Consequently, HRS is a bulk signal and scales linearly with the number density of molecules N:

$$\mathbf{I}_{HRS}(2\omega) \propto N\beta_{ijk}^2 \,\mathbf{I}(\omega)^2 \tag{1.22}$$

With increasing distance between the objects, the overall phase difference cannot be neglected anymore ($\Delta k \cdot L \neq 0$) and coherent SHS signal is produced, which scales with the square of the number density of molecules N^2:

$$\mathbf{I}_{SHS}(2\omega) \propto N^2\beta_{ijk}^2 \,\mathbf{I}(\omega)^2 \tag{1.23}$$

Thus, centrosymmetric structures with length scales on the order of the wavelength or some fractions of it can generate strong SHS signal.[72–74] First experimental proof of SHS from centrosymmetric polystyrene (PS) particles in an isotropic medium was reported by Wang et al. in 1996.[72]

The resulting detected scattering pattern of a particle in the far-field is determined by the phase difference of the emitted beams on the particle. Therefore, the overall scattering response is dependent on several parameters, such as the size, shape, refractive index of the material, and the beam geometry.[74] Moreover, the measured SHS intensity is not probing single particles, but reflects an average of all particles in the focal volume and if working in dilute conditions the signal will scale linearly with the particle density. Figure 1.9 shows an example of scattering patterns from PS particles with different diameters. As can be seen in the figure, the scattering pattern changes with the size of the particles and the maximum scattering intensity is shifted closer to the forward direction (0°) for bigger particle diameters.

There are several theoretical models, which describe the nonlinear optical properties of nanoparticles.[74] The most commonly used are the nonlinear Mie theory and Rayleigh-Gans-Debye (RGD) approximation.[74,76–82] For PS particles in water, as they are used within this thesis, the RGD approximation is most often used. In this theory, it is assumed, that the amplitude, direction and phase of the light beam are not changed upon crossing the particle/liquid interface. It has the advantage, that it can be used for particles of any shape. However, this assumption only works for systems where the refractive index difference between particles and liquid is small
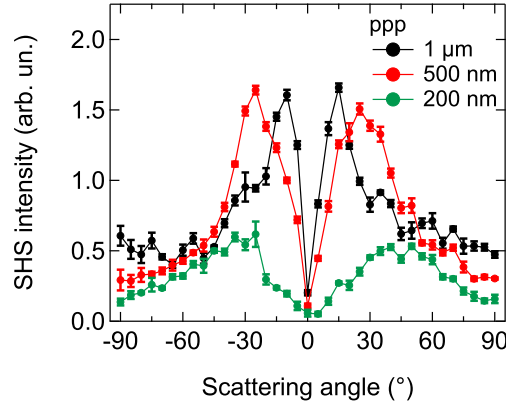
Figure 1.9: SHS scattering patterns detected in the far field in *ppp* polarization combination of PS particles with diameters of 1 μm (black), 500 nm (red) and 200 nm (green) in H_2O.

and the particles are not too big. For PS particles in water this approximation cannot be used for particles bigger than $R = 100$ nm.[79]

2 Experimental methods

This chapter describes the experimental methods used during this thesis. First, in chapter 2.1, the vibrational SFG spectroscopy setup is explained. Afterward, section 2.2 describes the experimental SHS setup. Brewster angle microscopy and surface tension measurements are explained in sections 2.3 and 2.4, as they were frequently used throughout the work reported in this thesis.

2.1 SFG spectroscopy

The SFG spectroscopy experiments in this thesis were all performed on a homebuilt setup, which is described in the following paragraphs. Generally, for vibrational SFG spectroscopy a visible (VIS) and an infrared (IR) laser pulse are overlapped temporally and spatially at the interface of interest. A scheme of the experimental SFG spectroscopy setup is shown in figure 2.1. A Ti:Sapphire oscillator (MaiTai, Spectra-Physics, USA) provides seed pulses at 800 nm wavelength, with a pulse duration of ∼40 fs. The seed pulses are further amplified with a regenerative Ti:Sapphire amplifier (Spitfire Ace, Spectra Physics, USA), which is pumped by an external Nd:YLF laser (Empower, Spectra-Physics, USA). The amplified VIS pulses have an average pulse energy of ∼5 mJ and a repetition rate of 1 kHz. A beam splitter (BS) splits the VIS pulses in two parts. The first part is guided through an etalon (SLS Optics Ltd., Isle of Man) to create narrow-band VIS pulses with an FWHM of ∼15 cm^{-1}. The other fraction of the VIS pulses is used to pump an optical parametric amplifier (TOPAS-C, Light Conversion, USA) with a subsequent difference frequency generation scheme. This produces tunable broadband IR laser pulses in the mid-IR range of ∼3-8 μm with average pulse energies of 2-5 μJ. The polarization state and power at the sample stage can be controlled individually for both VIS and IR beam via half-waveplates (WP) and polarizers (P). Unwanted harmonic frequencies or signal/idler contributions are filtered out by bandpass and longpass filters (F). Afterward, the beams are focused on the sample with plano-convex lenses (L)
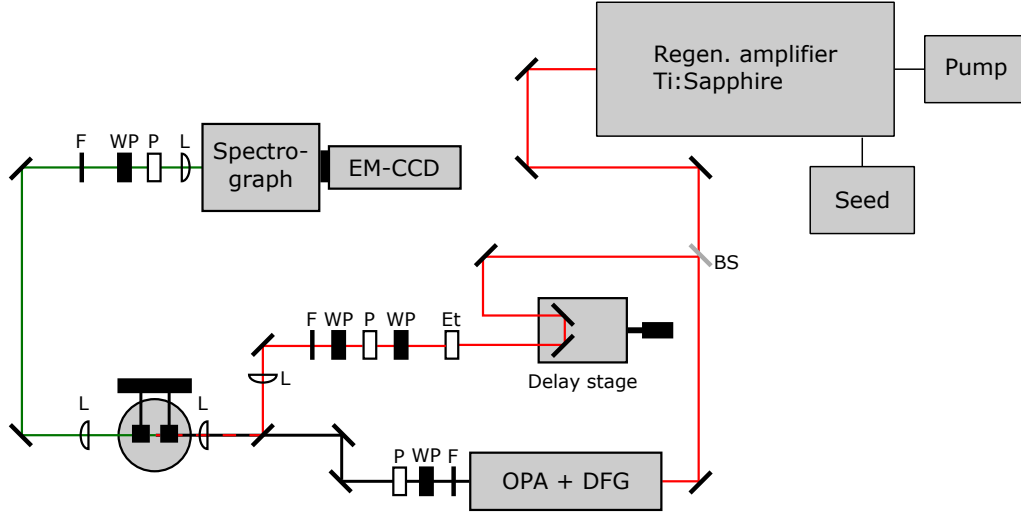
Figure 2.1: Overview of the experimental SFG spectroscopy setup and the optical components: (BS) Beam splitter, (Et) Etalon, (WP) half-waveplate, (P) polarizer, (F) filter, (L) lens. The SFG, VIS, and IR beam paths are depicted in green, red and black, respectively.

(f_{IR} = 5 cm, f_{VIS} = 20 cm). The spatial overlap of VIS and IR is established with mirrors, while the temporal overlap can be adjusted with a delay stage, to match the optical path lengths of VIS and IR beams.

The emitted SF signal from the sample is then collimated with a lens and guided through a shortpass filter. The polarization state of the detected SF signal is again controlled with a half-waveplate and a polarizer. Finally, the SF signal is focused onto the entrance slit of a spectrograph (Acton SpectraPro 300i, Princeton Instruments, USA) and detected with an electron-multiplied charge-coupled device camera (Newton EMCCD 971P-BV, Andor Technology Ltd, UK).

The setup is placed in a box, which can be flushed with nitrogen, in order to prevent unwanted IR-absorption from ambient water and carbon dioxide. This is done for all measurements performed in the amide I and free OH region. Moreover, the box reduces detection of ambient light. Apart from that, fractions of scattered VIS light could still reach the detector and generate a background signal. Therefore, all spectra are background corrected, by subtracting the signal, when the IR beam is blocked, while VIS is incident on the sample. A further correction step is done by normalizing the SFG data from the sample onto the spectral IR intensity profile. This is done by measuring the nonresonant SFG signal from either a z-cut quartz crystal or a gold reference and dividing the obtained sample signal by the

reference signal. All measurements in this thesis are taken at a room temperature of $(22 \pm 1)°C$. The Teflon coated trough for monolayer measurements is constantly rotated during the measurements to prevent laser-heating-induced displacement of the surfactants at the surface.[83]
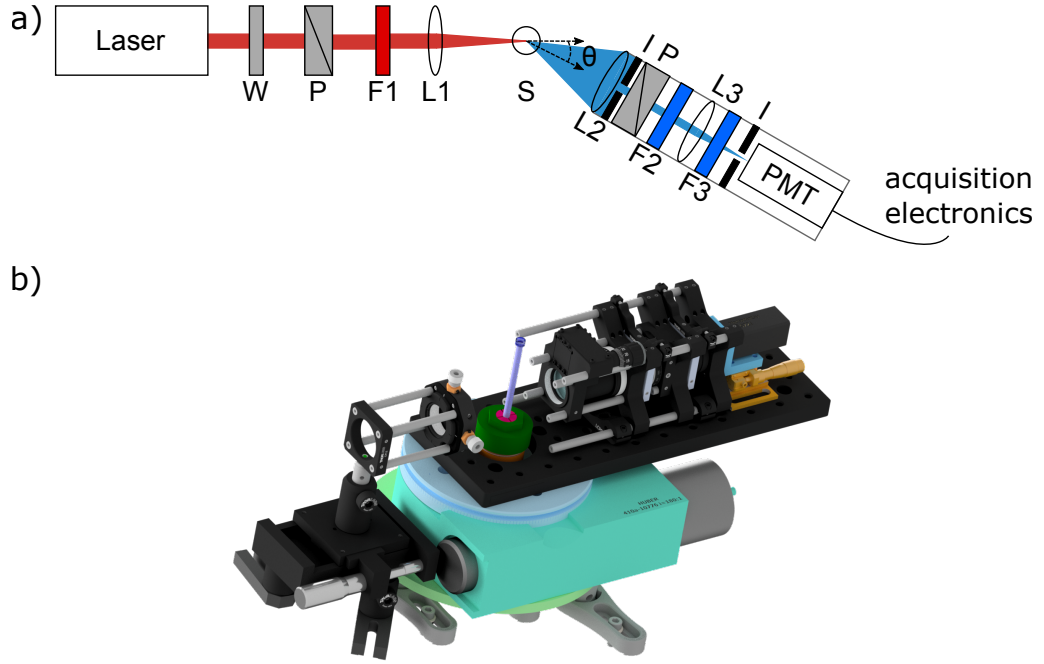
2.2 SHS Setup

Figure 2.2: (a) Overview over the optical components of the SHS setup: (W) quarter-wave plate, (P) polarizer, (F1) long pass filter, (L1 and L3) focusing lens, (L2) collimation lens, (F2 and F3) bandpass filters, (I) iris diaphragm. The fundamental beam is shown in red, scattered second harmonic light in blue. (b) 3D image of the SHS setup showing the sample and the SH detection path located on a rotational goniometer stage. This rendered image was kindly provided by M.-J. van Zadel.

The SHS setup described in this chapter was built during this work and is similar to the ones in Refs. [74, 84, 85]. Figure 2.2 shows a scheme of the experimental scattering setup. The source for the fundamental laser beam at 1028±5 nm is a mode-locked Yb:KGW (ytterbium-doped potassium gadolinium tungstate) laser (Pharos-15W, Light Conversion, Lithuania) with a tunable repetition rate and output power. Throughout the experiments in this thesis, the repetition rate is set to

1 MHz, and if not stated otherwise, the fundamental beam power is set usually in the range of 80-150 mW before the sample. The polarization of the fundamental beam is controlled with a Glan-Taylor polarizer (GT10-B, Thorlabs, USA). Beforehand the fundamental beam is circularly polarized by a quarter-wave plate (AQWP10M-980, Thorlabs, USA), so that the laser power after the polarizer is independent of the polarization state. A long pass filter (FEL850, Thorlabs, USA) filters out higher harmonic frequency contributions from the laser. Afterward, the beam is focused with a plano-convex lens (f = 7.5 cm) in the sample cell. Throughout this work three different cells are used for the various experiments: (i) cylindrical glass cuvettes (4.2 mm inner diameter, high precision cylindrical glass cuvette, LS instruments, Switzerland), (ii) cylindrical cuvettes (7.5 mm inner diameter, Hellma Analytics, Germany) and (iii) fluorescence cells (inner dimensions 10x10 mm^2, Hellma Analytics, Germany). The beam waist in the focus is $\sim$33 μm with a corresponding Rayleigh length of $\sim$0.83 mm. A collimation lens (f = 5.0 cm) collects the generated scattered SH light from the sample. An iris diaphragm and a Glan-Taylor polarizer (GT10-A, Thorlabs, USA) are used to determine the solid angle and the polarization over which the signal is integrated. If not stated otherwise, the acceptance angle in this work is set to $\sim$3.4 degrees for angle-dependent SHS measurements, while it is $\sim$13.5 degrees for SHS experiments at a constant detection angle. Two band-pass filters (ET525/50, Chroma, USA and FGB39, Thorlabs, USA) filter out the fundamental laser beam before detection. Finally, the signal is focused onto a photomultiplier tube (PMT, H10721-20, Hamamatsu, Japan). The generated electrical pulse from the PMT is further amplified (HFAC-26dB, Becker & Hickl, Germany) and sent to a time-correlated single photon counting board (TimeHarp Nano 260, Picoquant, Germany). To improve the signal to noise ratio, the signal is manually gated in the measurement software with a gate width of $\sim$12.5 ns. The detection path of the setup is mounted on a rotational goniometer stage (410A, Huber Diffraktionstechnik, Germany), which enables the collection of scattering patterns in the horizontal plane from -110 degrees to +110 degrees, where 0 is the direction of the fundamental.

SHS data treatment and general assumptions

The particle surface is not the sole signal source which is detected, but other sources could contribute to the emission at 2ω: the particle bulk, the HRS from the solvent

and that from the molecule/protein of interest. Thus, we measure for each sample the emission at 2ω from the bare NPs at the concentration of interest. We also measure mole dependently the HRS from the molecules/proteins and that from the solvent. For our specific systems under study, it turned out that no signal can be detected from the proteins in solution without particles and thus these two contributions will be disregarded for the further thesis. To correct for the incoherent HRS contributions, the obtained data are normalized in two ways: First, the HRS from the pure solvent is subtracted from the sample signal. Afterward, the sample signal is divided by the HRS signal of bulk water in *sss* polarization combination, to correct for angular differences of the focal volume. Thus, the normalized SH signal $SHS_{pii}(\theta)$ is obtained via equation 2.1:

$$SHS_{pii}(\theta) = \frac{I_{pii}(\theta) - HRS_{S,pii}(\theta)}{HRS_{H_2O,sss}(\theta)} \qquad (2.1)$$

Here, *ii* represents the incoming polarization (either *p* or *s*), $I_{pii}(\theta)$ is the *p*-polarized intensity generated by the sample, $HRS_{S,pii}(\theta)$ the *p*-polarized HRS intensity of the bulk solution in absence of particles and $HRS_{H_2O,sss}(\theta)$ is the HRS signal of water in *sss* polarization combination.

In addition, for all SHS measurements performed in this thesis, we apply the following assumptions for the data treatment:

a) The particle density is low enough so that multiple scattering is negligible. This assumption is verified later in this thesis for the 100 nm PS particles by the results in chapter 6, figure 6.4b.

b) Liquids are spatially isotropic and only produce incoherent HRS.

c) We consider the medium of our samples as lossless and dispersion-free. This means that Kleimann symmetry can be applied to the samples of interest.[55]

2.3 Brewster angle microscopy

Brewster angle microscopy (BAM) is a surface-sensitive method to study the morphology and layer thickness of monolayers at the air/water interface. The working principle of this technique is based on Brewster's law and was first established in 1991.[86,87] The reflection of light at a plane interface between two media with refractive indices n_1 and n_2 depends on the angle of incidence θ_i and the polarization
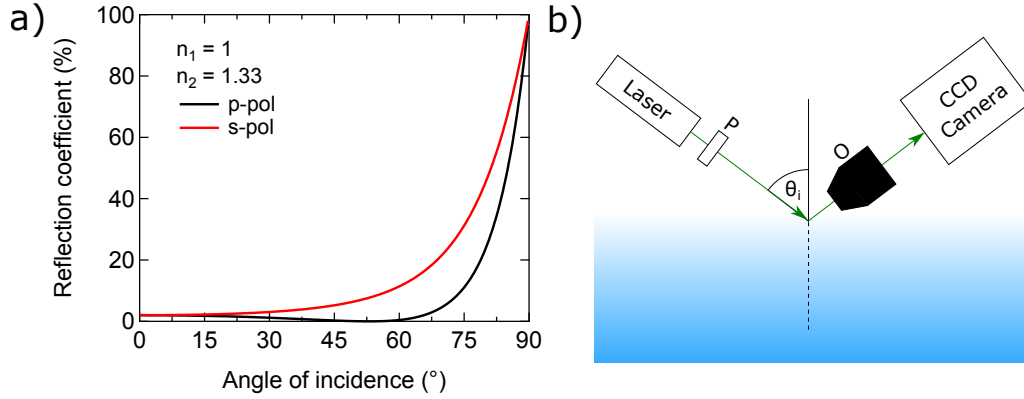
Figure 2.3: a) Reflectance of *p*-polarized (black) and *s*-polarized (red) light at the air/water interface as a function of the angle of incidence ($n_1 = 1$, $n_2 = 1.33$). b) Scheme of the BAM setup: The laser beam is *p*-polarized by a polarizer (P) and hits the interface with incidence angle $\theta_i = \theta_B$. For the air/water interface the Brewster angle is for $\lambda = 658$ nm $\sim$53.1°. The reflected light is collected with an objective (O) and detected with a CCD camera.

state of the light beam. The Fresnel reflection coefficients r_p and r_s are given in equations 2.2 and 2.3, respectively.

$$r_p = \frac{n_2 cos(\theta_i) - n_1 cos(\theta_t)}{n_2 cos(\theta_i) + n_1 cos(\theta_t)} \tag{2.2}$$

$$r_s = \frac{n_1 cos(\theta_i) - n_2 cos(\theta_t)}{n_1 cos(\theta_i) + n_2 cos(\theta_t)} \tag{2.3}$$

θ_t stands for the angle of the refracted wave with respect to the surface normal, and can be obtained using Snell's law ($n_1 sin(\theta_1) = n_2 sin(\theta_2)$). Figure 2.3a shows the calculated reflectance for $R_p = |r_p|^2$ and $R_s = |r_s|^2$ for *p*- and *s*-polarized light, for the water/air interface. As can be seen, the reflectance of the *p*-polarized light vanishes under illumination at the so called Brewster angle $\theta_B = arctan(n_2/n_1)$ (53.1° for the air/water interface using $\lambda = 658$ nm). However, in practice the reflectance at the Brewster angle is not zero, due to the nonvanishing thickness, roughness, or anisotropy of the interface.[88]

Figure 2.3b shows a typical scheme of a BAM setup. In BAM, the incidence angle of the laser beam is set to the Brewster angle, so that the reflectivity of the air/plain water interface is minimized. The reflected light from the surface is then collected with an objective and detected with a CCD camera. In presence of a surfactant
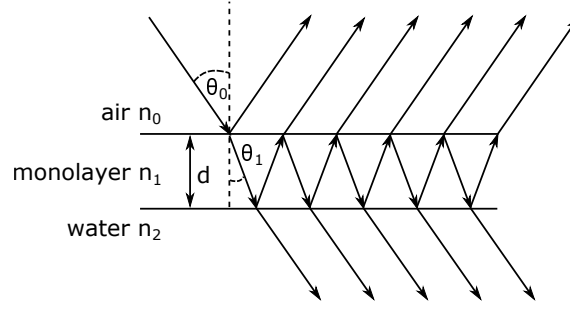
Figure 2.4: Reflection and transmission of a plane wave by a triple layer model consisting of ambient air, the monolayer of interest and a water subphase.

monolayer at the air/water interface, the interfacial parameters, such as for example layer thickness and refractive index, are altered, which leads to an increased reflectivity. This enables the imaging of the monolayer at the air/water interface. For very thin interfacial layers ($d << \lambda$), the reflected intensity scales approximately to leading order as the square of the layer thickness d.[88,89] In this work, a commercial BAM setup (Accurion, EP3 BAM, Germany) with a laser wavelength of $\lambda = 658$ nm and a maximum power of 50 mW is used for all measurements. For imaging, the signal is collected with a $10\times$ objective.

Setup calibration and determining the relative monolayer thickness

The reflected intensity of a monolayer-covered surface is determined by the optical thickness of the applied thin film. In order to determine the layer thickness of a thin film with BAM, we use a simple three layer model from Ref. [89] as depicted in Figure 2.4. Briefly, the reflected light intensity I as a function of the thickness d of the monolayer is given by the equation 2.4:

$$I = |r_p|^2 = C \cdot d^2 \tag{2.4}$$

Where r_p is the Fresnel reflection coefficient for p-polarized light and C is a constant. r_p is given by equation 2.5.

$$r_p = \frac{r_{01} + r_{12}e^{-i2\beta}}{1 + r_{01}r_{12}e^{-i2\beta}} \tag{2.5}$$

with

$$\beta = 2\pi(\frac{d}{\lambda})n_1 \cos(\theta_1) \tag{2.6}$$

$$r_{01} = \frac{n_1 \cos(\theta_0) - n_0 \cos(\theta_1)}{n_1 \cos(\theta_0) + n_0 \cos(\theta_1)} \tag{2.7}$$

$$r_{12} = \frac{n_2 \cos(\theta_1) - n_1 \cos(\theta_2)}{n_2 \cos(\theta_1) + n_1 \cos(\theta_2)} \tag{2.8}$$

Here λ is the wavelength of light, n_i and θ_i are the refractive index and angle of incidence with respect to the surface normal, respectively. The indices 0, 1 and 2 refer to air, surfactant monolayer and water, respectively. Calibration of the
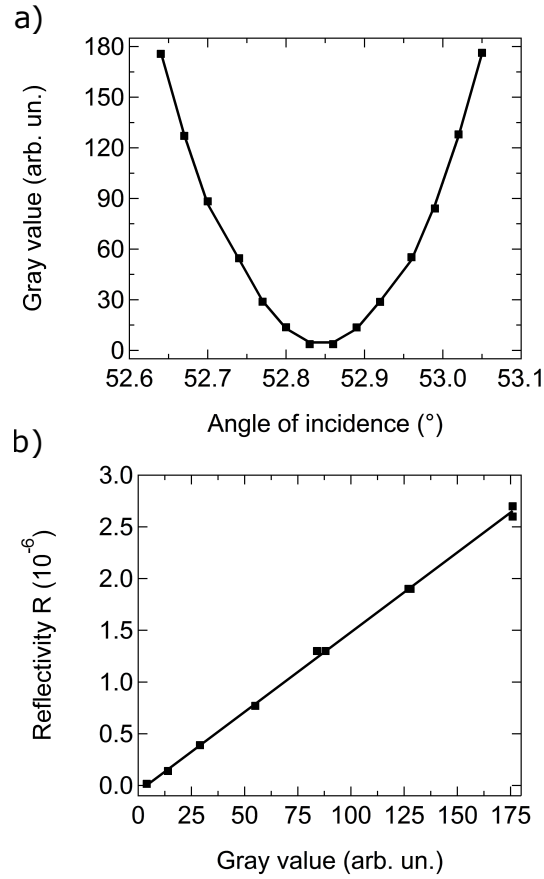

Figure 2.5: Calibration curves of the BAM setup on a pure water subphase. a) Detected gray levels at the CCD camera upon variation of the angle of incidence around the Brewster angle. b) The theoretical relative reflectivity of the pure water surface as calculated by the Fresnel coefficient as a function of the measured gray level values from a).

BAM setup enables correlating the measured gray level value to the reflectivity of the sample. The calibration procedure is adapted from earlier publications.[90–92] In the first step, the exact Brewster angle is determined by measuring the reflected light intensity from a pure water subphase for different angles of incidence (relative to the surface normal) close to the theoretical Brewster angle ($\sim$53.1°). Due to alignment tolerances of the setup, the actual measured Brewster angle can differ from the theoretical expected value (Figure 2.5 a). Now, the relative reflected light intensity from the pure water surface is calculated with the Fresnel formulas and can be plotted as a function of the measured gray level values (Figure 2.5 b). This results in a linear calibration curve of the setup, which enables to link measured gray level values to the actual reflectivity of the surface. Thus, the integrated intensity from BAM pictures of the different monolayers directly returns, through Eq. 2.4, a quantity that is proportional to the square of the monolayer thickness.

2.4 Film pressure measurements

Surface tension measurements are commonly used to determine the film pressure π of Gibbs and Langmuir monolayers and to study the adsorption of molecules on monolayers and model membranes. In this thesis, it is used to track the adsorption of blood proteins onto functionalized monolayers. In general, the surface tension of a liquid is defined by the work dW which has to be done in order to increase the surface area of the liquid by dA. This work is proportional to the surface tension γ:[93,94]

$$dW = \gamma \cdot dA \tag{2.9}$$

When a monolayer is present at the surface of the subphase, the film pressure π of the monolayer is defined as the difference between the surface tension of the subphase γ_0, in the absence of the monolayer, and the surface tension γ in the presence of the monolayer:

$$\pi = \gamma_0 - \gamma \tag{2.10}$$

The film pressure measurements in this thesis are performed with a DeltaPi tensiometer (Kibron, Finnland), using the so-called Wilhelmy method. The probe is a small diameter (0.51 mm) special alloy wire, which is placed partly into contact

with the aqueous subphase, as shown in figure 2.6. The force acting on the wire is given by equation 2.11.

$$F = F_g + \gamma \cdot p \cdot \cos(\theta_c) \tag{2.11}$$

With the gravitational attraction F_g, the perimeter p of the wire and the contact angle θ_c. This formula is further simplified, by assuming complete wetting ($\theta_c = 0°$) of the wire. For the film pressure measurements, the experimental setup is first calibrated to the plain aqueous subphase, and the film pressure is subsequently calculated from the changes in surface pressure after applying the monolayer.[93,94]
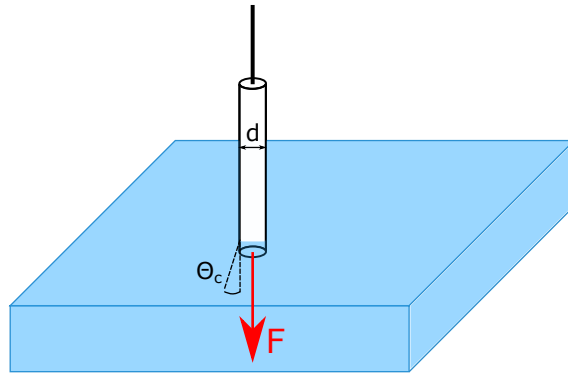

Figure 2.6: Scheme of the surface tension measurements using the Wilhelmy method with a wire probe.

3 Repelling and Ordering: The Influence of Poly(ethylene glycol) on Protein Adsorption

Author Contributions: C.B., G.G. and M.B. designed the research project. C.B. performed the SFG, BAM and surface pressure experiments. J.F. assisted with the SFG measurements. S.J.R. and T.W. performed the calculations for the protein SFG spectra. All authors discussed the results and wrote the paper.

3.1 Abstract

Development of new materials for drug delivery and biosensing requires the fine-tuning of interfacial properties. We report here the influence of the poly(ethylene glycol) (PEG) grafting density in model phospholipid monolayers on the adsorption behavior of bovine serum albumin and human fibrinogen, not only with respect to the amount of adsorbed protein, but also its orientational ordering on the surface. As expected, with increasing interfacial PEG density, the amount of adsorbed protein decreases up to the point where complete protein repellency is reached. However, at intermediate concentrations, the net orientation of adsorbed fibrinogen is highest. The different proteins respond differently to PEG, not only in the amount of protein adsorbed but also in the manner that proteins adsorb. The results show that for specific cases, tuning the interfacial PEG concentration allows to guide the protein

adsorption configuration, a feature sought after in materials for both biosensing and biomedical applications.

3.2 Introduction

Whenever materials come in contact with biological systems, adsorption of proteins on their surface occurs. Therefore, in the development of drug nanocarriers, biosensors or anti-biofouling coatings, protein resistant surfaces play an important role to prevent nonspecific protein adsorption.[4,6,22,95,96] A common approach to obtain protein repellent, or so-called anti-fouling, coatings relies on the use of hydrophilic or zwitterionic materials.[23,31,97] Among these materials poly(ethylene glycol) (PEG) is a widely used and thoroughly studied hydrophilic protein repelling polymer.[26] Surfaces that make use of different PEGylation strategies, namely block copolymers,[24,28,98] self-assembled monolayers on gold[29,35,36] or phospholipids,[44,99,100] have been widely used to control, localize or entirely prevent protein adsorption. In the past, various factors, such as PEG grafting density, chain length, and its molecular conformation, have been studied with respect to their influence on the protein adsorption behavior.[29,30,36,47,101–104] While for many biomaterial applications a completely protein-repelling surface is often desired, for biosensing and drug delivery, it is more important to control the type of protein adsorbed and to tune the surface orientation in the bound state.[29] It has been shown recently that controlled binding of proteins on nanoparticle surfaces can help to prevent nonspecific cellular uptake and prolong the blood circulation lifetime of drug nanocarriers.[25] The ability to also order the adsorbed proteins might then favor the uptake by the targeted cells. Naturally, also in the case of biosensors, having access to specific binding sites of the protein is desirable.[105]

In this work, we study the influence of PEG concentration in mixed 1,2-dimyristoyl-sn-glycero-3-phosphoethanolamine (DMPE) and 1,2-dimyristoyl-sn-glycero-3-phosphoethanol-amine-N-[methoxy(polyethylene glycol)-2000] (DMPE-PEG2000) phospholipid monolayers on both the amount and the orientational ordering extent of the adsorbed proteins. We have chosen bovine serum albumin (BSA) and human fibrinogen (Fbg) as model systems to track the impact of PEG density on the order of large proteins. BSA and Fbg have been chosen as representative proteins in the field because of their relevance for biomedical research. Albumin is the most abundant among blood proteins, and fibrinogen plays an important role in blood

coagulation and appears to have a higher affinity to the surface of PEGylated drug nanocarriers.[25] The two proteins are very different in terms of size (BSA ∼66 kDa and Fbg ∼340 kDa) and (tertiary) structure (globular for BSA vs. rod-like for Fbg). The results presented here show that the PEG density not only affects the amount of adsorbed protein but in the case of Fbg also strongly influences the protein orientation at the surface.

In our study, we employ vibrational sum-frequency generation (SFG) spectroscopy to directly probe the protein backbone at the surface. SFG spectroscopy is well suited to study proteins at interfaces.[62,106,107] In the past SFG spectroscopy has frequently been used to investigate the hydration of PEGylated surfaces in presence or absence of proteins in the subphase.[108–115] Moreover, there are several in situ studies probing the water structure or protein backbone in the amide I region after adsorption on hydrophobic or hydrophilic surfaces.[106,116–122] Understanding the interaction of proteins with PEGylated surfaces plays an important role, e.g. for the functionalization of nano drugcarriers or the design of biosensing devices. However, despite the broad use of PEG little is known about the molecular adsorption geometry of proteins at the surface. Here, we use surface sensitive SFG spectroscopy to *in vivo* study the protein adsorption on PEGylated surfaces with respect to both the amount of adsorbed protein and its orientational ordering. More generally this study highlights how a suite of different techniques can be used to obtain information on the adsorption of proteins on (soft) surfaces quite often a challenging issue because of their small number compared to the ones present in bulk solution.

3.3 Experimental

In our experiments, we employ a reflection geometry setup as shown in Figure 3.1a in combination with a translating Langmuir trough[123] to collect the amide I SFG signal from the proteins adsorbed at the monolayer/PBS (phosphate buffered saline solution) interface. All spectra in this work are taken in *ssp* (*s*-polarized SFG signal, *s*-polarized VIS-beam and *p*-polarized IR-beam) polarization combination with an accumulation time of 10 minutes. Contemporaneously with the SFG measurements surface pressure measurements are performed.

The phospholipid monolayer at the air/PBS interface is composed of DMPE and DMPE-PEG2000 as shown in Figure 3.1b. Both phospholipids are used as received, and a Langmuir trough is used to prepare the monolayers. Phospholipid mixtures
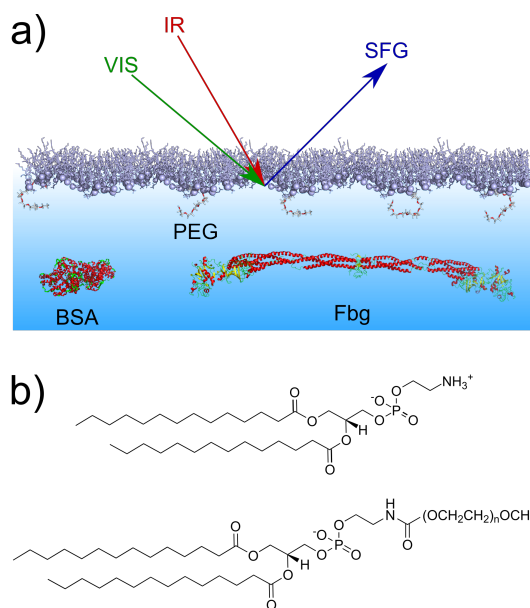
Figure 3.1: a) Scheme of the reflection SFG experiment at the phospholipid monolayer. b) Chemical structures of (top) DMPE and (bottom) DMPE-PEG2000 ($n = 45$).

containing 0, 1, 5 and 10 mol% DMPE-PEG2000 have been prepared. The lipids are spread at the air/PBS interface and compressed to an initial surface pressure of 20 mN m^{-1}. From a comparison of the pressure-area isotherms (Fig. 3.7 in section 3.6) with literature[124–126] it is possible to conclude that at this value of the surface pressure the monolayers are in the liquid-condensed phase. BSA, Fbg and PBS tablets are used as received. All samples have been prepared in PBS solutions (pH 7.4) and all the experiments conducted at a temperature of $22 \pm 1\,°C$. Further details on the Materials and methods can be found in the supplementary information in section 3.6.

3.4 Results and discussion

For the SFG experiments, the lipids mixtures containing 0-10 mol% of DMPE-PEG2000 are spread on a PBS subphase and compressed. After an initial surface pressure of 20 mN m^{-1} is reached, SFG spectra are collected, to study the order of the lipid monolayer, as shown in Figure 3.2. A peak at $\sim$1735 cm^{-1}, assigned to the carbonyl stretch vibration of the lipids, is present in all spectra. In general, the SFG signal intensity depends not only on the number of probed molecules but also on
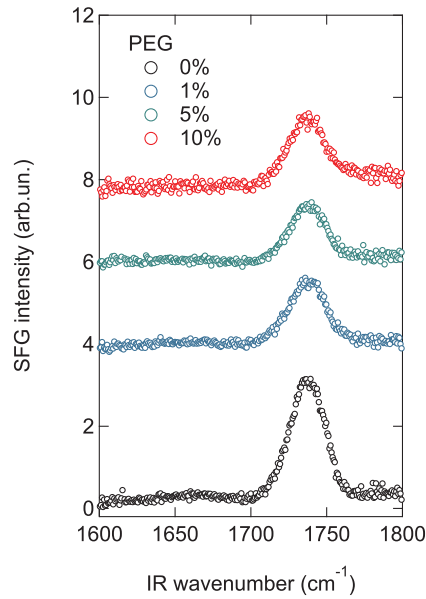
Figure 3.2: SFG spectra of different mixed phospholipid monolayers at a surface pressure of 20 mN m^{-1} in the carbonyl stretch region. The DMPE-PEG2000 content in the monolayers varies between 0 and 10 mol%. For clarity, the individual spectra are offset on the y-axis.

their orientation.[57] As can be seen in Figure 3.2, the intensity of this peak decreases upon addition of DMPE-PEG2000 into the monolayers. Since in the present study the average area per molecule, and therefore the total number of probed molecules, in the monolayers is kept constant, the observed decrease suggests that an increase in the concentration of PEGylated lipids induces orientational disorder in the monolayer that in turn results in a decrease in the SFG signal. This increased disorder can be caused by PEG-lipid, PEG-water and/or PEG-PEG interactions. In fact, it is known that these interactions roughen the monolayer surface, especially when PBS is present in the subphase,[127] as also apparent in Brewster angle microscopy images of the monolayers (see Fig. 3.8 in section 3.6).

Figure 3.3 shows the SFG spectra of the different monolayers with subphases containing different protein solutions, namely BSA (panel a) and Fbg (panel b). SFG spectra in the absence of proteins (open symbols), recorded immediately prior to injecting a small volume of a highly concentrated protein solution into the subphase, are shown for comparison. The final protein concentration in the subphase amounts to 0.1 mg ml^{-1}. From Figure 3.3a it is apparent that, in absence of PEG in the
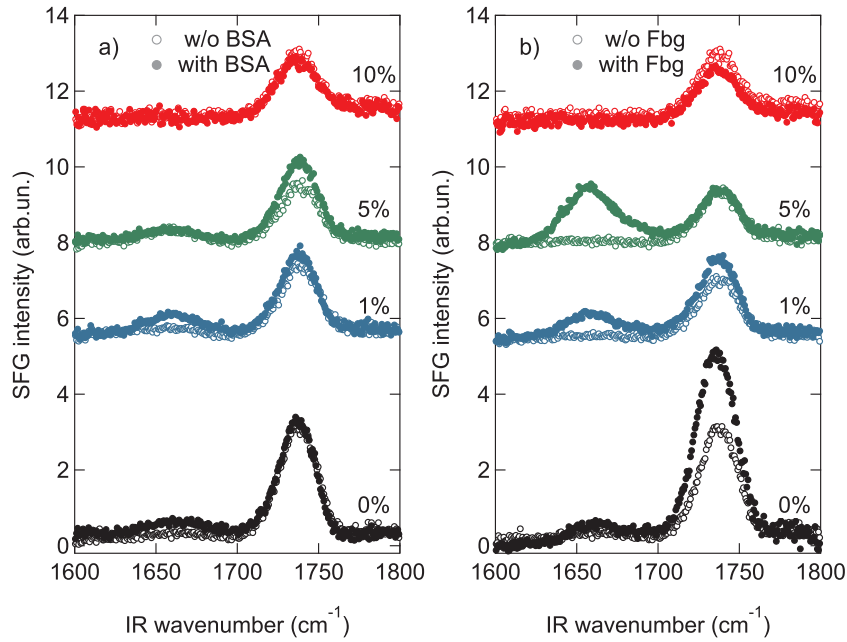
Figure 3.3: SFG spectra (offset on the y-axis for clarity) in the amide I region before (open symbols) and after (filled symbols) injection of a) BSA and b) Fbg (0.1 mg ml^{-1}) at mixed DMPE:DMPE-PEG2000 monolayers with different PEG concentrations.

monolayer, an additional peak centered at ∼1660 cm^{-1} arises in the spectrum in presence of BSA (for a zoom-in see Fig. 3.9 in section 3.6). This peak - related to the α-helical components in the protein secondary structure[128] - is a clear indication that the protein adsorbs to the monolayer.[129] This amide I peak is also clearly visible with 1 mol% PEG present in the monolayer. Further increase of the PEG concentration in the mixed monolayer to 5 or 10 mol%, completely suppresses the amide I signal of BSA, as expected for fully PEGylated surfaces. The actual PEG grafting density needed in order to obtain a completely protein repelling surface can actually differ depending on the PEG chain length. It has been shown in literature, that the PEG size strongly influences its conformation for a given grafting density.[29,44,47] As theoretically and experimentally shown, longer PEG chains are already protein resistant at lower mole fractions.[26,29] For our study we chose an intermediate chain length, namely PEG2000, since it is commonly used for nanoparticle functionalization and in PEGylated liposomes.[25,100,130] The small SFG signal present in the amide I region for the mixed monolayer with 5 mol% DMPE-PEG2000, is a feature sometimes observed, even in the absence of proteins, and is most likely caused by
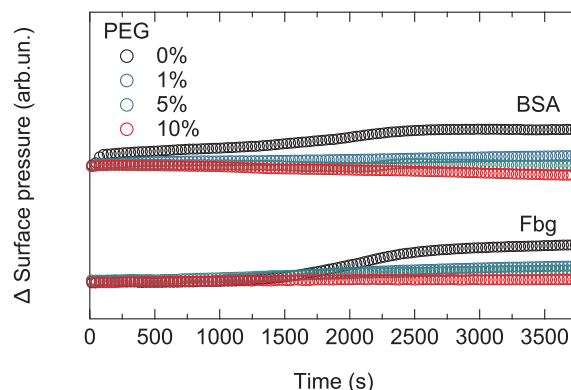
Figure 3.4: Change of surface pressure after injection of BSA (top) and Fbg (bottom) into the subphase at time t = 0 s of the corresponding mixed monolayer with PEG concentrations from 0 to 10 mol% (offset on the y-axis for clarity).

a contribution from the water bending mode. However, below we will consider differential spectra with and without protein so that this is not a problem (for further details see section SFG measurements and Fig. 3.10 in section 3.6).

SFG is very sensitive to protein symmetry and orientation and it is important to test whether the observed SFG signal changes are due to changes in the amount or the orientation of proteins at interfaces. To independently confirm BSA binding, we measure the surface pressure simultaneously with the SFG spectra, as shown in Figure 3.4. While SFG reports on both amount and order, surface pressure is primarily sensitive to the amount and can be used to disentangle the SFG information related to orientation. The relative increase in surface pressure after the injection of BSA into the subphase diminishes gradually when the number of PEGylated phospholipids present in the monolayer increases. This indicates, in line with the reported properties of PEG, that less BSA adsorbs to the surfaces with higher PEG content.[35,36,47]

While the surface pressure for Fbg (Figure 3.4) behaves similarly to that observed for BSA, SFG spectra reveal a different trend when Fbg interacts with the monolayer as shown in Figure 3.3b. As for BSA, upon addition of Fbg into the subphase of the pure DMPE monolayer, an additional weak amide I peak at ~1660 cm^{-1} is detectable and is attributed to the α-helical components of the protein structure.[131] However, the interaction of Fbg with the monolayer containing PEG is drastically different to that observed for BSA. In fact, the intensity of the amide I peak from

Fbg increases with higher PEG content, as can be seen from the mixed monolayer with 1 and 5 mol% DMPE-PEG2000. Only when the PEG concentration in the monolayer is further increased to 10 mol% the protein adsorption to the surface can be suppressed, leading to a situation where the SFG spectrum remains unchanged upon Fbg injection into the subphase.

Figure 3.5 shows the integrated amide I SFG intensity, obtained by integrating between 1615 cm^{-1} and 1700 cm^{-1} the difference spectrum in presence and absence of protein. From this graph, it is apparent that the amide I signal from BSA continuously decreases with increasing PEG concentration in the mixed monolayer system. In contrast, Fbg shows an increase in the amide I signal up to ∼5 mol% DMPE-PEG2000 before it vanishes for 10 mol% in the monolayer, indicating that there is a sweet spot around 5 mol% where the amide I SFG signal from Fbg is strongest. This observation for Fbg is somewhat unexpected as PEG is supposed to suppress protein adsorption, and as a consequence, the amide I signal is expected to decrease continuously with increasing PEG concentration. Indeed, from the surface pressure measurements in Figure 3.4 we can conclude that the amount of adsorbed Fbg decreases when increasing the percentage of PEG in the monolayer, similarly to what observed for BSA and in agreement with reports in literature.[35,36,47] In fact, to explain this apparent contradiction, a larger SFG signal for apparently fewer proteins adsorbed at the interface, one has to note that the SFG signal intensity depends not only on the number of probed molecules but also on their orientation. Consequently, the increase in the amide I signal intensity from Fbg at intermediate PEG concentrations (<10 mol%) in the monolayer can only be explained by an increased net orientation of the adsorbed proteins.

Apart from a change in the net orientation of the proteins at the surface, the increased SFG signal intensity could potentially also be explained by a change of the protein conformation. Therefore, the question arises to what extent BSA and Fbg remain in their native states when adsorbed to the PEGylated lipid surfaces. The secondary structure of BSA and Fbg is not changing significantly for different PEG concentrations since the amide I spectra are very similar for all concentrations (Figure 3.3 and Fig. 3.11 in section 3.6). However, at surfaces, structural changes often occur in the tertiary structure where helices, turn and sheet structures change their relative orientations.[132] A more detailed picture of surface conformation can be obtained using a recently developed method where the experimental SFG data are connected to protein structures by theoretical SFG spectra calculated from the
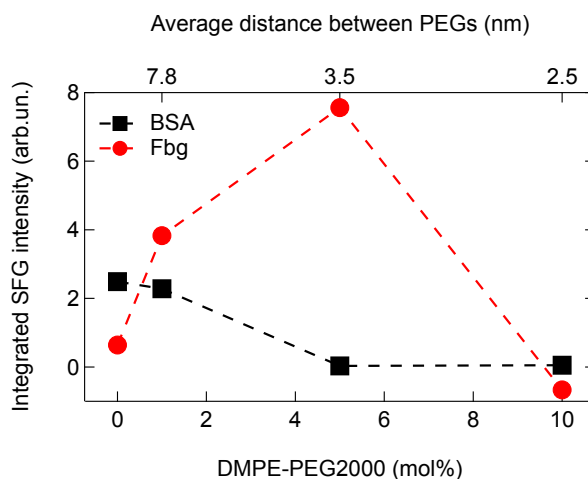
Figure 3.5: Integrated SFG signal in the amide I region of BSA and Fbg for different PEG contents in the mixed phospholipid monolayers.

PDB structure files.[133,134]

Structure files based on PDB entries 4F5S[128] and 3GHG[131] in combination with lipid headgroups were used to calculate the BSA and Fbg spectrum, respectively. Further details about the calculation procedure are summarized in section 3.6. The calculated spectra are shown in Figure 3.6 along with the measured SFG spectra. The calculated spectra capture the center positions and the spectral shape of the experimental protein and lipid peaks very well. It is important to note that besides an overall amplitude scaling factor, no adjustable parameters were used when comparing the experiments with the calculations. The general agreement between the two clearly shows that the structures of BSA and Fbg are likely preserved when binding to the PEGylated lipid layer (see section 3.6, Fig. 3.12 and Fig. 3.13) and is consistent with Fbg laying mostly flat on the surface. While bending like that suggested by Clark et al.[117] upon adsorption of Fbg on aliphatic poly(ether urethane) cannot be ruled out, we do not have any experimental evidence of such a change in conformation and thus decided to stick to the conformation of the crystalline structure as it returns a calculated spectrum in good agreement with our experimental data. Previous studies, using dual polarization interferometry on a similar system, also found that Fbg lies flat on the surface.[103]

Stable binding of native structures also at low PEG concentration differs from an earlier report by Michel et al., who found that BSA and Fbg denature at low PEG concentrations.[101] The difference is likely explained by two factors: (i) the earlier
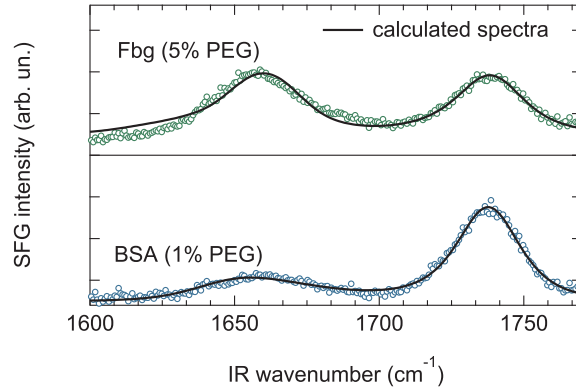
Figure 3.6: SFG spectra (open circles) in the amide I region of BSA (bottom) and Fbg (top) (0.1 mg ml^{-1}) at mixed DMPE:DMPE-PEG2000 monolayers with 1 and 5 mol% DMPE-PEG2000, respectively. The black lines are the corresponding calculated spectra from the PDB files.

study used ultra-high vacuum methods to probe protein folding, while in this work we use a hydrated interface, and (ii) the surface underlying the PEG layer in ref. [101] was charged while the present study uses uncharged, polar chemistry.

These results suggest that PEG not only acts as a protein repelling material but, depending on the protein, can also influence the adsorption geometry. Moreover, Fbg seems to have a stronger tendency to interact with the PEGylated surfaces compared to BSA: when ∼5 mol% PEG is present in the monolayer a change in surface pressure is still detectable for Fbg but not for BSA. This is also in good agreement with the observations by Schöttler et al. where it has been found that similar amounts of Fbg and human serum albumin are present in the protein corona of PEGylated polystyrene nanoparticles, even though albumin is ∼90 times more abundant in human blood than Fbg.[25,135,136]

3.5 Conclusions

In conclusion, we have shown that PEG does not simply act as a protein repelling material, but can interact differently with different proteins and strongly influence their orientation upon adsorption. Moreover, upon interaction with Fbg the properties of the PEGylated surface can be tuned through three different states: first the state of maximum protein adsorption in complete absence of PEG, second a state

of maximum protein orientation at intermediate coverage, and finally a protein repelling state at PEG concentrations above 10 mol%. In contrast, PEG seems to act as a purely repelling material for BSA, indicating the possible influence of the protein structure, globular in case of BSA and more elongated for Fbg, in determining the interactions with the surface functional groups as they might change configuration from mushroom-like, at low PEG concentration, to brush at higher concentrations.[44]* These findings can be exploited in the design of surfaces for biomedical applications. A deeper understanding of protein adsorption on functionalized surfaces clearly requires further characterization of adsorption not only regarding adsorption quantity but also regarding adsorption orientation and conformation of the proteins at the surface.

3.6 Supplementary Information

Lipid monolayer preparation

1 mmol DMPE and DMPE-PEG2000 (both Avanti Polar Lipids, purity >99%) were dissolved in chloroform (VWR Chemicals, purity 99%) and are mixed by volume to get solutions with 0, 1, 5 and 10 mol% DMPE-PEG2000 content. The lipids are then spread on an aqueous phosphate buffered saline subphase (PBS, Sigma Aldrich pH = 7.4) in a translating trough and compressed to an initial surface pressure of 20 mN m^{-1}. The average area per DMPE-PEG2000 molecule in the monolayers containing 1, 5 and 10 mol% DMPE-PEG200 is ∼60, 12 and 6 nm^2, respectively. This has been calculated by tracking the number of molecules present at the surface and the area they occupy. To study the protein adsorption behavior either bovine serum albumin (BSA, Sigma Aldrich, purity ≥96%) or fibrinogen (Fbg, Sigma Aldrich, clottable protein >90%) dissolved in PBS buffer solution was injected into the subphase to reach a final concentration of 0.1 mg ml^{-1}. During the measurements the surface pressure was monitored at all times using a DeltaPi tensiometer (Kibron, Finland).

---

*The Flory radius for PEG2000 is calculated to R$_F$ = 3.8 nm. Therefore, the onset from a mushroom to a more brush-like conformation is likely to be around 5 mol% DMPE-PEG2000.

SFG data treatment

All spectra were taken in *ssp*-polarization combination (*s*-SFG, *s*-VIS and *p*-IR), are background subtracted and normalized with a non-resonant reference signal from a gold film deposited on a silicon wafer used to account for the IR spectral shape. *ssp*-polarization combination was chosen as the interpretation of the spectra is more straightforward than in the *ppp* case and because the signal to noise ratio in *sps* configuration is so low that spectra with detectable signal in the amide I region could only be recorded for Fbg at the mixed monolayer containing 5 mol% DMPE-PEG2000. *ppp* SFG spectra in the amide I region of Fbg at mixed DMPE:DMPE-PEG2000 monolayers with DMPE-PEG2000 content varying from 0 to 5 mol% are plotted in Figure 3.12.
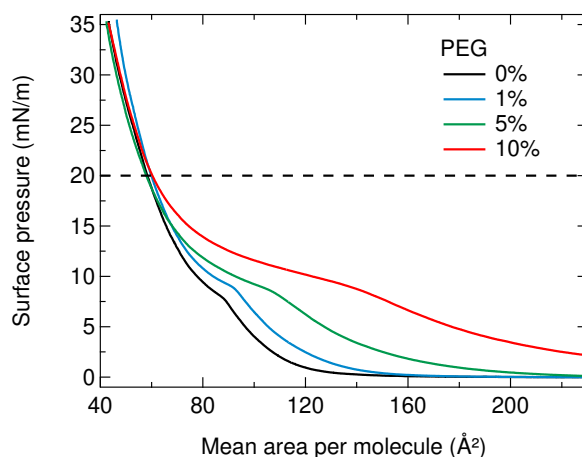
Pressure/area isotherms & BAM

Figure 3.7: Monolayer compression (π-A) isotherms measured at $22\pm1°$C of the mixed DMPE:DMPE-PEG2000 monolayers with DMPE-PEG2000 content varying from 0 to 10 mol%.

Figure 3.7 shows the monolayer compression isotherms of the different mixtures of DMPE:DMPE-PEG2000. The changes in the isotherms with increasing PEG content is comparable to reported results for other mixed monolayer systems with PEGylated phospholipids.[124–126] As can be seen from the figure, at high surface pressures > 20 mN m^{-1} all mixed monolayers behave almost identical as the pure DMPE monolayer, which indicates that the PEG chains are completely submerged into
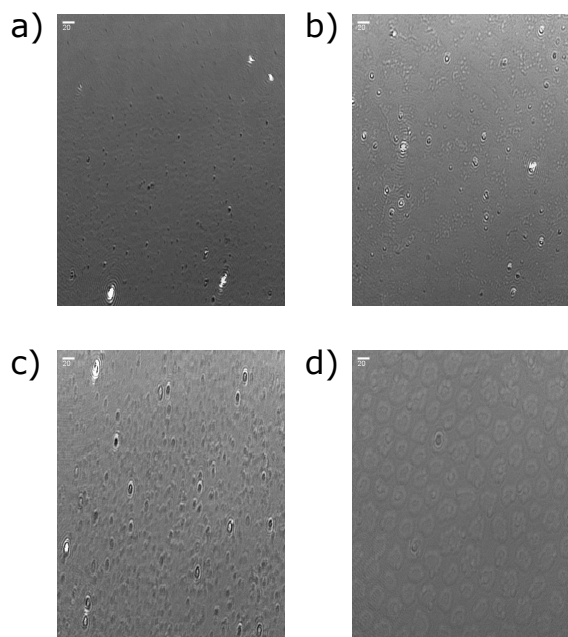
Figure 3.8: BAM images of different mixed DMPE:DMPE-PEG2000 monolayers with increasing PEG concentration: a) 0, b) 1, c) 5, d) 10 mol%. All images are taken at a surface pressure of 20 mN m^{-1}. The scalebar size is 20 μm and the sensitivity of the detecting camera was automatically adjusted: For this reason, the intensities between the different images are not comparable.

the buffered subphase. At a surface pressure of 20 mN m^{-1}, all monolayers are in the liquid-condensed phase. Studies using a mixed monolayer using a very similar phospholipid, 1,2-distearoyl-sn-glycero-3-phosphoethanolamine (DSPE),[124,125] found that by changing the PEG concentration in the monolayers from 1 to 10 mol% the PEG chains are expected to change from mushroom to brush conformation, so we can expect the same is happening in our study.

In Figure 3.8 BAM images of the different mixed phospholipid monolayers with DMPE-PEG2000 concentrations from 0 to 10 mol% are shown. The images are taken at a surface pressure of 20 mN m^{-1}, as in the SFG measurements. The BAM images show that as the DMPE-PEG2000 content in the monolayer increases the monolayer's roughness increases in agreement with what reported in literature on similar systems.[127]
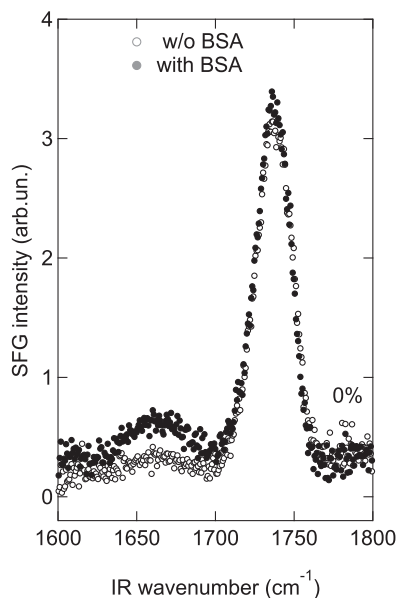
Figure 3.9: SFG spectra in the amide I region before (open symbols) and after (filled symbols) injection of BSA at the DMPE monolayer. Data replotted from Figure 3.3.

SFG measurements

Figure 3.9 shows the SFG spectra in the amide I region before (open symbols) and after (filled symbols) injection of BSA into the subphase of the DMPE monolayer. This is a rescaled Figure derived from the data also shown in Figure 3.3. As can be seen a new peak centered at 1660 cm^{-1} appears after injection of BSA, which indicates the presence of the protein at the surface. In our raw spectra, a broad ($\sim$1580-1800 cm^{-1}) and very weak SFG signal is always present, which is generated by the water bending mode. The spectrum is shown in Figure 3.10. In order to get rid of this background signal, the SFG spectrum of the plain air/PBS interface was subtracted from all spectra (with and without proteins). However, this contribution is still visible in some measured spectra, since our background subtraction method possibly underestimates the contribution of more ordered water at the mixed air/monolayer interface compared to the plain air/PBS interface. Furthermore, all shown spectra are normalized on the IR spectral shape after subtraction of the background signal. The weak peak in the amide I region appearing in some of the measured spectra could also be an artifact from that normalization, which can over-compensate the water absorption, since the residual environmental humidity can
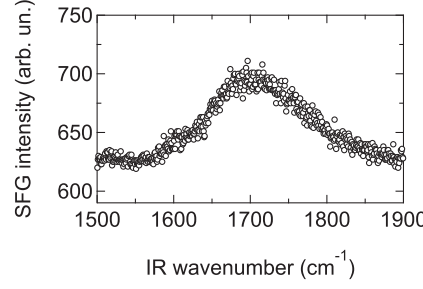
Figure 3.10: SFG spectrum of the air/PBS interface in the amide I range. The measurement was done in *ssp* polarization combination with an integration time of 10 minutes.

Table 3.1: $\chi^{(2)}$ tensor elements contributing to the SFG spectra for different polarization combinations for an azimuthally isotropic surface.

Polarization combination (SFG, VIS, IR)	Probed $\chi^{(2)}$ elements ($x \equiv y \parallel$ surface, $z \perp$ surface)
ssp	$\chi^{(2)}_{xxz}$
ppp	$\chi^{(2)}_{zzz}$, $\chi^{(2)}_{zxx}$, $\chi^{(2)}_{xzx}$, $\chi^{(2)}_{xxz}$

slightly change from measurement to measurement.

The SFG spectra in Figure 3.11 for the monolayers in presence of proteins show that the shape of the protein signal in the amide I region, does not change changing the DMPE-PEG2000 content in the mixed monolayers. Therefore we conclude that the protein secondary structure is not dramatically changed with increasing DMPE-PEG2000 content. Figure 3.12 depicts SFG spectra in *ppp* polarization combination for different mixed DMPE:DMPE-PEG2000 monolayers in presence of Fbg at the surface. As in the case of *ssp* polarization combination, the intensity of the protein amide I signal increases with increasing DMPE-PEG2000 concentration in the monolayer. In *ppp* polarization combination several $\chi^{(2)}$ tensor elements are probed simultaneously (see Table 3.1) and can interfere with each other making the interpretation of measurement in this polarization combination less straightforward.
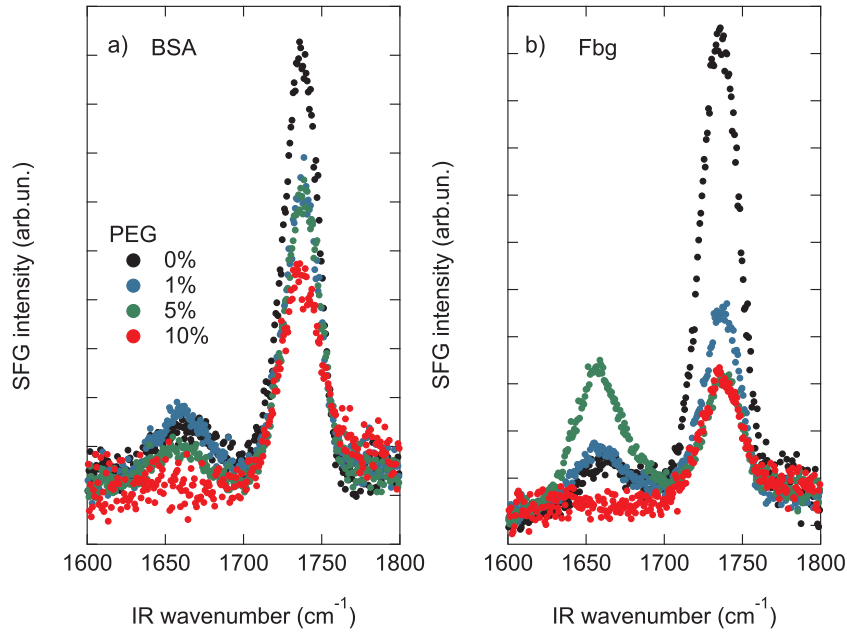
Figure 3.11: SFG spectra in the amide I region of a) BSA and b) Fbg at mixed DMPE:DMPE-PEG2000 monolayers with DMPE-PEG2000 content varying from 0 to 10 mol%. Data plotted from Figure 3.3.

Calculation of vibrational SFG spectra

The spectral vibrational SFG calculations have been performed based on the formalism described in Ref. [133]. Briefly, the atom coordinates were obtained from the PDB files, from which the one-exciton Hamiltonians were constructed. Then, after diagonalization, the eigenvalues and eigenvectors of the systems were obtained, from which their spectroscopic responses were calculated. The couplings in the Hamiltonians were determined (I) for nearest neighbors using a parametrized map of an ab initio calculation of a glycine dipeptide (Ac-Gly-NHCH$_3$) with the 6-31G+(d) basis set and B3LYP-functional, that gives the coupling as a function of the dihedral angle, and (II) for non-nearest neighbors using the transition dipole coupling (TDC) model that gives the through-space coupling in a Coulomb-like fashion. The rationale behind this is that the neighbor coupling is dominated by through-bond effects, while non-nearest neighbors couple mainly through space. The local amide I mode frequencies of the amide groups are redshifted according to the same empirical hydrogen-bond shift model used in Ref. [137], which is a more detailed version of
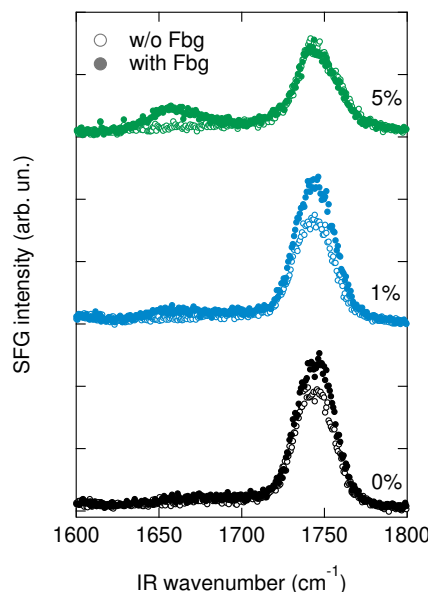
Figure 3.12: SFG spectra in *ppp* polarization combination in the amide I region of Fbg at mixed DMPE:DMPE-PEG2000 monolayers with DMPE-PEG2000 content varying from 0 to 5 mol%.

the model described in Ref. [138] as described in Ref. [133], however with 20% smaller hydrogen bond length - redshift ratios.

The vibrational SFG spectrum is generally very sensitive for the orientation of the protein. In order to reproducibly define the molecular axis of the proteins, we aligned them according to their moments of inertia, using the *orient* script in VMD (see Figures 3.13 b and c).[139] We found that the experimental spectra of Fbg could be reproduced well with $\Theta = 5.9°$, with Φ and Ψ averaged from 0 to 2π due to the azimuthal isotropy (Θ, Φ and Ψ being the Euler angles as usually defined, see Fig. 3.13 a) and also Ref. [133]). The Θ-angle of the lipid C=O-mode was set to 64° in accordance with IRRAS measurements on similar phospholipids.[140] The fitted width of the Lorentzians was 5.1 cm^{-1} for the protein normal modes and 6.3 cm^{-1} for the lipid C=O groups, while the gas phase frequency of the amide I local modes was found to be 1678 cm^{-1}. For BSA the azimuthal isotropy seems less pronounced, so we fitted the data without averaging Φ. The experimental BSA spectra could be reproduced well with a rather broad orientation distribution centered around $(\Theta,\Phi) = (\sim100°, \sim210.0°)$. The broad distribution around these values, probably a result of the more-globular structure of BSA compared to Fbg, is reflected in the
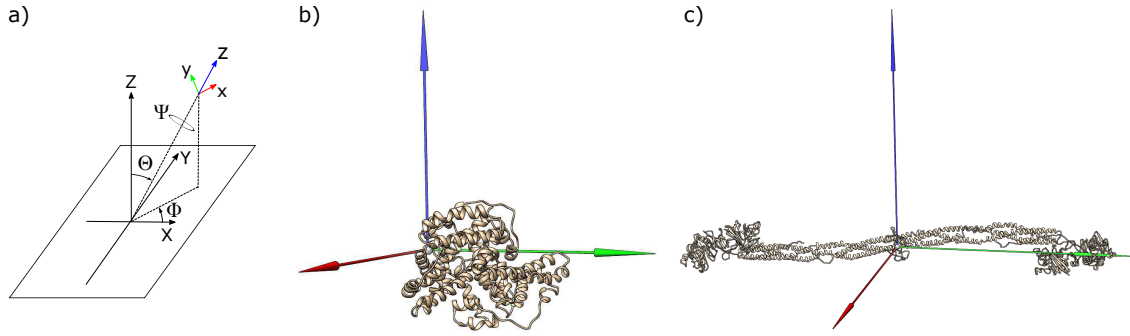
a)

b)

c)

Figure 3.13: a) Definition of the molecular axis and the Euler angles (Θ, Φ, Ψ), orientation of b) BSA (Θ, Φ) = (96.7°, 213.0°) and c) Fbg in the molecular frame (Θ = 5.9°, Φ is averaged from 0 to 2π). Red, green and blue represent the x, y, and z-axes respectively. The z-axis is parallel to the surface normal in the lab frame.

much larger width of the normal modes of the protein (15.7 cm^{-1}, as compared to 5.1 cm^{-1} for Fbg); all other parameters remained the same as for Fbg.

4 Interfacial Conformation of Hydrophilic Polyphosphoesters Affects Blood Protein Adsorption

4.1 Abstract

Synthetic polymers are commonly used as protein repelling materials for a variety of biomedical applications. Despite their widespread use, the fundamental mechanism underlying protein repellence is often elusive. Such insights are essential for improving existing and developing new materials. Here, we investigate how subtle differences in the chemistry of hydrophilic polyphosphoesters influence the adsorption of the human blood proteins serum albumin and fibrinogen. Using thermodynamic measurements, surface-specific vibrational spectroscopy, and Brewster angle microscopy, we investigate protein adsorption, hydration, and steric repulsion properties of the polyphosphoester polymers. Whereas both surface hydration and polymer conformation of the polymers vary substantially as a consequence of the

chemical differences in the polymer structure, the protein repellency ability of these hydrophilic materials appears to be dominated by steric repulsion.

4.2 Introduction

PEGylation of drug nanocarriers is frequently utilized to reduce nonspecific cellular uptake and prolong blood circulation lifetimes.[6,141] However, besides the widespread use of PEG, this material, unfortunately, has several drawbacks especially for biomedical applications, such as the lack of chemical functionalization and the fact that it is not biodegradable and consequently accumulates in the body, to trigger allergic reactions.[141,142] Very recently, a new class of materials - polyphosphoesters (PPEs) - was introduced for so-called "stealth" functionalization of drug nanocarriers.[25,34,143,144] PPEs can overcome the limitations mentioned for PEG, as PPEs can be chemically modified and are biodegradable.[32,143] Moreover, the degradation time and products are tunable by chemical alterations of the PPE structure.[32,143] Nanoparticles functionalized using PPEs have protein-repelling properties equivalent to that of PEG. In fact, for both PEG and PPE modifications, small amounts of proteins can still adsorb, which has been found beneficial to produce "stealth" nanoparticles.[25] Despite the great promise of PPE surface modification as a versatile approach to achieve protein-repelling properties, the microscopic mechanism underlying the protein repellence behavior of PPEs is still unknown. Understanding the protein-repelling mechanism of these polymers is of great importance, especially for the design of new drug nanocarrier systems, for which controlling protein adsorption is crucial. A previous study by Simon et al. has revealed a correlation between the macroscopically determined hydrophilicity of PPE (co)polymer-functionalized nanoparticles with changes of the protein corona composition as well as with cellular uptake.[34] While for PEG many studies have been performed over the years, there is a lack of further insights into the microscopic protein-repelling mechanism of PPEs in the literature. For PEG, two mechanisms of protein repulsion have been proposed. First, hydration forces are considered responsible for the protein-repelling properties of loosely packed short PEG chains.[29–31,38–40] Protein adsorption onto those surfaces is energetically unfavorable, as the hydration water molecules constitute an energetic and physical barrier, which needs to be overcome.[30,37] Second, steric hindrance has been widely used to explain the protein-repelling properties of long-chain and densely packed short-chain PEG layers[26,28,44] as well as oligo(ethylene glycol)-functionalized
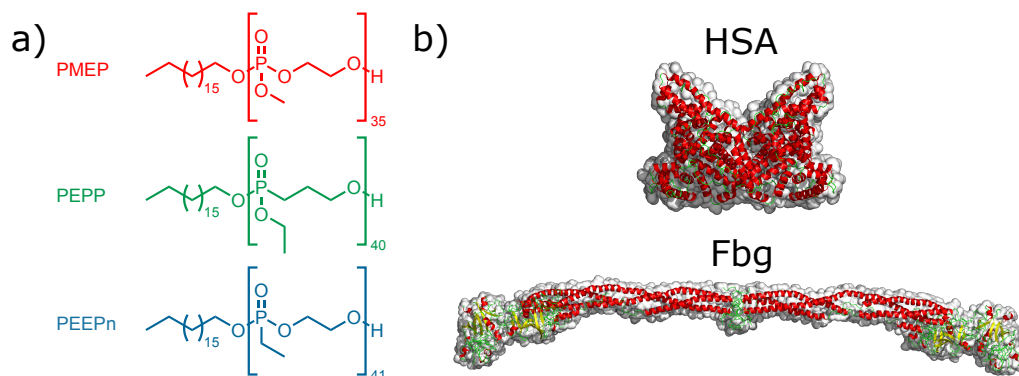
Figure 4.1: a) Chemical structures of the three PPE surfactants PMEP, PEPP, and PEEPn. b) Crystal structures of HSA (PDB code 1AO6) and Fbg (PDB code 3GHG), not to scale.

polymer brushes:[24,145] proteins, while approaching the surface, compress the flexible brush-like PEG chains and reduce the entropy, causing protein adsorption to be energetically unfavorable.[26] While the above two mechanisms explain the protein-repelling ability of PEG, a microscopic understanding of the mechanism explaining the properties of PPEs is still lacking. We tune the surface hydration and polymer conformation by minor changes in the chemical structure of PPE polymers and report how these changes affect the interaction with proteins.

4.3 Experimental

We use model systems consisting of PPE surfactant monolayers on an aqueous subphase with a constant packing density. We prepared three different nonionic PPE surfactants: The hydrophobic tail consists of a C18 chain, while the hydrophilic PPE part was based on either a polyphosphate or a polyphosphonate (main-chain or side-chain polyphosphonate). These minor chemical changes in PPE structure (see Figure 4.1a) result in different hydrolysis degradation times of the polymers in aqueous media and are also expected to influence hydrophilicity. We introduce the blood proteins human fibrinogen (Fbg) and human serum albumin (HSA) to the aqueous subphase to investigate the PPE-protein interaction. HSA is the most abundant blood protein and commonly used to screen for protein-repelling materials. Fbg, on the other hand, is the third most abundant blood protein, which plays an important role in blood coagulation and seems to be effectively repelled by PPE

functionalization.[25]

We use a combination of surface pressure measurements, sum-frequency generation (SFG) spectroscopy, and Brewster angle microscopy (BAM) to study how small chemical changes alter the PPE hydration, steric, and protein-repelling properties. The surface pressure reports on protein adsorption, while SFG spectroscopy is a second-order nonlinear optical technique, which is surface specific due to symmetry selection rules. SFG reports on surface hydration[109,112,115,121,146,147] and protein adsorption[106,107,116,118,148–153] at interfaces. Finally, BAM measurements enable insights into PPE molecular conformation and morphology through the relative layer thickness of the monolayers at the air/water interface.[90–92,154]

Three different nonionic PPE surfactants were prepared by organocatalyzed ring-opening polymerization (ROP) of methyl ethylene phosphate (MEP), 2-ethoxy-1,2-oxaphospholane-2-oxide (EPP), or 2-ethyl-1,3,2-dioxaphospholane 2-oxide (EEPn) with stearyl alcohol as the respective initiator.[33,155] The degrees of polymerization were adjusted to 35-41 repeat units (additional characterization data are shown in the Supporting Information in chapter 4.6). The surfactants only vary in the binding pattern around the phosphorus unit (see Figure 4.1a and chapter 4.6 section NMR spectra), which was proven to strongly influence their hydrolysis degradation in aqueous media.[155] To study the protein adsorption behavior on PPE-functionalized surfaces, we prepared monolayers of the different PPEs on a phosphate buffered saline (PBS) subphase with a mean molecular area of 5 nm^2, representative of that used to prepare drug nanocarriers.[25,34] For protein adsorption studies, the monolayers are spread on a PBS subphase (pH 7.4), but identical results were obtained for a pure H_2O subphase (see Figure 4.12). Measurements to study the hydration of the PPE surfactants are performed on pure water, as the PBS strongly reduces the SFG water signal (see Figure 4.13 in chapter 4.6).

4.4 Results and discussion

After the preparation of the PPE monolayers on PBS, a small volume of a highly concentrated protein solution (either Fbg or HSA, Figure 4.1b) is injected into the subphase to reach a final protein concentration of 0.1 mg/ml. Figure 4.2a reports the evolution of the surface pressure over time for the different PPE monolayers after injection of Fbg or HSA into the subphase at $t \sim 250\ s$. In the case of the PMEP monolayer, the surface pressure increases within minutes after protein in-
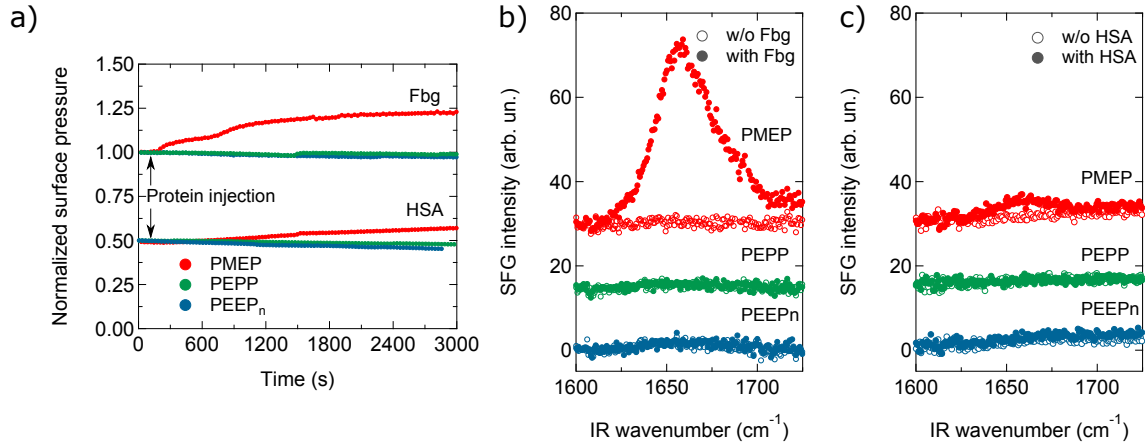
Figure 4.2: a) Normalized surface pressure of the different PPE monolayers on PBS after injection of Fbg and HSA into the subphase at time $t \sim 250$ s. The HSA data are offset vertically for clarity. Amide I region SFG spectra in the absence (open symbols) and presence (filled symbols) of 0.1 mg/ml b) Fbg or c) HSA in the subphase of the PPE monolayers. The curves in panels b) and c) are offset vertically for clarity.

jection and then stabilizes over $\sim$30 min, while no changes in the surface pressure, even after almost 1 h, are detected for the PEPP and PEEPn monolayers. Comparison of the surface pressure response between Fbg and HSA suggests that HSA adsorption on the PMEP monolayer is slower compared to Fbg. Generally, protein adsorption at surfaces is modulated by both the nature of the surface and that of the protein. Hence, the difference in sizes, (tertiary) structures, charge distribution, and hydrophobicity of HSA and Fbg can result in a different adsorption speed of the proteins on PMEP. Interestingly, the observed adsorption speed trend on PMEP is the same observed at the hydrophobic air/PBS interface (see Figure 4.14 in chapter 4.6), indicating that the slower adsorption of HSA relative to Fbg is not an uncommon feature. This observation indicates that both proteins adsorb to the PMEP monolayer, while they are repelled from the PEPP and PEEPn monolayers. This is confirmed by SFG spectroscopy of the amide I region before and after injection of the Fbg (Figure 4.2b) and HSA (Figure 4.2c) solutions. In the absence of proteins in the subphase, no peak is detected in the amide I region for all monolayers. After the injection of the Fbg solution, a broad peak centered at $\sim$1660 cm^{-1} with a shoulder at $\sim$1690 cm^{-1} appears only in the case of the PMEP monolayer. This peak can be attributed to α-helical ($\sim$1660 cm^{-1}) and β-sheet ($\sim$1690 cm^{-1}) components in the protein secondary structure.[131,156] Upon injection of HSA, again, a broad peak
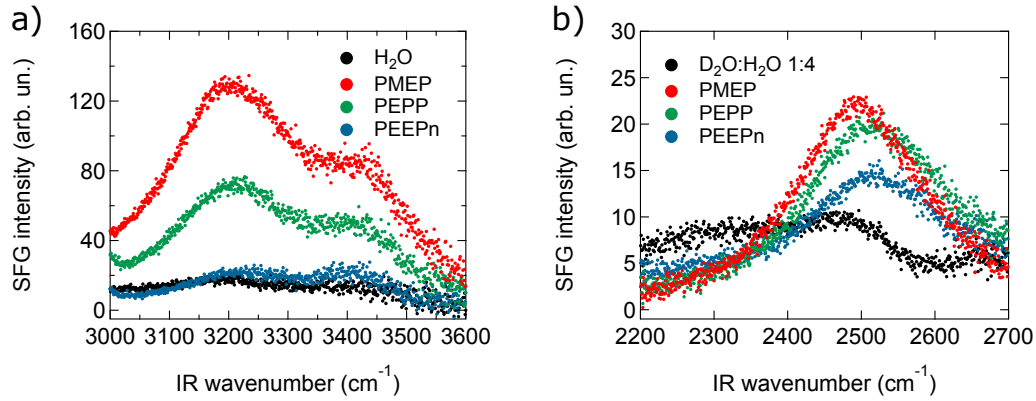
Figure 4.3: SFG spectra of the plain water/air interface (black) and covered with mono-layers of PMEP (red), PEPP (green), and PEEPn (blue): a) in the OH-stretch region on a pure H_2O subphase and b) in the OD-stretch region on an isotopically diluted subphase (D_2O:H_2O 1:4). The mean molecular area for the different PPE monolayers is 5 nm^2.

centered at $\sim$1660 cm^{-1} is present at the PMEP monolayer, which is assigned to the α-helical components in the HSA secondary structure.[157] The presence of amide I peaks indicates not only that Fbg and HSA adsorb but also that they do so in an ordered fashion. However, in both cases, no change in the amide I region is detected for either PEPP or PEEPn monolayers (see Figure 4.15 for other polarization com-binations). An additional confirmation of the absence of protein adsorption on these two monolayers can be found by monitoring the signal from water: while a change in the water signal for PMEP after injection of the protein is observed, no change is apparent in the case of PEPP and PEEPn (see Figures 4.16 and 4.17). A possible explanation of the observed protein adsorption for PMEP could be the presence of unoccupied air/water interface patches; however, based on the SFG spectra, the dangling OH peak at $\sim$3700 cm^{-1} (see Figure 4.18) vanishes for all surfactant mono-layers, which supports the picture that the PPE surfactant monolayers fully cover the surface. At this point, a question naturally follows: Which material property makes PMEP so different from PEPP and PEEPn to explain its ability to adsorb proteins? As mentioned above, for protein-repelling surfaces, two main mechanisms have been considered: hydration and steric hindrance.[26,28,29,31,44] First, motivated by the hydrophilicity of the PPEs, we study the hydration of the different surfactants. To address this question, we measured the vibrational SFG response in the OH-stretch region (Figure 4.3a) for all three PPE surfactant monolayers. SFG spectra in the OH-stretch region contain information about (i) the degree of water align-

ment at the surface, reflected by the intensity of the spectra, and (ii) the average strength of hydrogen bonding of interfacial water molecules, given by the first moment of the spectral distribution (center of mass, COM). Comparing the COMs of the different PPE monolayer SFG spectra enables insight into the relative hydrogen bonding strength without the need of assumptions, as more traditional approaches like, for example, fitting of the spectra usually require. The SFG signal intensity for all PPE monolayers shows an enhancement of the water molecules ordering relative to the neat air/water interface. PMEP seems to possess the strongest net reorientational effect, followed by PEPP, and a weak net reorientation is induced by PEEPn, as testified by the relative peak intensities. Furthermore, the spectra consist of two main bands centered around 3200 and 3400 cm^{-1}, similarly to the water spectra of other protein-repelling surfaces.[109,112–114] In general, the lower the spectral first moment, the stronger is the interaction between water molecules and the surfactants. However, spectral first moments in the OH-stretch region are very close to each other (within 20 cm^{-1}, see Table 4.2 for PMEP, PEPP and PEEPn, which suggests that the average hydrogen bonding strength of water molecules is comparable for the three surfaces. However, the interpretation of SFG spectra can be difficult in the OH-stretch region because they are influenced by inter- and intramolecular coupling of H_2O molecules.[158,159] Thus, to confirm this conclusion, we collected SFG spectra of the monolayers on isotopically diluted water, where inter- and intramolecular coupling effects can be suppressed. Figure 4.3b shows the SFG spectra of the PPE surfactants on D_2O/H_2O 1:4 (v/v) in the OD-stretch region. The measurements were performed on an isotopically diluted D_2O subphase rather than isotopically diluted H_2O to avoid possible interference with the CH-stretch signals from the surfactants that can complicate the interpretation of the spectra. Again, for all three PPE materials, the spectra are significantly different from the plain water/air interface and possess a single band centered around 2500 cm^{-1}. The observed SFG signal intensity trend on the pure H2O subphase is confirmed: PMEP has the highest intensity, followed by PEPP and finally PEEPn. However, the relative intensities between the spectra are different between the data in Figures 4.3a and 4.3b. This indicates that the different chemical structures of the PPE polymers induce differences in the coupling of water molecules. At the same time, the calculated spectral first moments (see Table 4.2) are again quite close to each other for all three surfactants. Thus, from the data in Figure 4.3, we can conclude that the net orientation of water molecules is higher for PMEP than for PEPP and
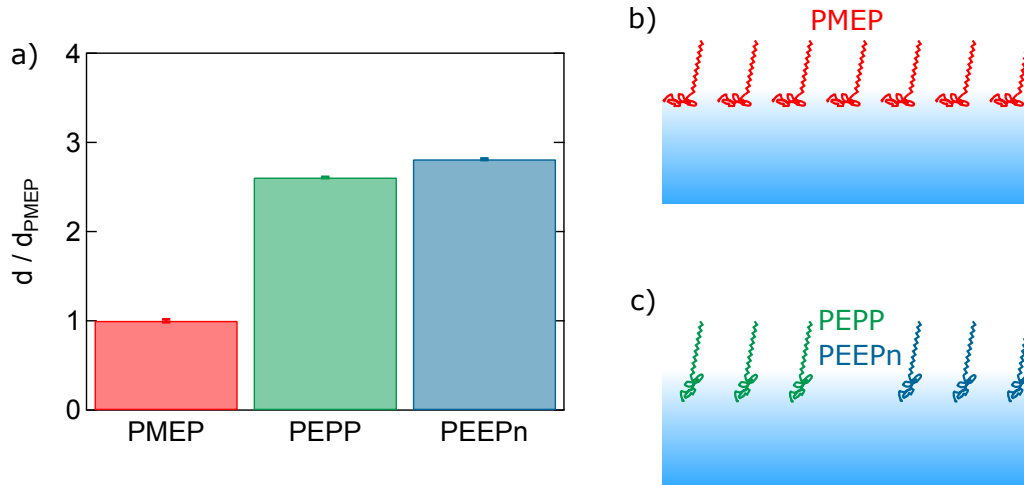
Figure 4.4: a) Relative thickness of the PMEP (red), PEPP (green), and PEEPn (blue) monolayers on PBS normalized on the thickness of PMEP. The error bars represent the standard errors for different measurements on the same sample. On the right, sketches of b) PMEP and c) PEPP and PEEPn monolayer conformation on PBS subphase.

PEEPn, while the average hydrogen bonding strength is comparable for all three PPEs. Nonetheless, the former is not able to repel proteins, while the latter two do. This behavior is opposite to that reported for other materials, where a correlation between strong interaction with interfacial water molecules and protein repellence was found.[108,114,160] Consequently, we conclude that while hydration is different for the three polyphosphoesters, the differences do not explain the protein-repelling behavior of PEPP and PEEPn versus PMEP. To investigate whether, instead, steric hindrance[26,28,44,47] of the materials can explain the difference in the protein-repelling properties of the PEPP and PEEPn surfactants, we performed BAM experiments. It is expected that conformational differences of the polymers will result in changes in the monolayer thickness. BAM measurements provide the relative thickness of the monolayers. In BAM the intensity of the reflected light is proportional to the square of the layer thickness of the thin film. Therefore, it is possible to determine the relative layer thickness of the monolayers from the relative reflected intensity (details can be found in the Supporting Information chapter).

Assuming that the (unknown) monolayer refractive index is the same for all monolayers ($n_{ML} = 1.35$) and purely real-valued because of the absence of transitions at the BAM laser wavelength, we can obtain the relative thickness as shown in Figure 4.4a. For both PEPP and PEEPn the layer thickness is about 3 times that of PMEP.

Using a refractive index value of 1.336 for the PBS subphase, we calculate the layer thicknesses of PMEP, PEPP, and PEEPn to 2.7 ± 0.7, 6.9 ± 0.3 and 7.5 ± 0.3 nm, respectively. The results show that small chemical changes in the polymer headgroups of the PPE surfactants lead to substantial conformational changes possibly due to different chain flexibility of PMEP as compared to PEPP and PEEPn introduced by the P-C bond. In any case, it seems that PMEP prefers a mushroom-like conformation (Figure 4.4b) while the two poly(phosphonates) PEPP and PEEPn reach deeper into the subphase and thus a more extended brush-like conformation (Figure 4.4c and chapter 4.6 last section). These results are in line with reports from the literature, where polymer brushes are known to repel proteins[23,44,47] and explain why PEPP and PEEPn behave differently from PMEP regarding protein-repelling properties. Thus, we conclude that the main mechanism determining the protein-repelling behavior of the PPEs studied in this work is steric repulsion and not surface hydration.

4.5 Conclusions

In summary, we demonstrated how small changes in the chemistry of hydrophilic PPE polymers alter their interfacial protein repelling properties. While both the surface hydration and the polymer conformation are affected by these chemical changes, the usually claimed correlation between hydrophilicity and protein repellence is not observed on a microscopic level. As mentioned above, the hydration water molecules create an adsorption barrier for the proteins, which scales with hydrogen bonding strength and amount of the hydration molecules. Therefore, it is generally assumed that stronger hydration leads to better protein repelling behavior. However, our results show that there is not a sizable difference in the hydrogen bonding strength of the three polymers and that, surprisingly, the polymer onto which proteins adsorb is the one inducing the greatest extent of interfacial water orientation. Instead, modification of the polymers from a poly(phosphate) to a poly(phosphonate) induces a conformation that clearly influences the protein repelling behavior. These results provide important insights into the microscopic mechanisms behind polymer/protein interactions and are important to further improve the design of not just polyphosphoesters but of polymers for biomedical applications in general.

4.6 Supplementary Information

Nuclear magnetic resonance (NMR) spectroscopy

^{1}H, ^{13}C and ^{31}P NMR spectra were recorded using a Bruker Avance 300 or a Bruker Avance III 500. All spectra were measured in CDCl$_3$ or d2-DCM and referenced internally to residual proton signals of the deuterated solvent. The spectra were analyzed using MestReNova 12 software from Mestrelab Research S.L.

Size exclusion chromatography (SEC)

SEC measurements of the surfactants were performed in DMF (containing 1 g/l of lithium bromide as an additive) at 60°C and a flow rate of 1 ml/min with a PSS SECurity as an integrated instrument, including a set of 3 PSS GRAM columns (porosity of 100 Å and 1000 Å) and a refractive index (RI) detector. Calibration was carried out using polyethylene glycol standards provided by Polymer Standards Service.

Synthetic procedures

The monomers, 2-ethyl-1,3,2-dioxaphospholane-2-oxide (EEPn), 2-ethoxy-1,2-oxaphospholane 2-oxide (EPP) and 2-methoxy-1,3,2-dioxaphospholane 2-oxide (MEP), were prepared according to literature procedures.[33,155,161]

Synthesis of PMEP surfactant. All Schlenk-tubes were flame-dried prior to use. 1-Octadecanol was used as initiator and 1,8-diazabicyclo[5.4.0]undec-7-ene DBU (DBU) / 1-(3,5-bis(trifluoromethyl)phenyl)-3-cyclohexylthiourea (TU) as catalyst/ co-catalyst system. TU (121 mg, 739 μmol, 5 eq) and 1-octadecanol (40 mg, 148 μmol, 1 eq) were introduced into a flame-dried Schlenk-tube, dissolved in benzene, and dried by lyophilization. MEP (863 mg, 6.25 mmol, 42 eq) was added. 3 ml of DCM were added and the reaction mixture was cooled down to 0°C and the polymerization was started by rapid addition of DBU (112 mg, 739 μmol, 5 eq). The polymerization was quenched after 1.5 h by addition of an excess of acetic acid in DCM (c = 20 mg/ml). The solvent was removed under reduced pressure and the polymer was dissolved in a mixture of THF/H$_2$O and dialyzed against water. The polymer was obtained as a colorless viscous liquid (660 mg, 77%).

[1]**H NMR** (300 MHz, Chloroform-d) δ 4.29 - 4.21 (m, -O-C**H**$_2$-C**H**$_2$-O- polymer backbone), 3.81 (dd, J = 11.2 Hz, -O-C**H**$_3$), 1.67 (m, -O-CH2-C**H**$_2$ - initiator)

1.24 (s, -(C**H**$_3$)$_{15}$-C**H**$_3$ initiator) 0.87 (t, J = 6.8 Hz, -C**H**$_3$ initiator). ^{31}**P NMR** (202 MHz, Chloroform-d) δ 1.12, -0.18, -1.50. ^{13}**C NMR** (126 MHz, Chloroform-d) δ 66.34 (-O-C**H**$_2$-C**H**$_2$-O- polymer backbone), 54.68 (-OC**H**$_3$ side chain), 29.69, 29.68 (-C**H**$_2$- initiator), 29.65, 29.52, 29.35, 29.16, 14.06 (-C**H**$_3$ initiator).

Synthesis of PEPP surfactant. All Schlenk-tubes were flame-dried prior to use. 1-Octadecanol was used as initiator and 1,8-diazabicyclo[5.4.0]undec-7-ene DBU (DBU) / 1-(3,5-bis(trifluoromethyl)phenyl)-3-cyclohexylthiourea (TU) as catalyst/ co-catalyst system. 1-Octadecanol and TU (136 mg, 370 μmol, 4.6 eq) were dried by lyophilization with benzene. EPP (490 mg, 3.26 mmol, 40 eq) was added to the dried TU. A stock solution of 1-octadecanol in dry toluene was prepared with at a concentration of 20 mg/ml. 1.1 ml (22.0 mg, 84 mol, 1 eq) of the initiator stock solution was added to the monomer. The polymerization was initiated by the addition of DBU (62 mg, 0.41 mmol, 4.6 eq) at 5°C. Subsequently, the reaction mixture was cooled down to 0°C and quenched after 20 h by the rapid addition of an excess of acetic acid (c = 20 mg/ml). The polymer was obtained by three-times precipitation in cold diethyl ether and subsequent dialysis against water to yield 396 mg (81%) of a colorless amorphous polymer.

^{1}**H NMR** (500 MHz, Chloroform-d) δ 4.18 - 4.02 (m, -CH$_2$-C**H**$_2$-O- polymer backbone, -O-C**H**$_2$- side chain), 1.95 (ddt, J = 14.9, 11.0, 6.2 Hz, -O-CH$_2$-C**H**$_2$- polymer backbone), 1.82 (ddt, J = 16.7, 11.7, 7.2 Hz, -O-CH$_2$-CH$_2$-C**H**$_2$- polymer backbone), 1.32 (t, J = 7.0 Hz, -C**H**$_3$ side chain), 1.24 (s, (C**H**$_2$)$_{15}$-CH$_3$ initiator), 0.86 (t, J = 6.9 Hz, -C**H**$_3$ initiator). ^{13}**C NMR** (126 MHz, Chloroform-d) δ 64.99 (-CH$_2$-C**H**$_2$-O- polymer backbone) 61.71(-O-C**H**$_2$- side chain), 29.68 ((C**H**$_2$)$_{15}$- initiator), 23.91 (-O-CH$_2$-C**H**$_2$- polymer backbone), 22.50, 21.36 (-O-CH$_2$-CH$_2$-C**H**$_2$- polymer backbone), 16,51(-C**H**$_3$ side chain), 14.12 (-C**H**$_3$ initiator). ^{31}**P NMR** (202 MHz, Chloroform-d) δ 31.77, 31.43, 31.05.

Synthesis of PEEPn surfactant. 2-ethyl-1,3,2-dioxaphospholane-2-oxide (457 mg, 3.36 mmol, 40 eq) was placed in a flame-dried Schlenk tube. A stock solution of octadecanol in dry toluene was prepared with a concentration of 20 mg/ml. 1.13 ml (22.7 mg, 0.084 mmol, 1 eq) of the initiator stock solution was added to the monomer. The polymerization was initiated by the addition of 62 μL of DBU (64 mg, 0.42 mmol, 5 eq). The polymerization was conducted at room temperature and quenched after 19 h by the rapid addition of an excess of acetic acid (c = 20 mg/ml

in DCM). The polymer was obtained by three-times precipitation in cold diethyl ether and subsequent dialysis against water to yield 448 mg (93%) of a colorless amorphous polymer.

^{1}H NMR (500 MHz, Chloroform-d) δ 4.38 - 4.09 (m, -O-**CH$_2$**-**CH$_2$**-O- polymer backbone), 1.83 (dq, J = 18.4, 7.7 Hz, P-C**H$_2$**-CH$_3$ side chain), 1.26 (s, (C**H$_2$**)$_{15}$- initiator), 1.19 (dt, J = 20.5, 7.6 Hz, P-CH$_2$-C**H$_3$** side chain), 0.86 (t, J = 6.9 Hz, -C**H$_3$** initiator). **^{13}C NMR** (126 MHz, Chloroform-d) δ 64.50(-O-**CH$_2$**-**CH$_2$**-O- polymer backbone), 29.69 ((**CH$_2$**)$_{15}$- initiator), 19.36, 18.22 (P-**CH$_2$**-CH$_3$ side chain), 14.12 (-**CH$_3$** initiator), 6.44 (P-CH$_2$-**CH$_3$** side chain). **^{31}P NMR** (202 MHz, Chloroform-d) δ 35.81, 35.23, 35.36.

Monolayer preparation & surface pressure measurements

PMEP, PEPP and PEEPn are dissolved in a 9:1 (v/v) mixture of chloroform (VWR Chemicals, purity >99%) and methanol (VWR chemicals, chromanorm) to obtain 50 μM solutions. The surfactants are spread on an H$_2$O subphase filtered with a Millipore unit (resistivity $\sim$18 MΩ cm). The mean molecular area per surfactant at the surface for all measurements is 5 nm^2 and was calculated by the number of molecules spread at the surface and the area of the air/water interface. Due to the very low surfactant concentration used in the experiments ($\sim$80 nmol/l as compared to the critical micelle concentrations that are instead in the range of 4-8 μmol/l[162]) multilayer formation of the polymers is not expected. For comparison, the reported functionalized polystyrene nanoparticles have particle radius $r \sim 50$ nm and usually have $N \sim 5 \cdot 10^3 - 1 \cdot 10^4$ functionalized groups at the surface.[25,34,162] Assuming perfectly spherical particles, this results in a particle surface area A_{NP} of: $A_{NP} = 4\pi r^2 = 3.14 \cdot 10^4$ nm^2. Thus, the mean molecular area of functional groups is 3.14 - 6.28 nm^2. For the protein adsorption studies the monolayers were instead prepared on an aqueous phosphate buffered saline subphase (PBS, Sigma Aldrich pH 7.4). Furthermore, small amounts ($\sim$100 μl) of highly concentrated protein solutions of either fibrinogen (Fbg, Sigma Aldrich, clottable protein >90%), human serum albumin (HSA, Sigma Aldrich, >99% purity) dissolved in PBS buffer solution are injected into the subphase to reach a final protein concentration of 0.1 mg/ml. Fbg, HSA and phosphate buffered saline tablets are used as received. Moreover, the surface pressure is simultaneously monitored during all measurements using a DeltaPi tensiometer (Kibron, Finland). The measured surface pressure of the monolayers is

determined to be ∼11 mN/m for PMEP, ∼22 mN/m for PEPP and ∼19 mN/m for PEEPn, respectively. For all three PPEs this value is far below the film pressure at critical micelle concentration, which was determined to be ∼29 mN/m, ∼36 mN/m and ∼28 mN/m for PMEP, PEPP and PEEPn, respectively.[162] These data further confirm, that multilayer formation of the PPE materials can be neglected.

SFG data treatment

The polarization combination in all shown spectra of the manuscript is set to *ssp* (*s*-polarized SFG signal, *s*-polarized VIS-beam and *p*-polarized IR-beam) and the accumulation time is 10 minutes. All spectra are background subtracted and normalized with a non-resonant reference signal from a z-cut quartz to account for the IR spectral shape. All measurements are taken at a room temperature of (22±1)°C. To quantify the average strength of the hydrogen bonding at the different PPE surfaces, the first moment of spectral distribution (center of mass, COM) is calculated:

$$COM = \sum_n \frac{I_{SFG}(\omega_n) \cdot \omega_n}{I_{SFG}(\omega_n)} \tag{4.1}$$

where I_{SFG} denotes the SFG intensity at the IR frequency ω_n.

NMR spectra

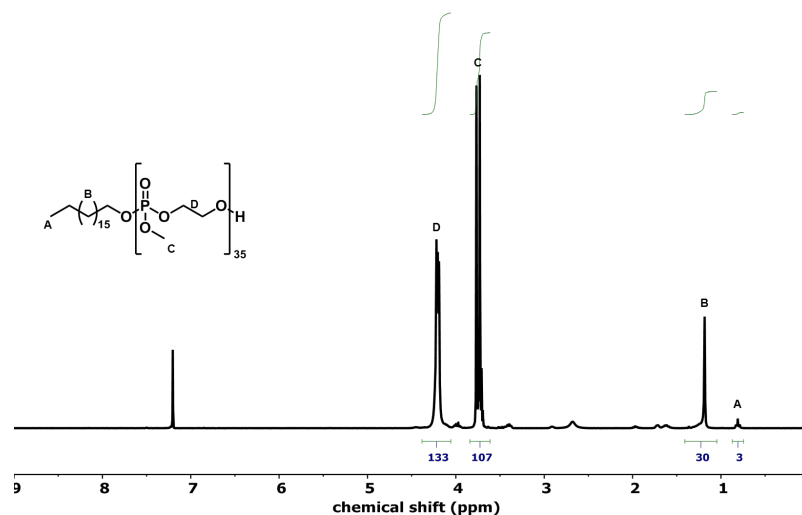**Figure 4.5:** ^{1}H NMR of PMEP (300 MHz, CDCL$_3$, 300K). The repeating units of the polymer were calculated by comparing the integrals of the -CH$_3$ group of the initiator with the -CH$_3$ group (C) in the pendant chain of the polymer.

Figure 4.6: ^{1}H NMR of PEPP (500 MHz, CDCL$_3$, 298K). The repeating units of the polymer were calculated by comparing the integrals of the -CH$_3$ group of the initiator with the -CH$_2$- group (E) in the pendant chain of the polymer.
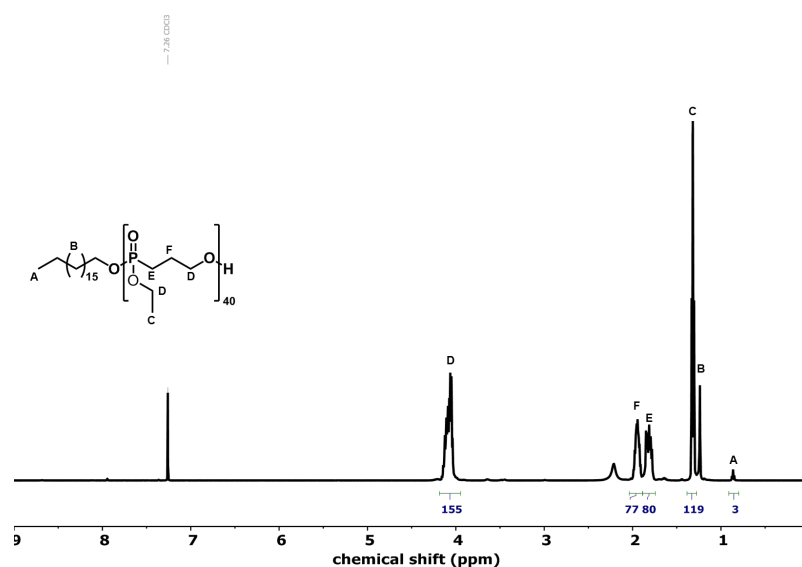
Figure 4.7: ^{1}H NMR of PEEPn (500 MHz, CDCL$_3$, 298K). The repeating units of the polymer were calculated by comparing the integrals of the -CH$_3$ group of the initiator with the -CH$_2$- group (E) in the pendant chain of the polymer.

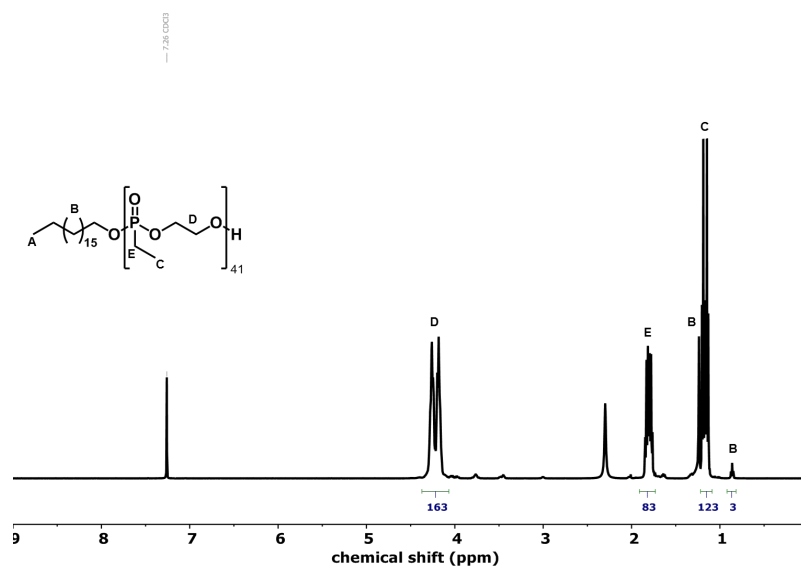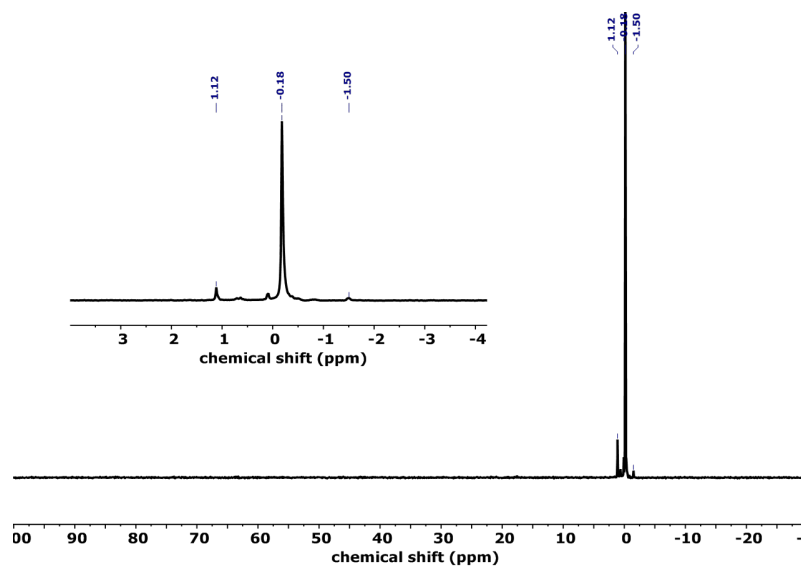**Figure 4.8:** ^{31}P NMR of PMEP (121 MHz, CDCL$_3$, 300K).
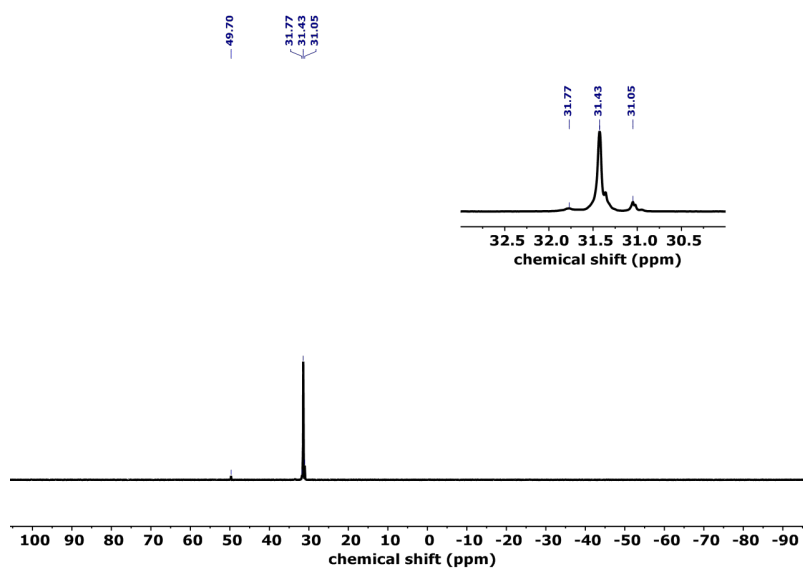
Figure 4.9: ^{31}P NMR of PMEP (202 MHz, CDCL$_3$, 298K).
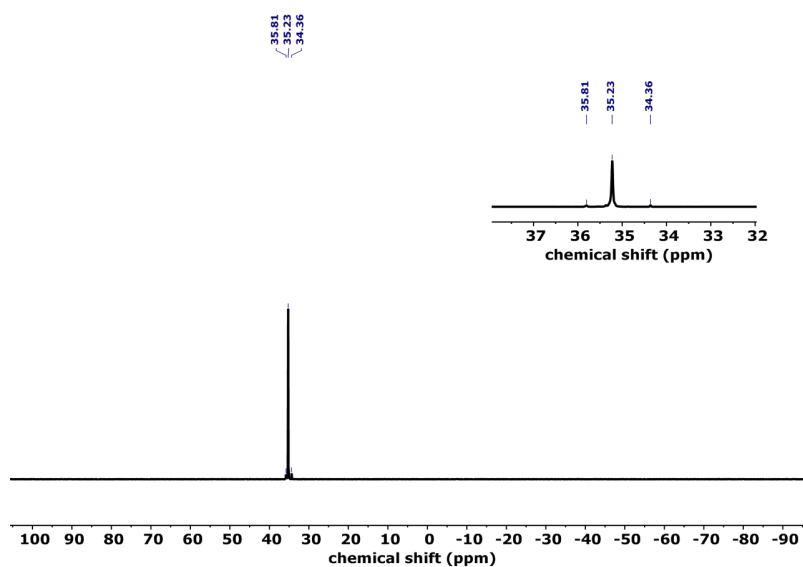
Figure 4.10: ^{31}P NMR of PEEPn (202 MHz, CDCL$_3$, 298K).

SEC analysis
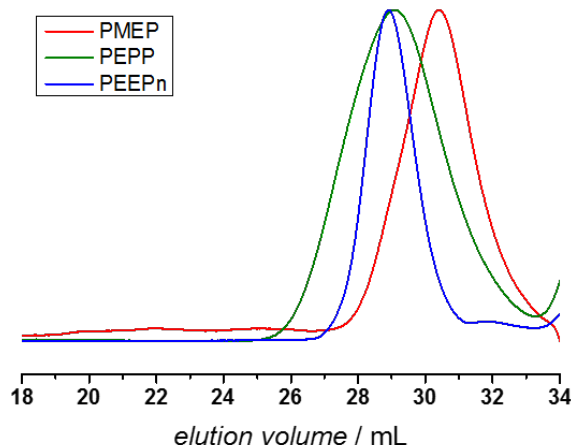
Figure 4.11: SEC elugrams of PMEP, PEPP, PEEPn in DMF at 60 °C.

Table 4.1: SEC data of the prepared surfactants.

Material	M_w (g mol^{-1})	M_n (g mol^{-1})	M_w / M_n
PMEP	2,250	1,697	1.33
PEPP	4,014	2,671	1.50
PEEPn	3,934	3,566	1.10

SFG spectra and surface pressure measurements

The presence of salts in the subphase, by changing from pure H_2O to PBS, does not change the overall protein repelling behavior of the PPE surfactants, as shown in Figure 4.12. In both cases the adsorption of HSA is suppressed for PEPP and PEEPn, while it is not for PMEP.

Figure 4.13 shows the SFG OH-stretch response for a PMEP monolayer on a H_2O, a diluted PBS ($\sim$10 mM ionic strength) and a PBS subphase. The interfacial water structure is changed due to the high ionic strength of PBS, resulting in a strong change in the SFG signal. This effect less pronounced, yet still present for the diluted PBS subphase, indicates a gradual change with increasing ionic strength in the subphase.

The normalized surface pressure measurement data in Figure 4.14 show that HSA adsorbs slower on the air/PBS interface as compared to Fbg. This indicates that the speed trend observed for PMEP in Figure 4.2 in the manuscript is not induced by the polymer, but is a rather common feature.

Figure 4.15 shows the SFG spectra in the amide I region for PEPP and PEEPn monolayers in the absence and presence of Fbg in the subphase. As can be seen from the data, no spectral changes occur upon addition of protein, indicating complete repellence of Fbg by those two monolayers.

Figure 4.16 reports the SFG spectra in the OH-stretch region for monolayers of PEEPn (blue), PEPP (green) and PMEP (red) on PBS. Upon injection of Fbg into the subphase (black lines), only the SFG signal for the PMEP monolayer changes, while PEPP and PEEPn show no change. This suggests, in agreement with surface pressure measurements (see Figure 4.2a), that Fbg is not adsorbing.

The SFG spectra in Figure 4.17 a) for PMEP show changes of the hydration after injection of Fbg in the subphase in *ssp* and *sps* polarization combinations. These changes are not observed in Figure 4.17 b) and c) for PEPP and PEEPn, respectively. This is further confirmation of the absence of proteins at the air/monolayer interface for both PEPP and PEEPn.
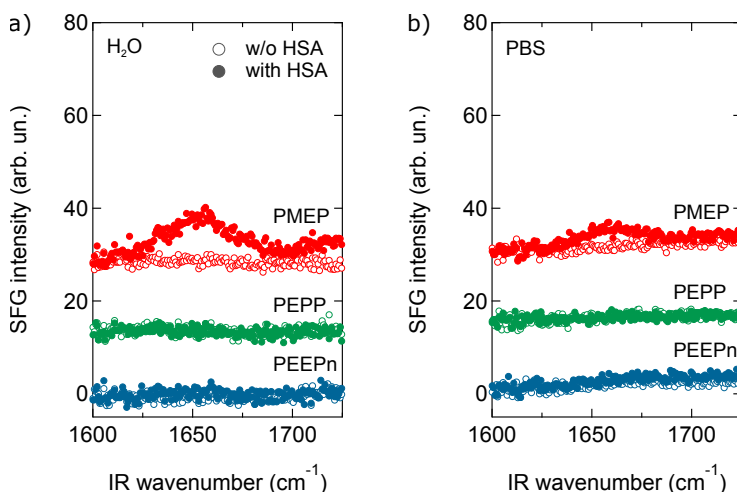
Figure 4.12: SFG spectra in the amide I region for the different PPE surfactant monolayers in absence (open symbols) and presence (filled symbols) of 0.1 mg/ml HSA in the subphase. The subphase is changed from a) pure H_2O to b) PBS as in Figure 4.2. Curves are offset on the y-axis for clarity.
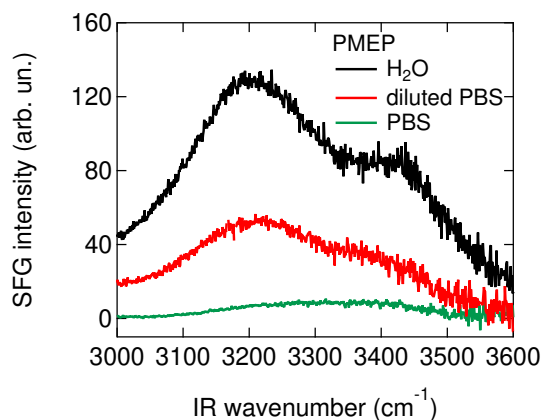
Figure 4.13: SFG spectra in the OH-stretch region for a PMEP monolayer with a mean molecular area of 5 nm^2 on pure H_2O (black), diluted PBS with an overall ionic strength of ~10 mM (red) and PBS (green).
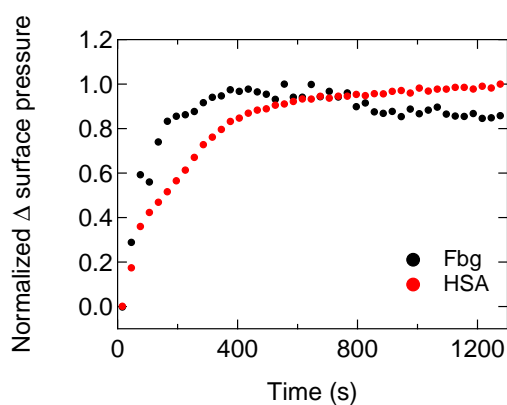
Figure 4.14: Normalized surface pressure of the air/PBS interface after injection of Fbg (black) and HSA (red) into the subphase at time $t \approx 0$ s.
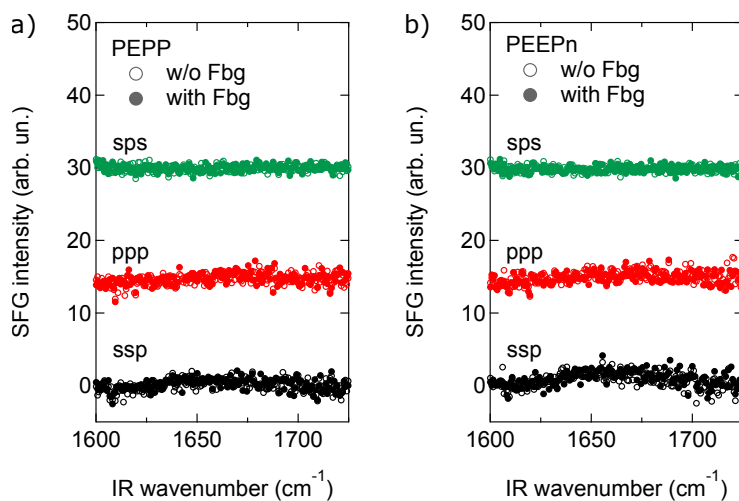
Figure 4.15: SFG spectra in the amide I region for monolayers of a) PEPP and b) PEEPn in absence (open symbols) and presence (filled symbols) of 0.1 mg/ml Fbg in the subphase in *ssp* (black), *ppp* (red) and *sps* (green) polarization combination. The spectra are offset vertically for clarity.
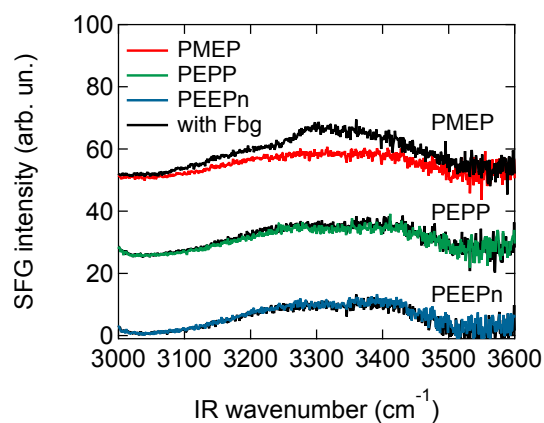
Figure 4.16: SFG spectra in the OH-stretch region for monolayers of PEEPn (blue), PEPP (green) and PMEP (red) on PBS. The black lines represent the spectra after injection of 0.1 mg/ml Fbg into the subphase. The spectra are offset on the y-axis for clarity.
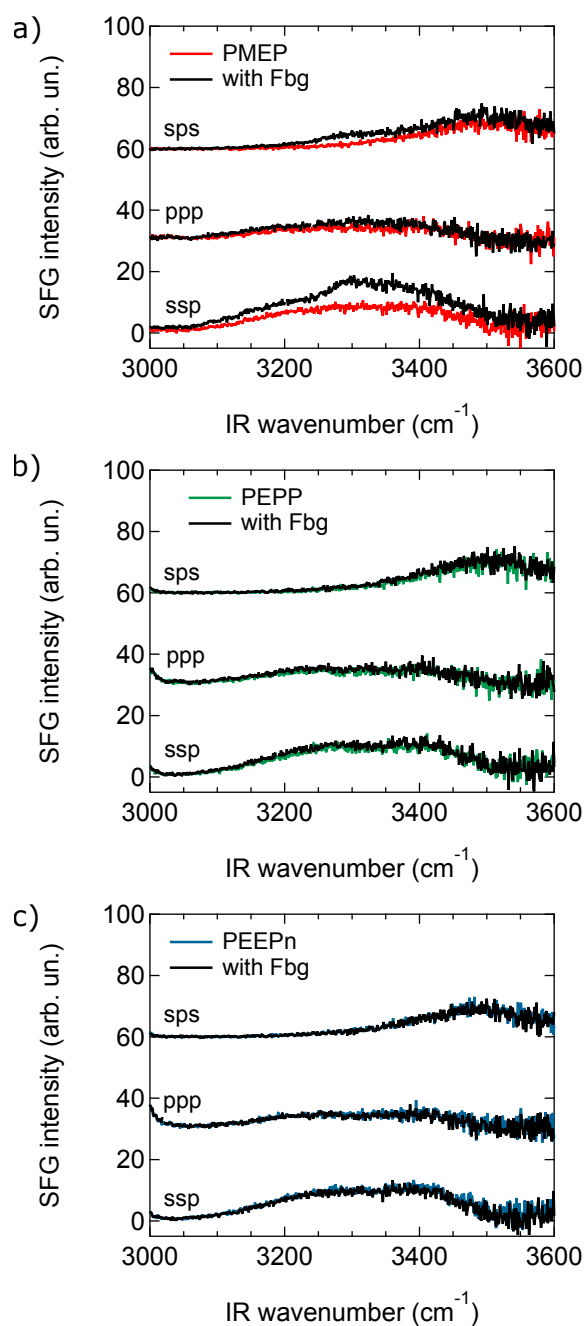
Figure 4.17: SFG spectra in the OH region for a) PMEP, b) PEPP and c) PEEPn in absence and presence (black) of 0.1 mg/ml Fbg in the subphase for *ssp*, *ppp* and *sps* polarization combinations. The spectra are offset vertically for clarity.
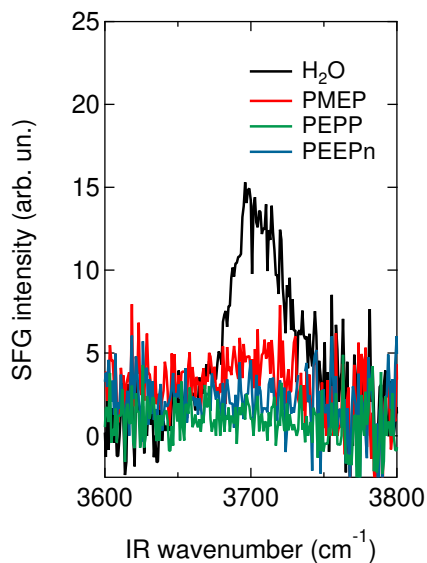
Figure 4.18: SFG spectra in the dangling OH-region for plain H_2O (black), PMEP (red), PEPP (green) and PEEPn.

The dangling OH peak at $\sim$3700 cm^{-1} is a typical signature of the plain water/air interface, resulting from water molecules at the surface with one OH bond pointing towards the gas phase. As shown in Figure 4.18, the dangling OH peak disappears in the presence of the PMEP, PEPP and PEEPn monolayers.

SFG spectra: center of mass

Table 4.2 summarizes the first moments of the spectral distribution for the SFG spectra shown in Figure 4.3, calculated via equation 4.1. For the spectra in the OH-stretch region the COM is calculated in a frequency range of 3000-3600 cm^{-1}, for the isotopically diluted spectra between 2200 and 2700 cm^{-1}.

Table 4.2: Calculated spectral first moments for the SFG spectra shown in Figure 4.3.

Material	COM on pure H_2O subphase (cm^{-1})	COM on D_2O:H_2O 1:4 subphase (cm^{-1})
PMEP	3284	2495
PEPP	3287	2516
PEEPn	3304	2504

Table 4.3: Comparison of the experimentally determined monolayer thickness from BAM on the PBS and plain water subphase with the theoretically expected values for the mushroom size (Flory radius R_F) and the brush thickness L. The average distance between the monolayer molecules is d = 2.2 nm for all materials.

Material	Calculated layer thickness on PBS (nm)	Calculated layer thickness H_2O (nm)	Theoretical Flory radius R_F (nm)	Theoretical brush thickness L (nm)
PMEP	2.7 ± 0.7	2.8 ± 0.5	5.1	8.7
PEPP	6.9 ± 0.3	7.8 ± 0.5	5.5	10.0
PEEPn	7.5 ± 0.3	9.3 ± 0.2	5.6	10.2

Determining the relative monolayer thickness

For these experiments the BAM setup was calibrated as described in section 2.3. The measured intensity values divided by the input intensity are $(1.7 \pm 0.8) \cdot 10^{-8}$, $(1.14 \pm 0.08) \cdot 10^{-7}$ and $(1.32 \pm 0.18) \cdot 10^{-7}$ for PMEP, PEPP and PEEPn respectively. The intensity is detected from a broad region of interest (the same where the calibration was performed) and the errors are obtained by averaging over $\sim$190 individual measurements. Based on these reflected intensities, the relative monolayer thickness was obtained as shown in Figure 4.4 a. Here, we assume that the three monolayers with PMEP, PEPP and PEEPn possess the same (real valued) refractive index. Using the relation between the measured reflectivity R and the thickness of the monolayers (equation 1 in Ref. [92]), we can calculate the thickness of our monolayers. Here, we assume an effective refractive index for the monolayers of 1.35, due to the fact that the interfacial layer mainly consists water and only few surfactant molecules. Furthermore we use $\lambda \sim 658$ nm for our laser wavelength and 1.336 as the refractive index of the PBS solution at this wavelength. The resulting layer thicknesses are summarized in Table 4.3. It is worth noting, that using a higher refractive index for PMEP (denser layer because of its mushroom-like conformation as compared to the more brush-like conformation of PEPP and PEEPn) as compared to PEPP and PEEPn would lead to an even lower layer thickness for this polyphosphoester layer. We compared the relative layer thicknesses of the monolayer on a PBS subphase with a pure H_2O subphase in order to see, whether the presence of ions in the subphase influences the polymer conformation and therefore the layer thickness (see Figure 4.19). The calculated layer thickness on the pure
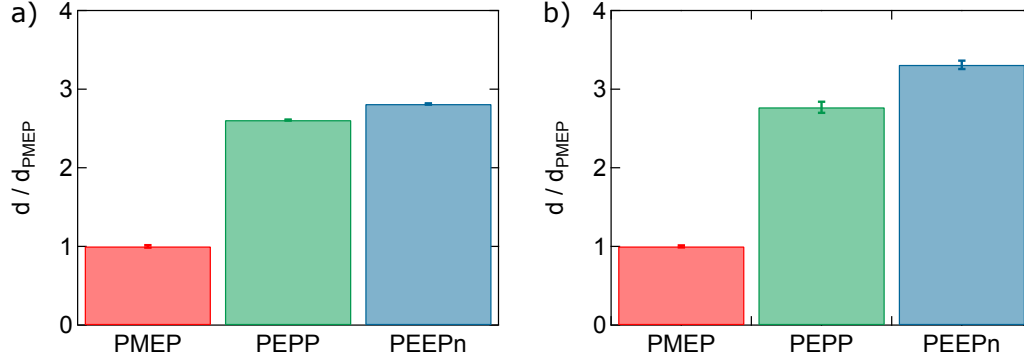
Figure 4.19: Relative thickness of the PMEP (red), PEPP (green) and PEEPn (blue) monolayers normalized on the thickness of PMEP on a a) PBS and b) pure H_2O subphase, respectively. The error bars represent the standard errors for different measurements on the same sample.

water subphase, using $n_{water} = 1.33$ and $n_{ML} = 1.344$, to keep the refractive index change constant, are also summarized in Table 4.3. The results show, that even though there are small differences for the different subphases, the overall effect of the ions is negligible in this work.

Comparing the monolayer thickness with expected mushroom and brush sizes

A common measure to determine the polymer monolayer transition from mushroom to brush conformation is a comparison of the Flory radius R_F with the average distance between the monolayer molecules d. The polymers are supposed to assume a mushroom conformation for low packing densities of the monolayers ($d > R_F$), whilst they are forming a uniform brush, with the brush thickness L, for high packing densities ($d < R_F$).[42] The distance between the monolayer molecules in this work is $d \sim 2.2$ nm and the Flory radii for the materials is in the range of 5.1 nm, 5.5 nm and 5.6 nm for PMEP, PEPP and PEEPn, respectively. Therefore, all polymers are theoretically expected to be in brush conformation. We calculated the Flory radius R_F and the theoretical brush thickness L for the PPE polymers in a good solvent with a monomer length of $a = 0.6$ nm for all PPEs:[42]

$$R_F = aN^{3/5} \tag{4.2}$$

$$L = Na\left(\frac{a}{d}\right)^{2/3} \tag{4.3}$$

The resulting theoretical values R_F, d and the experimentally determined layer thicknesses are summarized in Table 4.3. A comparison for PMEP shows that the calculated layer thickness is lower than the theoretically expected brush thickness, while the for PEPP and PEEPn the values are comparable to the theoretically expected ones. These findings suggest that PEPP and PEEPn present a more brush-like conformation with respect to PMEP.

5 Both poly(ethylene glycol) and poly(methyl ethylene phosphate) can guide specific protein adsorption

Contributions to this chapter: C. Bernhard, G. Gonella and M. Bonn designed the research project. C.B. performed the SFG, BAM and surface pressure experiments. Further SFG spectroscopy data were collected by D. Maltseva. S. J. Roeters and T. Weidner did the calculations of the protein SFG spectra. K. N. Bauer and F. R. Wurm designed and performed the PMEP synthesis and characterization. The cHSA synthesis and characterization were done by M. Mueller and S. L. Kuan. All authors discussed the results and contributed to the manuscript.

5.1 Introduction

Over the last decades biosensors have gained a lot of attention, because of their potential applications in medicine, environmental monitoring and bioanalytics.[163,164] They are of special interest in the biomedical area where nanoparticle-based sensors can be used as diagnostic agents, for instance, and to monitor the health status of patients.[164–166] However, despite their promising potential applications, nano-biosensors often suffer from nonspecific protein adsorption at the surface of the nanoparticles. These nonspecifically bound proteins form the so-called protein corona, which can lead to blockage of the binding sites and consequently decrease the sensitivity of nano-biosensors.[11,15] Thus, further optimization of biosensors commonly faces two major challenges: 1) promoting specific binding of the desired detection entity, while 2) preventing nonspecific protein adsorption.

On the one hand, specific binding can be favored by the use of both covalent and non-covalent immobilization of proteins at the surface of the biosensors.[163,167,168] In addition to immobilization, the binding sites of the proteins need to be accessible for proper targeting.[166–168] Thus, the orientation of the immobilized proteins at the

surface is of paramount importance[166,167] as has been recently shown, by comparing nanoparticles covered by "favorably" oriented physisorbed proteins with "unfavorably" chemisorbed ones.[166,169] On the other hand, nonspecific protein adsorption is commonly reduced by additional protein-repelling functionalization, for instance using poly(ethylene glycol) (PEG).[165,167,168,170] However, even though unspecific protein adsorption is reduced with PEG, it is known that the protein adsorption is not fully prevented at the surface of PEGylated nanoparticles.[25] Furthermore, we have recently shown that the PEG packing density controls the fibrinogen (Fbg) orientation at the surface.[156]

Since PEG influences both the orientation of adsorbed proteins as well as the nonspecific protein adsorption, it is important to understand the potential of protein-repelling materials for biosensor applications. Here, we compare two protein-repelling polymers, PEG and a member of the polyphosphoester (PPE) polymer family poly(methyl ethylene phosphate) (PMEP), in terms of their protein specific repellency and their influence on the protein orientation at the surface. PPEs have been established as good alternatives to PEG coatings for nanoparticles to reduce protein adsorption.[25,34] We have found that both PEG and PMEP seem to be unable to fully prevent fibrinogen and albumin adsorption, when used at surface densities commonly used in nanoparticle coatings, but rather promote the formation of a protein corona.[156,171] In this work, we compare and contrast these two polymers, in terms of their interactions with proteins. We use a combination of surface pressure measurements and surface sensitive vibrational sum-frequency generation spectroscopy (SFG) to study differences in the specific protein-repelling properties of the polymers. Furthermore, by combining the experimental data with calculated SFG spectra, we obtain the orientation of the proteins adsorbed on the individual surfaces.

5.2 Experimental

In our experiments, we use model systems consisting of polymers, modified with an alkyl chain to render them surface active, so that monolayers can be formed at the air/aqueous phosphate buffered saline (PBS) subphase (pH 7.4). The nonionic surfactants used in this work are a PEG derivative, Lutensol AT50 (BASF Germany), and a PPE surfactant, PMEP (see Figure 5.1), which was synthesized and characterized according to Refs. [33, 33, 171]. We use Brewster angle microscopy (BAM) to
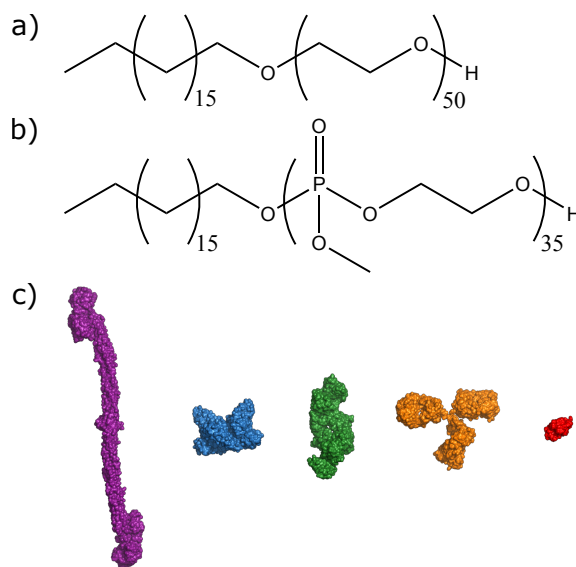
Figure 5.1: Chemical structures of the surfactants a) Lutensol AT50 and b) PMEP. c) From left to right: Crystal structures of Fbg (PDB code 3GHG), HSA (PDB code 1AO6), Tf (PDB code 2HAV) and IgG (PDB code 1IGT) and Lys (PDB code 1DPX) drawn to scale.

study the conformation of the polymeric monolayers, as described in Ref. [171]. To investigate the surfactant-protein interactions, small volumes of highly concentrated human fibrinogen (Fbg), human serum albumin (HSA), transferrin (Tf), immunoglobulin G (IgG) or lysozyme from hen egg white (Lys) solutions are injected into the subphase of the monolayers, to a final protein concentration of ∼0.1 mg/ml. The proteins represent a variety of natural proteins with different functions, sizes and isoelectric points (see Table 5.1). Furthermore, we use a chemically modified cationic HSA (cHSA) as described in Ref. [172]. More details about the sample preparation and the experiments can be found in section 5.5.

In the experiments, we combine surface pressure measurements and vibrational sum-frequency generation (SFG) spectroscopy to investigate the protein adsorption behavior onto the two different surfactant monolayers Lutensol and PMEP, respectively. The surface pressure measurements are sensitive to adsorption of proteins at the interface, while SFG spectroscopy is a second-order nonlinear optical spectroscopy, which is surface selective due to symmetry selection rules, and has been frequently used to obtain information conformation and orientation of proteins at interfaces.[106,107,116,118,149–152,173]

Table 5.1: Characteristics of the used proteins. [a] The estimated charge at pH 7.4 is calculated with the protein calculator v3.4 (http://protcalc.sourceforge.net/).

Protein	M_W in kDa	Isoelectric point (IEP)	Estimated charge at pH 7.4	PDB code
Fbg	~ 326	~ 5.5	-15.2	3GHG
HSA	~ 66	~ 4.8	-16.1	1AO6
Tf	~ 75	~ 6	-3.0	2HAV
IgG	~ 150	~ 7.5	$+0.2$	1IGT
Lys	~ 14	~ 11	$+7.3$	1DPX

5.3 Results and discussion

We prepare monolayers of Lutensol and PMEP on a PBS subphase using a mean molecular area of 5 nm^2, similarly to the polymer density used at the surface of nanoparticles.[25,34] Characterization of the monolayers via BAM (see Ref. [171] and section 5.5) shows, that even though at this packing density both polymers are beyond the transition point from mushroom to more brush-like conformation, they are unlikely to be in a fully extended conformation. The two monolayer systems also show similar hydration characteristics (see section 5.5 for more details on the monolayer hydration characterization), which is an important factor since conformation and hydration of the polymers are known to determine their ability to repel proteins.[26,31,37,44,174] Next, small volumes of the different protein solutions are injected into the subphase, to study the protein adsorption behavior.

Protein adsorption. Figure 5.2 shows the time evolution of the normalized surface pressure for the PMEP and Lutensol monolayers. Injection of Fbg, HSA, or Tf induces an increase in the surface pressure over time, suggesting adsorption of these proteins onto both PMEP and Lutensol monolayers. While there seems to be a difference in the affinity of HSA and Tf toward Lutensol and PMEP, Fbg seems to adsorb onto the two surfaces with equal strength. Furthermore, IgG and Lys seem to be repelled by both Lutensol and PMEP as no increase in the surface pressure is observed in the 45 minutes after injection.

In principle, the protein size could be a possible explanation of why some proteins could be repelled, while others adsorb: small proteins can penetrate the polymer barrier, while this is energetically more costly for bigger proteins. However, in our
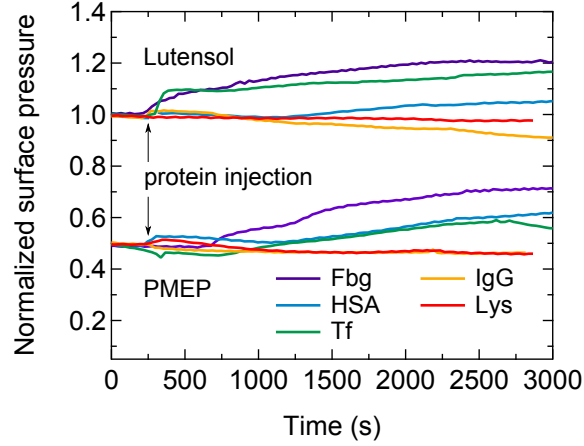
Figure 5.2: Normalized surface pressure of the Lutensol and PMEP monolayer on PBS after injection of the Fbg (purple), HSA (blue), Tf (green), IgG (orange) and Lys (red) into the subphase at time $t \sim 250s$. The PMEP measurements are offset vertically for clarity.

experiments we observe, that the smallest protein (Lys) is repelled, whereas the largest one adsorbs (Fbg). Therefore, protein size does not appear to be the key parameter governing the adsorption behavior of proteins onto PMEP and Lutensol. It seems instead, that the protein adsorption is correlated to their isoelectric point (IEP): negatively charged proteins (IEP $<$ 7.4: Fbg, HSA, and Tf) adsorb, while positively charged ones (IEP $>$ 7.4: IgG and Lys) are repelled. To further test this hypothesis and keep other parameters constant, we choose to use a chemically modified cationic HSA (cHSA). With this modification, the overall changes to the system are minimal, as only the protein surface is changed. Figure 5.3 shows the surface pressure measurements after injection of cHSA into the subphase of the two different monolayers. As can be seen, the positively charged cHSA adsorbs onto both polymer monolayers. This leads us to the conclusion that the protein charge also does not seem to determine protein adsorption onto Lutensol and PMEP. However, since protein adsorption is very complex, we cannot rule out other contributing factors such as the structural rigidity of the proteins or the charge and/or hydrophilicity distribution of specific protein domains.

Protein orientation. In the next step, we investigate whether the adsorption of Fbg, HSA, and Tf also occurs in an ordered manner, by collecting the SFG spectra in the amide I region. Figure 5.4 shows the SFG spectra before (black) and after
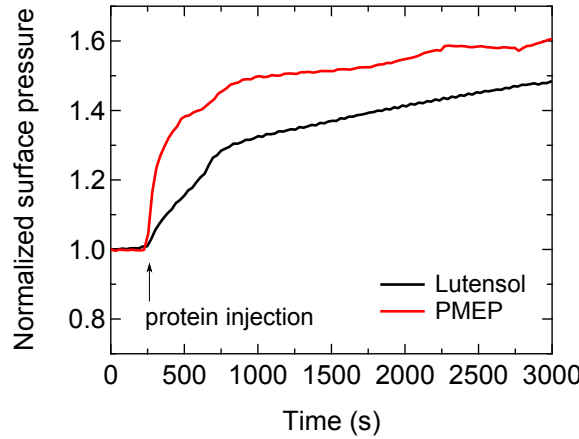
Figure 5.3: Normalized surface pressure of Lutensol (black) and PMEP (red) monolayers on PBS after injection of the cHSA solution into the subphase at time $t \sim 250s$.

(colored) injection of either Fbg, HSA or Tf into the subphase of the Lutensol and PMEP monolayer, respectively. Here, the general behavior of the proteins at the two different surfaces is very similar. Without proteins present in the subphase, no distinct peak is present in the amide I region between 1600 and 1700 cm^{-1} for either monolayer. In presence of Fbg, HSA and Tf (see figure 5.9 in section 5.5 for a zoom-in of the spectra) a broad peak around 1660 cm^{-1} appears, which is assigned to α-helices in the secondary structure of the proteins. Additionally, in case of Fbg a shoulder at around 1690 cm^{-1} is present, which stems from β-sheet structures.[171] The presence of the amide I peaks in the SFG spectra indicate that Fbg, HSA and Tf adsorb in an ordered manner onto these polymers, as randomly oriented proteins cannot contribute to the SFG intensity.

Despite the so far observed similarities in the protein-repelling behavior of Lutensol and PMEP, there is one distinct difference: the overall SFG signal intensity in the amide I region generated by HSA and Fbg. This can have several origins, namely differences in 1) the amount of adsorbed protein, 2) protein orientation, and 3) protein conformation at the two surfaces or any combination of the above-mentioned factors. In the case of HSA, it seems likely that differences in the amount of adsorbed protein are responsible for the differences in the SFG intensities, as also observed in the surface pressure measurements. For Fbg on the other hand, the initial surface pressure is comparable for Lutensol and PMEP ($\sim$11 mN/m), as is the relative change ($\sim$2.5 mN/m). This suggests that similar amounts of Fbg adsorb onto both surfaces. Consequently, we conclude that the differences in the SFG
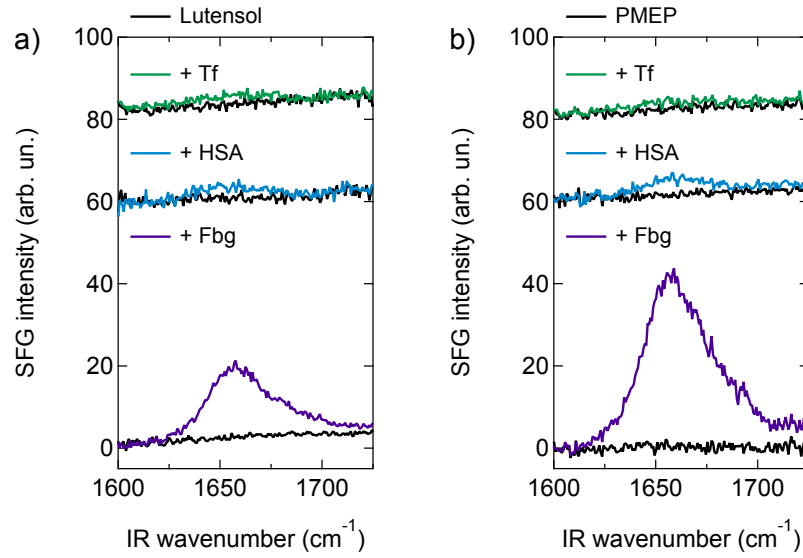
Figure 5.4: SFG spectra in the Amide I region in the absence (black) and presence of 0.1 mg/ml protein in the subphase of the a) Lutensol and b) PMEP monolayers, respectively. The curves in are offset vertically for clarity. The mean molecular area for both monolayers is 5 nm^2.

signal intensities cannot be explained by different amount of adsorbed protein. This leaves changes in protein orientation and/or conformation as possible explanations. Previous studies on the Fbg adsorption on other hydrophilic surfaces showed that Fbg can obtain various conformations upon adsorption.[117,132,175,176] However, the most common conformations in all these studies show bending of the protein which is very close to the crystalline structure of Fbg. Moreover, changes in the secondary structure of Fbg upon adsorption onto the polymer surfaces should be reflected in changes of the spectral shape of the amide I SFG signal. This is not observed in our study, where the normalized SFG spectra of Fbg adsorbed onto Lutensol and PMEP have the same shape (see Figure 5.10 in section 5.5). We thus assume in the following that the Fbg conformation is mainly preserved upon adsorption on the two polymers.

Insights on the protein orientation at the surface can be obtained through the collection of SFG spectra in different polarization combinations,[61,62] even more so when this is combined with calculated spectra.[133,148] Details on the calculation of the SFG spectra can be found in section 5.5. Figure 5.5 shows the experimental and calculated SFG spectra in the amide I region for Fbg adsorbed on Lutensol and PMEP in *ssp*, *ppp* and *sps* polarization combinations, respectively. The calculated SFG
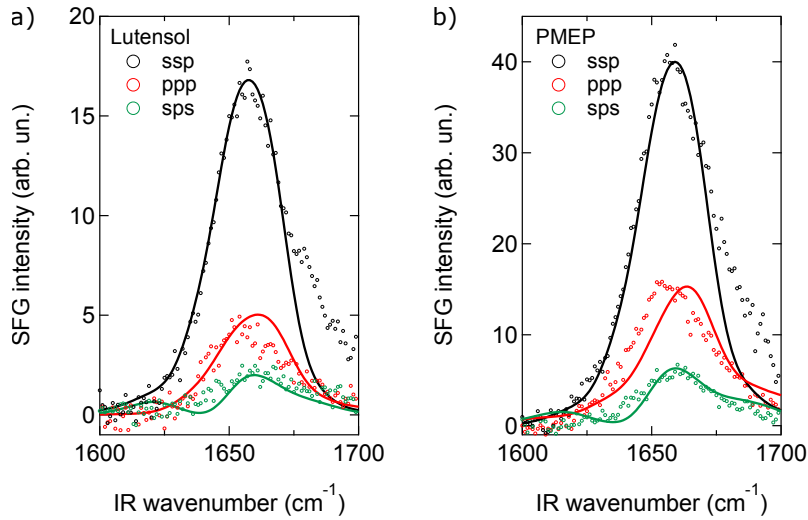
Figure 5.5: SFG spectra in the Amide I region of 0.1 mg/ml Fbg in *ssp* (black), *ppp* (red) and *sps* (green) polarization at the a) Lutensol and b) PMEP monolayer. The full lines represent the calculated SFG spectra for Fbg at the Lutensol and PMEP monolayer, respectively. The mean molecular area for both monolayers is 5 nm^2.

spectra (using PDB structures) reproduce the spectral shape and center position of the experimental protein peaks very well, in agreement with a preserved protein structure upon adsorption. Moreover, the calculation results show that the overall orientation of Fbg is different for the two surfaces. The calculated tilt angles of Fbg with respect to the surface normal are ∼31°and ∼16° at the Lutensol and PMEP monolayer, respectively (see Figure 5.12 in section 5.5). Therefore, Lutensol and PMEP seem to induce different orientations for the adsorbed Fbg, at the surface density usually used to coat nanoparticles

5.4 Conclusions

In conclusion, our results show no qualitative difference between PEG and PMEP in their likelihood to allow specific adsorption among the different proteins tested in this work. And, as an aside, we were also able to rule out protein size and net charge as possible factors governing the adsorption. However, a clear difference was observed in the manner Fbg orients on the two polymer surfaces. This finding can be important for potential biosensor applications, as it shows that a single surface functionalization can be sufficient to induce orientation of specific proteins upon

adsorption, while it suppresses unspecific adsorption of some other proteins at the same time.

5.5 Supplementary Information

Monolayer preparation and surface pressure measurements

PMEP and Lutensol are dissolved in a 9:1 (v/v) mixture of high purity chloroform (VWR Chemicals) and methanol (VWR chemicals) to obtain solutions with 50 μM concentration. Subsequently, the surfactants are spread on a phosphate buffered saline (PBS, Sigma Aldrich, pH 7.4) subphase. The mean molecular area per surfactant at the surface for all measurements is 5 nm^2 and was calculated by tracking the number of molecules present at the surface and the area they occupy. For comparison, the functionalized polystyrene nanoparticles in literature have a particle radius $r \sim 50$ nm with roughly $N \sim 5 \cdot 10^3 - 1 \cdot 10^4$ functionalized groups at the surface.[25,34,162] Assuming perfect spheres, this results in a particle surface area A_{NP} of: $A_{NP} = 4\pi r^2 = 3.14 \cdot 10^4$ nm^2. The resulting mean molecular area of one functional group is then $3.14 - 6.28$ nm^2. For the protein adsorption studies $\sim$100 μl of highly concentrated solutions of either fibrinogen (Fbg, Sigma Aldrich), human serum albumin (HSA, Sigma Aldrich), transferrin (Tf, Sigma Aldrich), immunoglobulin G (IgG, antibodies-online GmbH) or lysozyme from hen egg white (Lys, Roche) dissolved in PBS buffer solution are injected into the subphase to reach a final protein concentration of $\sim$0.1 mg/ml. The proteins and phosphate buffered saline tablets are used as received. During the SFG experiments, the surface pressure is simultaneously monitored during all measurements using a DeltaPi tensiometer (Kibron, Finland).

Monolayer hydration

Figure 5.6 shows the SFG spectra in the OH-stretch region of both monolayers. The spectra have two distinct bands, one at $\sim$3200 cm^{-1} and another one at $\sim$3400cm^{-1}, comparable to other protein repelling materials reported in literature.[109,112–114] The SFG intensity for Lutensol and PMEP increases as compared to the plain air/water interface, suggesting substantial ordering of water molecules induced by the surfactants. The effect on the net reorientation of water molecules from PMEP is apparently stronger as compared to Lutensol, as can be seen from the overall higher
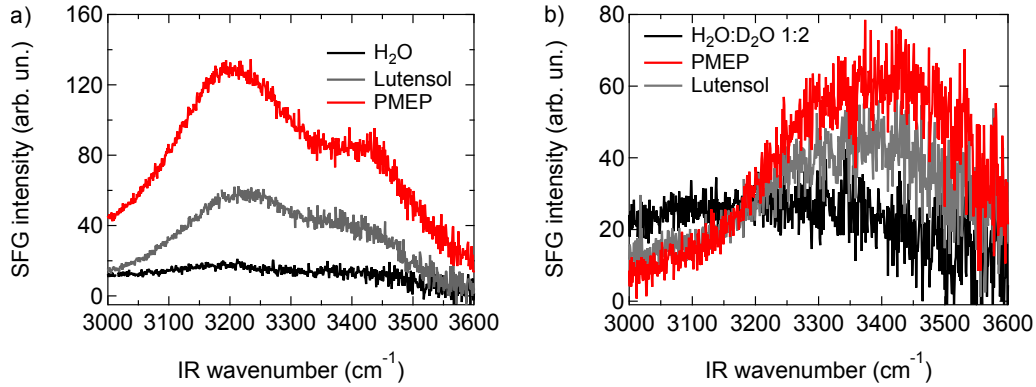
Figure 5.6: SFG spectra in the OH-stretch region of the plain air/water interface (black) and covered with monolayers of Lutensol (gray) and PMEP (red) on a) a plain H_2O and b) an isotopically diluted H_2O:D_2O 1:2 (v/v) subphase. In both measurements, the mean molecular area for the monolayers is 5 nm^2.

SFG signal intensity. A possible explanation for this could be the fact that PMEP has more hydrogen bonding donor sites than Lutensol.

By comparing the intensities and the first moments of spectral distribution (center of mass, COM) of the different spectra, we can get information on the degree of water alignment at the surface and the average hydrogen bonding strength of interfacial water molecules. The lower the COM of the SFG spectra in the OH-stretch region, the stronger is the interaction of interfacial water molecules with the surfactant. The calculated COMs for Lutensol and PMEP on the pure H_2O subphase are 3282 cm^{-1} and 3284 cm^{-1}, respectively. Therefore, the average hydrogen bonding strength of the water molecules is equivalent within the two monolayers. Strictly speaking, the interpretation of SFG spectra on a pure water subphase can be challenging since they are influenced by inter- and intramolecular coupling of the water molecules.[158,159] However, the conclusion of equal hydrogen bonding strength of water at Lutensol and PMEP is further supported by measurements on an isotopically diluted water subphase (see Figure 5.6b), where the contributions from inter- and intramolecular coupling are suppressed. In this case the COMs of the two systems are again quite close to each other: 3333 cm^{-1} and 3356 cm^{-1} for Lutensol and PMEP, respectively. So, apart from the overall stronger net orientation of water molecules at the PMEP surface as compared to Lutensol, there seem to be no major differences in the interaction between water molecules for these two polymers.

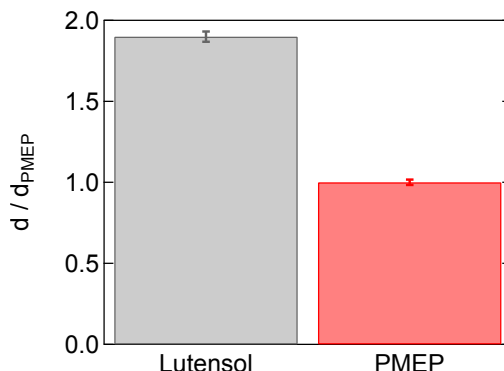**Monolayer thickness and polymer conformation**

Figure 5.7: Relative thickness of the Lutensol (gray) and PMEP (red) monolayer on PBS normalized on the thickness of PMEP. The error bars represent the standard errors for different measurements on the same sample. The mean molecular area for both monolayers is 5 nm^2.

The polymer chains could assume different conformations upon interaction with water, which would result in different monolayer thicknesses. Therefore, we measured the relative thickness of the Lutensol and PMEP monolayers using BAM, as shown in Figure 5.7. For thin films the reflected intensity in BAM scales in first approximation with the square of the layer thickness. Details can be found in chapters 2 and 4. Both Lutensol and PMEP do not possess optical transitions at the BAM laser wavelength, therefore we assume an identical, purely real-valued refractive index for the two monolayers as done earlier for different members of the PPEs family.[171] The Lutensol layer is roughly twice as thick as the PMEP layer, as inferred from the relative reflected intensities of $(6.0 \pm 0.8) \cdot 10^{-8}$ and $(1.7 \pm 0.8) \cdot 10^{-8}$, respectively. This could indicate different conformations of the polymers at the interface. For the given packing density with a mean molecular area of 5 nm^2, the mean distance between two molecules is $d \sim 2.2$ nm. In comparison, the Flory radii R_F and brush thickness L of Lutensol and PMEP using monomer sizes of 0.39 nm and 0.6 nm are depicted in table 5.2. Since the average distance between two molecules is smaller than the Flory radius of the polymers, it is likely that both polymers do not adopt a pure mushroom conformation. However, since the Flory radii of the two polymers are quite similar and the packing densities are identical, they are likely to present similar conformations.

Table 5.2: Comparison of the experimentally determined monolayer thickness from BAM on the PBS subphase with the theoretically expected values for the mushroom size (Flory radius R_F) and the brush thickness L. The refractive index of the PBS subphase is 1.336 and the refractive index for the monolayers is assumed to be 1.35.

Material	Calculated layer thickness (nm)	Theoretical Flory radius R_F (nm)	Theoretical brush thickness L (nm)
Lutensol	5.1 ± 1.1	4.1	6.2
PMEP	2.7 ± 0.7	5.1	8.7

Monolayer surface coverage

Furthermore, to show that the monolayers fully cover the air/PBS interface, we measure the dangling OH peak. The SFG spectra in Figure 5.8 show that the peak at ~ 3700 cm^{-1} disappears for both Lutensol and PMEP monolayers. The dangling OH peak is a typical feature of the neat air/water interface, therefore the data suggest that monolayers are formed which fully cover the surface.
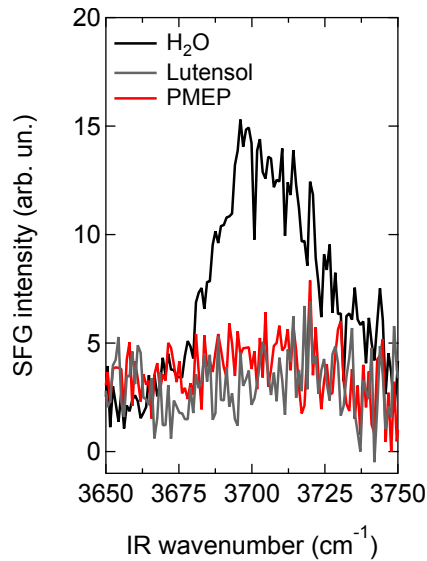
Figure 5.8: SFG spectra in the dangling OH-region for the plain air/water interface (black) and covered with Lutensol (gray) and PMEP (red) monolayers. The mean molecular area for the monolayers is 5 nm^2.

Further supporting SFG measurements
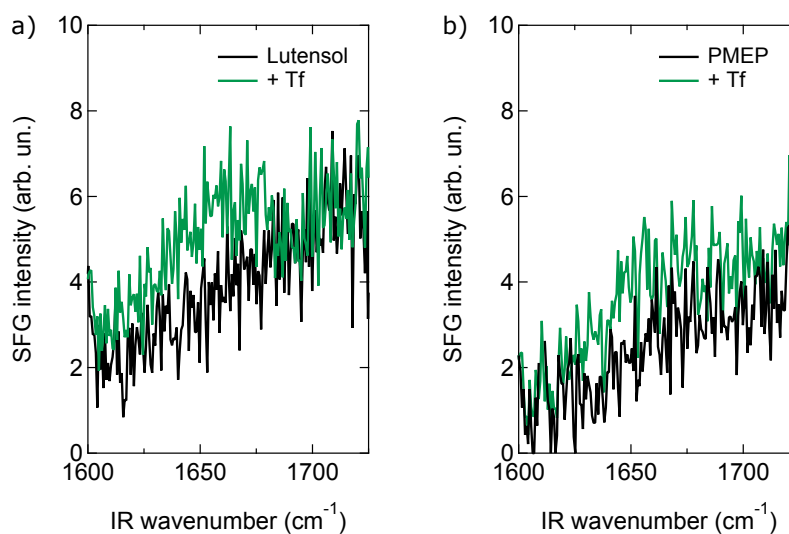
Figure 5.9: SFG spectra in the amide I region of a) Lutensol and b) PMEP in the absence (black) and presence (green) of 0.1 mg/ml Tf in the subphase. The mean molecular area for the monolayers is 5 nm^2.
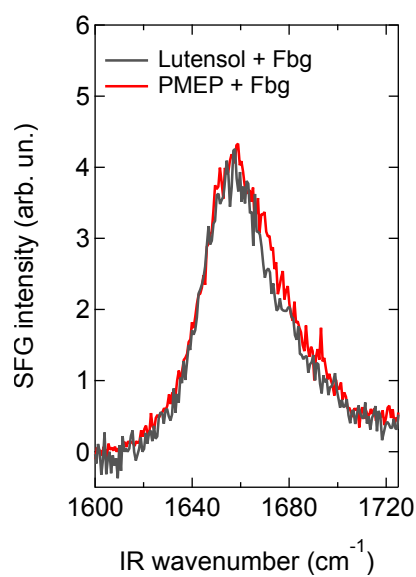
Figure 5.10: SFG spectra in the amide I region of Fbg adsorbed to Lutensol (gray) and PMEP (red). The spectra are normalized to their maximum intensity and the contribution from the pure monolayers in the absence of protein in the subphase are subtracted.
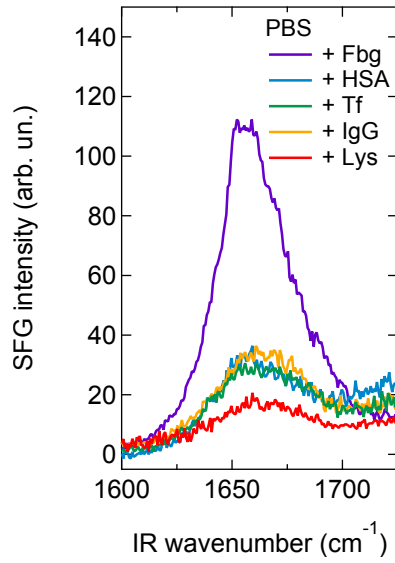
Figure 5.11: SFG spectra in the amide I region for 0.1 mg/ml Fbg (purple), HSA (blue), Tf (green), IgG (orange) and Lys (red) in PBS.

The SFG spectra in Figure 5.11 show the amide I region of the individual protein solutions in PBS. The presence of the amide I peak around 1660 cm^{-1} shows that all proteins adsorb in an oriented way to the plain air/PBS interface.

Calculation of vibrational SFG spectra

The calculations in this chapter are performed as described in chapter 3: We average over Φ and Ψ due to the azimuthal isotropy and thus the spectra are mainly influenced by the tilt angle Θ of the protein with respect to the surface normal. The molecular axis of the proteins is reproducibly defined by aligning them according to their moments of inertia, using the orient script in VMD. In order to correct the calculated spectra for the Fresnel coefficients at the respective wavelengths, we use the following refractive index values for both Lutensol and PMEP monolayers: $n_{SFG} = 1.18$, $n_{VIS} = 1.18$, and $n_{IR} = 1.41$, respectively. The best fits for the orientation of Fbg at the Lutensol and PMEP surface result in tilt angles of $\Theta \sim 31°$ and $\Theta \sim 16°$, respectively. The obtained orientations of Fbg at the individual surfaces are shown in figure 5.12.
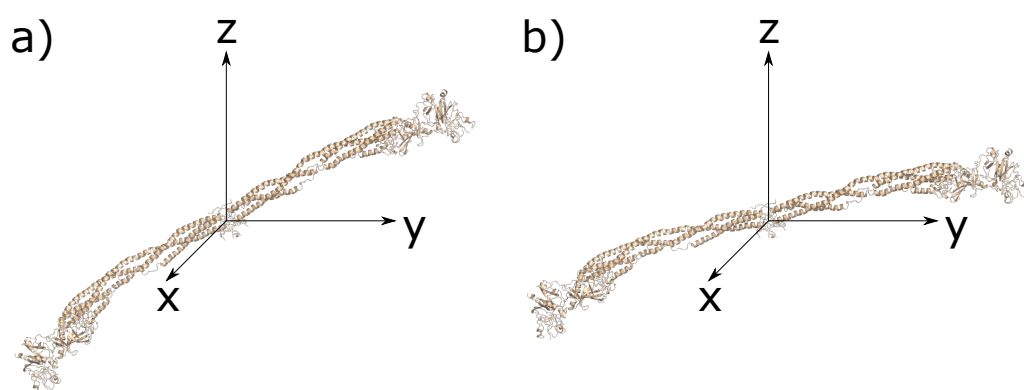
Figure 5.12: Fbg in the molecular frame with the calculated orientation at the a) Lutensol ($\Theta = 31°$) and b) PMEP ($\Theta = 16°$) surface.

6 Quantification of Protein Adsorption on Nanoparticle Surfaces

Contributions to this chapter: C. Bernhard and G. Gonella designed the research project. C.B. built the SHS setup, performed the characterization, and some of the SHS measurements. A. Bunn performed the SHS, DLS, and ζ-potential measurements. C.B. and G.G. analyzed the results. C.B., M. Bonn and G.G. discussed the results and contributed to the manuscript.

6.1 Introduction

As already widely discussed in the previous chapters of this thesis, functionalized nanoparticles have found a broad range of applications for biomedical purposes. In the work presented in the previous chapters, we have gained an insight into protein adsorption onto planar model surfaces that mimic the surface of these nanoparticles. The next natural step toward more realistic systems would be the characterization of the interaction of proteins with nanoparticle surfaces *in situ*. Second-order nonlinear optical techniques such as vibrational SFG spectroscopy or SHG are intrinsically surface specific and as such in principle ideal techniques to investigate interactions at interfaces. However, because of the comparable size between the object of interest and the used wavelength of these optical techniques, it is impossible to simply apply these methods to investigate nanoparticle surfaces in the same way they are applied to planar surfaces.[74] As in the case of their linear optical counterparts, this hurdle can be overcome by nonlinear light scattering methods, such as second-harmonic (SHS) or sum-frequency light scattering (SFS), which combine the surface specificity intrinsic to the nonlinear optical techniques with a scattering geometry and have been successfully employed to probe nanoparticle surfaces *in situ*.[72–74,82,177] More specifically, SHS has been used in resonant and non-resonant conditions to characterize nanoparticle dispersions and the adsorption of molecular species. Res-

onant SHS relies either on resonances of the nanoparticles, such as for example the localized surface plasmon of metallic nanoparticles,[178–183] or on (electronic) resonances of the adsorbate.[79,184–189] Therefore, resonant SHS is necessarily limited in the types of nanoparticles and adsorbates that can be studied, given the constraints of conventional laser wavelengths. On the other hand, non-resonant SHS, while lower in signal intensity as it is not enhanced by resonances, provides a broader variety of potential applications. So far, non-resonant SHS has been used to study charged colloidal dispersions and screening of the surface charges.[190–195] On planar surfaces, non-resonant SHG has also been used to investigate the apparent screening of polycations and proteins on charged silica surfaces.[196,197]

Here, we develop a non-resonant SHS method to investigate the adsorption of proteins on the surface of nanoparticles. More specifically, we use non-resonant SHS to study the adsorption of blood proteins on negatively charged polystyrene (PS) nanoparticles with different surface functionalization and sizes. By combining the experimental SHS data with a simplified adsorption model, namely a modified Langmuir model, we obtain information on the maximum amount of adsorbed protein per nanoparticle, the apparent binding constant and thus the apparent Gibbs free energy.

The SHS setup described in chapter 2 was constructed during this work. Consequently, we first carried out several tests to assure the proper performance of the setup, which will be discussed in the following section. Afterward, we explain the theoretical background for the developed non-resonant SHS method, before discussing the results from protein adsorption studies on the nanoparticle surfaces.

6.2 Tests of the new SHS setup

This section contains the characterization of the laser source, the setup alignment, and checks on the surface specificity of the method and second-order non-linearity of the detected signal.

Characterization of the laser source

First, we examine the output of the fundamental laser source. Figure 6.1 shows the spectra of the fundamental laser beam and the SH spectrum obtained by converting the fundamental with a barium borate (BBO) crystal. The spectra were
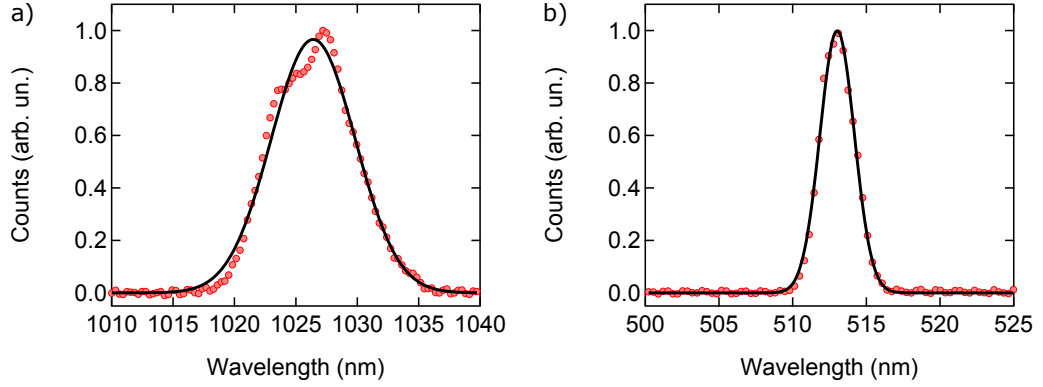
Figure 6.1: a) Spectral beam profile of the fundamental Pharos laser output. b) SH spectrum generated with a BBO crystal. The black curves represent Gaussian fits to the measured data points.

collected with a fiber spectrometer (AvaSpec 3648, Avantes, Netherlands). The black curves represent Gaussian fits to the data points. The fundamental and SH beam have a center wavelength of $\lambda_f = 1026$ nm and $\lambda_{SH} = 513$ nm, respectively. The full width at half maximum of the fundamental and SH beam are $\Delta\lambda = 8.1$ nm and $\Delta\lambda = 3.2$ nm, respectively. For the fundamental beam this corresponds to $\Delta\nu = 2.38 \cdot 10^{12}$ Hz in frequency domain. Furthermore, the pulse duration of the fundamental beam was measured with an autocorrelator (PulseCheck, A.P.E., Germany). Assuming a Gaussian temporal beam profile, the pulse duration results to be $\tau = 210$ fs. The time-bandwidth-product of the fundamental beam is therefore calculated to ∼0.48, which is close to the theoretical minimum value of ∼0.44 for Gaussian pulses. Thus, we conclude that the laser source presents good pulse quality, which is close to that of a transform-limited pulse.

Setup alignment and polarization sensitivity

Next, to assure correct alignment of the SHS setup, we use the hyper-Rayleigh scattering (HRS) signal from water. Generally, water is regarded as an isotropic liquid and therefore, in the electric dipole approximation, is not expected to produce a coherent SH signal. Nevertheless, in the experiments, a background signal from water is observed. This signal is caused by orientational and density fluctuations of the water molecules in the solution and referred to as HRS, as explained in section 1.5.3.[75] As HRS is an incoherent contribution to the overall detected signal, it can simply be subtracted from the measurement data, as described in section 1.5.3. Be-
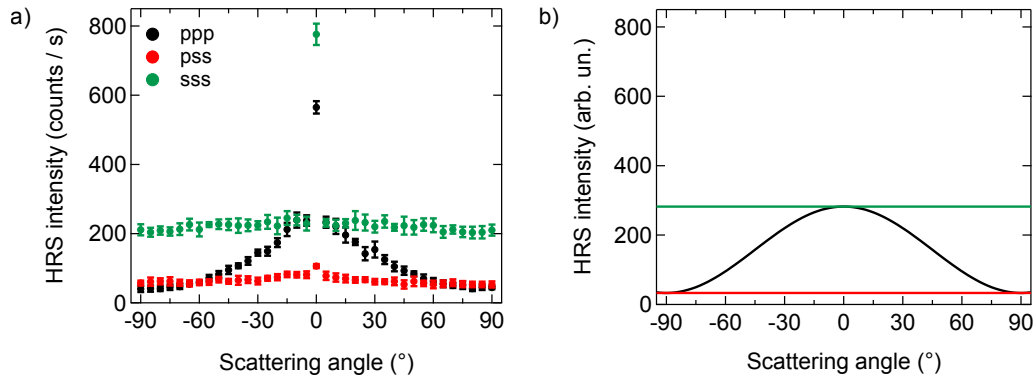
Figure 6.2: a) Experimental and b) theoretical HRS patterns of water in *ppp*, *pss*, and *sss* polarization combinations.

cause of symmetry considerations, the angle-dependent HRS (as well as SHS) signal from water is expected to be symmetric around 0 degrees (relative to the propagation direction of the fundamental beam), which is used here as reference to check the alignment of the setup. In figure 6.2 the experimental and theoretical (according to Ref. [198]) HRS patterns of water in *ppp*, *pss* and *sss* polarization combinations are shown. Please note, the polarization combination is assigned in the same way as for SFG, from high to low frequencies: The first letter represents the SH signal, while the last two indicate the polarization state of the fundamental beam. It is apparent that all experimental scattering patterns possess a peak intensity at a scattering angle of 0 degrees, which is generated from SH light produced in the optical components of the detection arm. Therefore, the data point at 0 degrees is not considered for further analysis. The *ppp* polarization combination scattering pattern shows a minimum at ±90 degree, which is in agreement with the theoretically predicted shape.[198] Furthermore, the theory also predicts that the SH intensity at ±90 degrees for *ppp* and *pss* polarization combinations should be identical, which is also observed in the experimental data in figure 6.2. The HRS intensities for *sss* and *ppp* polarization combinations are also the same for angles close to zero, also in agreement with the theory. Moreover, this indicates a correct polarization sensitivity of the setup. The shapes of the scattering patterns for all polarization combinations also nicely match the experimental observations previously reported in Refs. [85, 199].

Finally, from theoretical considerations, it is expected that the scattered light intensity in *sss* polarization combination is independent of the scattering angle, whereas
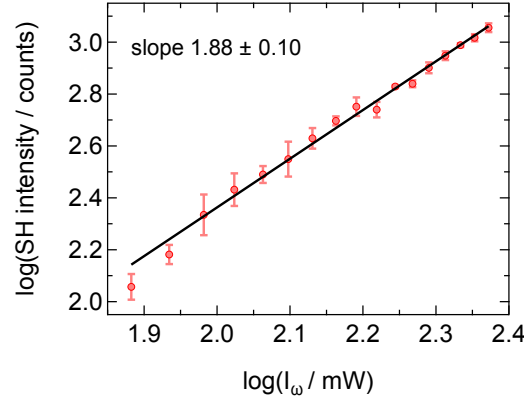
Figure 6.3: Dependence of the HRS signal from H_2O in *sss* polarization combination intensity on the power of the fundamental laser beam (from 76 to 235 mW) at a scattering angle of 90 degrees. The black curve is a linear fit to the measured data points on the double logarithmic scale.

the experimental data show a slight increase in HRS intensity for scattering angles close to the forward direction of the fundamental beam. Thus, we normalize our data (see SHS data treatment in section 1.5.3) to correct for this difference.

Power dependence of HRS

Generally, the generation of nonlinear optical processes requires high photon densities. However, depending on the actual photon density, the observed scattered signal can also include contributions from other nonlinear optical effects. By using narrow-band filters in the detection path and a narrow gating window for the detector, we assure that only photons in the frequency range of SHG are detected and unwanted contributions from two-photon fluorescence are suppressed. Furthermore, to make sure that the measured response is truly a second-order nonlinear process, we measure the dependence of the signal intensity on the fundamental laser power. In a second-order nonlinear process, the detected SH intensity is expected to depend quadratically on the power of the fundamental laser source. Figure 6.3 shows the dependence of the HRS signal of H_2O in *sss* polarization combination on the fundamental power in a double-logarithmic plot in a range from 76 to 235 mW. The fit to the data shows a slope of 1.88 ± 0.10, which is in good agreement with the theoretically expected quadratic dependence.
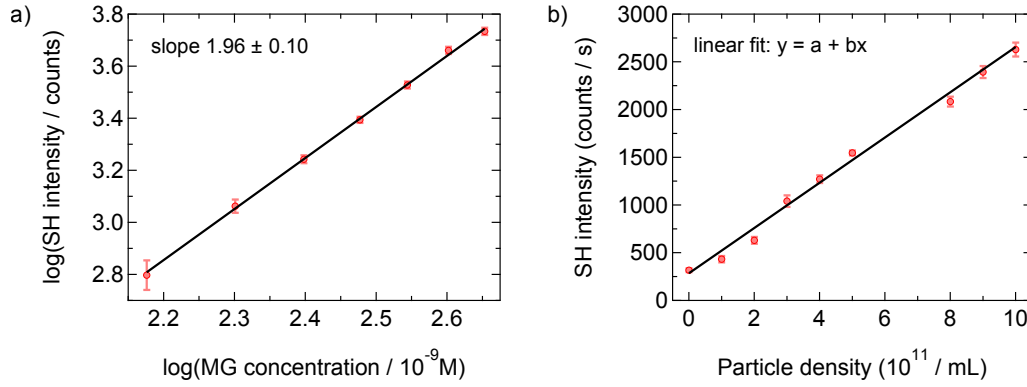
Figure 6.4: Dependence of the SHS signal intensity on a) the MG concentration in the solution (from 150 to 450 nM) and b) the amount of dispersed PS nanoparticles (100 nm diameter) per volume. The black curves are linear fits to the measured data points (in figure a) on a double logarithmic scale). The measurements are performed at a detection angle of 90 degrees and in *ppp* polarization combination. The power of the fundamental before the sample is a) 149 mW and b) 205 mW, respectively.

Surface specificity of SHS

To validate that the detected SHS signal is coherently generated at the surface of the nanoparticles, rather than coming from bulk molecules in solution, we measured the dependence of the SHS intensity on the concentration of adsorbates in solution. Theoretically, for coherent SHG, the intensity of the SH light $I_{2\omega}$ scales with the square of the sum of all SH fields generated by ith adsorbed molecule $E_{i,2\omega}$:

$$I_{2\omega} \propto (\sum_{i=1}^{N} E_{i,2\omega})^2 \tag{6.1}$$

and N is the total number of molecules adsorbed on the nanoparticle. Thus, if the signal is coherently generated at the surface, the SHS intensity should depend quadratically on the density of adsorbed molecules, as described in section 1.5.3. We use negatively charged PS nanoparticles with a diameter of 1 μm at pH 4 and measure the SHS signal dependence on the concentration of cationic malachite green (MG) molecules in solution. MG presents a very broad electronic resonance at the second harmonic frequency and therefore gives rise to an enhanced resonant SHS signal.[72,184] Figure 6.4a shows the dependence of the normalized signal intensity on the MG concentration. The signal is normalized by subtracting the non-resonant SH signal generated by the PS nanoparticles in the absence of MG in the solution

and also two-photon fluorescence contributions from the pure MG solution. The fit to the data with a slope of 1.96 $\pm$ 0.10 shows an excellent agreement with the expected square law, as also reported in the past by Wang et al.[72] and suggests that most MG molecules adsorb to the nanoparticles.

Additionally, we investigate the dependence of the signal intensity on the density n of the PS nanoparticles. We use nanoparticles with a diameter of 100 nm in a range from 10^{11} - 10^{12} nanoparticles per milliliter, as shown in figure 6.4b. We observe a linear dependence of the SHS signal on the nanoparticle density, which indicates incoherent summation of the signal generated at the individual nanoparticles. In this case, the total emitted light $I_{2\omega}$ is proportional to the sum of the squared emitted fields $E_{j,2\omega}$ by the individual nanoparticles:

$$I_{2\omega} \propto n \cdot I_{j,2\omega} = \sum_{j=1}^{n} (E_{j,2\omega})^2 \tag{6.2}$$

where n is the total number of nanoparticles. Moreover, the average interparticle distance for the nanoparticle densities used here is in the range of 1.0-2.15 μm (assuming an average interparticle distance of $n^{-1/3}$). The linear dependence of the scattered intensity on the number of nanoparticles warrants that, within this nanoparticle density range, multiple scattering is not taking place in the sample solution.[199]

6.3 Theoretical background

Non-resonant SHG and SHS have been intensively used in the past to investigate charged planar and nanoparticle surfaces.[69–71,190–194,196,197,200] Commonly, second-order nonlinear optical processes are just considered to probe the interface. However, in presence of charged moietes at the surface in contact with water, the electrostatic field generated at the surface leads to reorientation and polarization of water molecules. This leads to breaking of the centrosymmetry and therefore also generates a contribution to the second-harmonic response from bulk molecules. Thus, the detected second-harmonic intensity is considered to depend not only on a surface (see section 1.5) but also a bulk contribution:[69,195,201]

$$I_{2\omega} \propto |[F_{eff}(qR)\chi^{(2)} + 2\Phi_0\chi^{(3)}(F_1(qR) + F_3(\kappa R, qR))]I_\omega|^2 \tag{6.3}$$

where $\chi^{(2)}$ depicts the susceptibility of interfacial molecules, whereas $\chi^{(3)}$ is the susceptibility from molecules in bulk solution which are aligned and polarized due to the static electric field induced by the charges at the surface. $F_{eff}(qR)$, $F_1(qR)$ and $F_3(\kappa R, qR)$ are scattering form factors: the former two depend on the scattering geometry and nature of the system (R is the nanoparticle radius and q the scattering wave vector), while the latter also on the surface charge (κ^{-1} is the Debye length, see below) of the nanoparticles according to nonlinear Rayleigh-Gans-Debye theory. [77,79,177,195,202] It has been found that the $\chi^{(3)}$ contribution, especially at low ionic strength, can significantly distort the scattering pattern. [195] Φ_0 is the electrostatic surface potential. For measurements at a fixed scattering angle and fixed ionic strength $F_{eff}(qR)$, $F_1(qR)$ and $F_3(\kappa R, qR)$ are constant.

Ions in the bulk solution in contact with charged interfaces form an electrical double layer (EDL), which is generated by the balance between electrostatics attracting the counterions close to the surface and entropy favoring counterions solvated in isotropic bulk condition. In case of spheres, and under the assumption of a diffuse EDL, the relationship between Φ_0 and the surface charge density σ_0 can be approximated with an empirical formula: [203]

$$\sigma_0 = \frac{2\epsilon_r \epsilon_0 \kappa k_B T}{ze} \left[\sinh\left(\frac{ze\Phi_0}{2k_B T}\right) + \frac{2}{\kappa R} \tanh\left(\frac{ze\Phi_0}{4k_B T}\right) \right] \tag{6.4}$$

Here ϵ_0 is the vacuum permittivity, ϵ_r the relative permittivity of the solvent, k_B is the Boltzmann constant, T the temperature, z the valence of the electrolyte, e the elemental charge and the Debye length κ^{-1} for a symmetric electrolyte with valence z:

$$\kappa^{-1} = \sqrt{\frac{\epsilon_0 \epsilon_r k_B T}{2000 N_A z e^2 c}} \tag{6.5}$$

with Avogadro's number N_A and the bulk electrolyte concentration c. Thus, the electric surface potential is intrinsically linked to the surface charge density, ionic strength, and temperature of the solution.

As a consequence, the non-resonant SHS, similarly to the SHG signal, is sensitive to changes of the surface charge density. In our study, these changes are induced by adsorption of proteins. Upon protein adsorption, the surface charge density σ_0 changes according to:

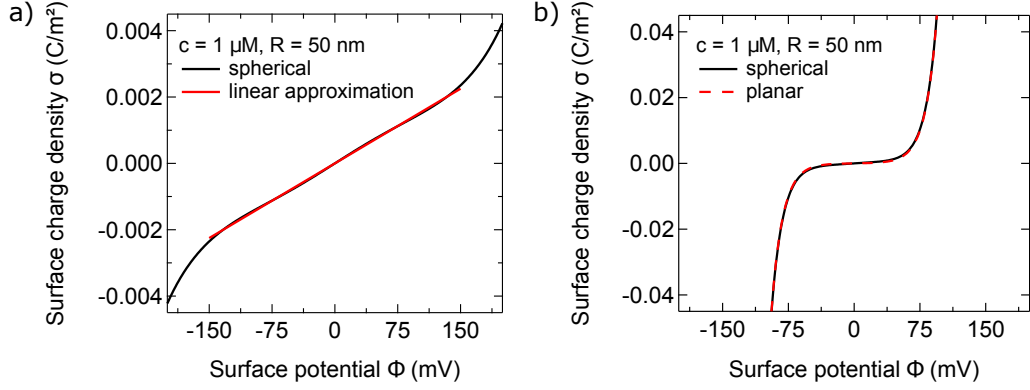$$\sigma_0 = \sigma_{Part} + \sigma_{Prot} \theta_{cov} \tag{6.6}$$

Figure 6.5: Surface charge density σ_0 as a function of the surface potential Φ_0 of the nanoparticles (black). a) Assuming a 1:1 electrolyte. The red curve represents a linear fit to the curve in the range from -150 to +150 mV. b) Assuming a 4:4 electrolyte to model the net negative charge of HSA (about -8.0) at pH 6.6. The red dashed line shows the function for planar surfaces in comparison.

with σ_{Part} the charge density of the bare nanoparticles, σ_{Prot} the charge density of the adsorbed protein at saturation and θ_{cov} the relative surface coverage of the protein.

Unfortunately, from equation 6.4 is not it is not possible to obtain an analytical inverse equation for Φ_0 as a function of σ_0. For small nanoparticle sizes and under low ionic strength conditions ($\sim 10^{-6}$ M of a 1:1 electrolyte), this can however be approximated with a linear behavior in the range from -150 to +150 mV for the surface potential, as shown in figure 6.5. For strongly charged proteins or electrolytes with higher valence, such as a 4:4 electrolyte for example, the curve can nicely be approximated with the function for planar surfaces (see figure 6.5b):

$$\sigma_0 = \frac{2\epsilon_0\epsilon_r\kappa k_B T}{ze} \ \sinh(\frac{ze\Phi_0}{2k_B T}) \tag{6.7}$$

which is easily invertible. This is also the case for large nanoparticles and/or high ionic strength conditions (see figure 6.10 in section 6.7). In the remainder of this chapter, we will use the linear approximation for the relation between Φ_0 and σ_0.

To describe the relative surface coverage θ_{cov} for a given protein concentration, here we use a modified Langmuir adsorption model. The classical Langmuir adsorption model neglects depletion of the adsorbing species in bulk. This is usually appropiate for flat surfaces, where the maximum amount of adsorbed molecules per unit volume N_{max} is much smaller than the bulk concentration c. However, this assumption

is not valid anymore for nanoparticle dispersion, where the total surface area can be very large. Therefore, we use a modified model to correct for this depletion.[184] Furthermore, the Langmuir model is based on four assumptions: i) all adsorption sites are equivalent, ii) each adsorption site can only bind one molecule, iii) the adsorbed molecules are non-interacting, and iv) the adsorption process is reversible. Strictly speaking, for protein adsorption on nanoparticle surfaces these assumptions are not always correct.[204–206]

However, the maximum amount of adsorbed protein can still be calculated from this simplified Langmuir model, whereas the binding constant can easily be underestimated.[204] With this in mind, in our analysis we will still use the modified Langmuir model. In this case the adsorption process is described as a reaction of a molecules, in our case a protein (P) with an empty surface site (ES), which returns a filled surface site (FS):

$$\text{ES} + \text{P} \underset{k_d}{\overset{k_a}{\rightleftharpoons}} \text{FS} \tag{6.8}$$

Here, k_a and k_d describe the adsorption and desorption rate constants, respectively. The resulting kinetic equation for this process is

$$\frac{dN}{dt} = k_a \frac{(c - N)}{M_{solv}}(N_{max} - N) - k_d N \tag{6.9}$$

with the amount of adsorbed proteins per unit volume N and the molarity of the solvent M_{solv}. All experiments in this thesis are performed in water, which has a molarity of 55.5. At equilibrium, the rates of adsorption and desorption are equal and therefore dN/dt vanishes. Then, the relative surface coverage θ_{cov} can be determined from equation 6.9:

$$\theta_{cov} = \frac{N}{N_{max}} = \frac{(c + N_{max} + M_{solv}/K) - \sqrt{(c + N_{max} + M_{solv}/K)^2 - 4cN_{max}}}{2N_{max}} \tag{6.10}$$

Here, $K = k_a/k_d$ is the equilibrium binding constant. Theoretically, there are two solutions to equation 6.9 since it is a quadratic equation. However, since the surface coverage θ_{cov} has to be in the range from 0 to 1, only the solution shown in equation 6.10 is physically meaningful. This simplified adsorption model enables access to the

maximum amount of adsorbed protein, as well as the binding constant. Furthermore, from the binding constant the Gibbs free energy ΔG^0 can be calculated:

$$\Delta G^0 = -RT \ln K \tag{6.11}$$

with the ideal gas constant R and the temperature T. As mentioned above, the Langmuir model can result in quite large uncertainties of the binding constant and therefore the Gibbs free energy. Thus, we will refer to the obtained values from the fits as "apparent" binding constant K_{app} and "apparent" Gibbs free energy ΔG^0_{app} in this thesis.

6.4 Experimental

For the SHS experiments we used commercial Polybead$^®$ (Polysciences Europe, Germany) and further carboxylate functionalized Polybead$^®$ nanoparticles. The nanoparticle diameters were 100 nm, 200 nm, and 500 nm, respectively, and the stock dispersions of 2.5 wt% were diluted prior to use with ultrapure water (resistivity $\sim$18 MΩ). The nanoparticle density for the SHS was adjusted to $\sim 4.55 \cdot 10^{11}$ ml^{-1}, $\sim 1.31 \cdot 10^{10}$ ml^{-1}, and $\sim 1.81 \cdot 10^9$ ml^{-1}, for the 100 nm, 200 nm, and 500 nm nanoparticles, respectively. Human serum albumin (HSA) and human fibrinogen (Fbg), transferrin (Tf), and sodium chloride were purchased from Sigma Aldrich (Germany) and used as received. Immunoglobulin G (IgG) was received from antibodies-online GmbH (Germany) and also used as received. The protein solutions were prepared in ultrapure water. After the addition of the protein solution, the nanoparticle dispersion was stirred with a magnetic stirrer for one minute. Stirring was turned off before the SHS measurements. The SHS setup is described in detail in chapter 2. The samples were prepared in quartz cuvettes (Hellma Analytics, Germany) with a diameter of 10 mm. The observed SHS signal intensity is solely generated by the nanoparticle dispersion in the focal volume and the walls of the quartz cell do not contribute (see figure 6.11 in section 6.7). All SHS measurements were performed at a room temperature of $(22 \pm 1)°$C. The angle-resolved SHS scattering patterns were measured with an acceptance angle of $\sim$3.4 degrees. For the SHS titration experiments at fixed detection angle, the acceptance angle was set to $\sim$13.5 degrees and the polarization combination is set to *ppp*. The integration time for all measurements is 1 s and each data point is averaged over a minimum of 10 measurements.
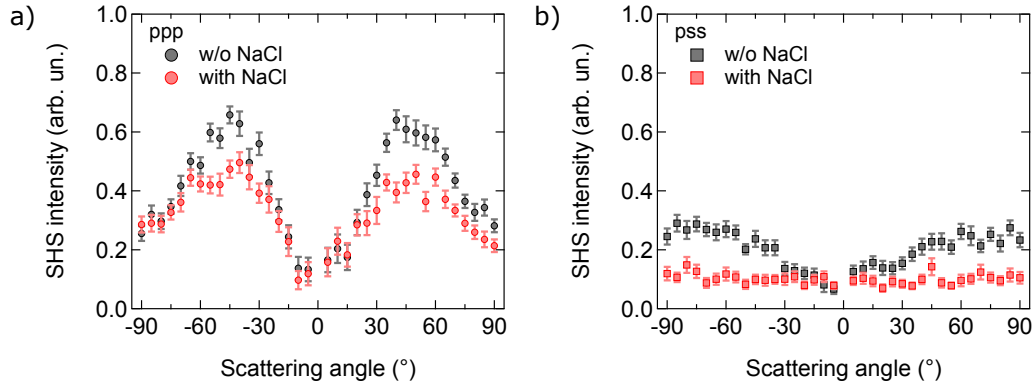
Figure 6.6: Angle resolved non-resonant SHS pattern for SDS stabilized PS nanoparticles with 100 nm diameter in a) *ppp* and b) *pss* polarization combination. The patterns were recorded for nanoparticles dispersed in ultrapure water (gray) and with 10 mM sodium chloride bulk concentration (red).

We used a commercial dynamic light scattering (DLS) setup (Malvern, Zetasizer) to investigate particle sizes and agglomeration. The ζ-potential of the nanoparticles in an 1 mM sodium chloride solution was determined with a Malvern Zetasizer Nano-Z. The temperature for the DLS and ζ-potential measurements was 20 and 25°C, respectively.

6.5 Results and discussion

First, we want to investigate the influence of charge screening on the SHS intensity and scattering pattern of PS nanoparticles. To this end, we measured angle-resolved SHS pattern for sodium dodecyl sulfate (SDS) stabilized PS nanoparticles in ultrapure water and with 10 mM sodium chloride bulk concentration, as shown in figure 6.6. The observed non-resonant SHS signal stems mainly from interfacial water molecules, which are aligned and/or polarized by the static electric field generated by the charges at the surface of the nanoparticles.[190,191,199] The addition of 10 mM sodium chloride results in screening of the surface charge, and thus decreases the modulus of the surface potential Φ_0. According to equation 6.3, it is therefore expected that the SHS signal intensity decreases. This is in agreement with the experimental observations for scattering patterns in both *ppp* and *pss* polarization combinations and for titration of sodium chloride in the bulk solution (see figure 6.12 in section 6.7). Furthermore, from the angle-resolved SHS patterns in *ppp* po-
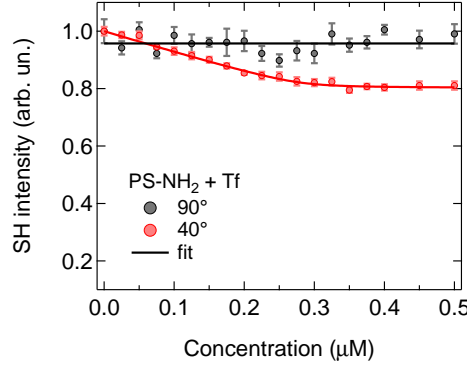
Figure 6.7: SHS intensity as a function of bulk Tf concentration for amino functionalized PS nanoparticles with 100 nm diameter, detected at 90 degrees (gray) and 40 degrees (red) scattering angle. Solid lines represent fits to the measurements.

larization combination, it is apparent that the decrease in signal intensity is more pronounced at scattering angles around 40 degrees than for 90 degrees, indicating that scattering angles close to the maximum intensity are more sensitive to charge screening than larger scattering angles ($\sim$90 degrees).

Additionally, it has been calculated in Ref. [195] that the maximum scattering intensity for PS nanoparticles with 100 nm diameter shifts towards higher scattering angles when increasing the ionic strength (for instance, 10^{-5} M of a 1:1 electrolyte) to higher ionic strength (for instance, 10^{-2} M of a 1:1 electrolyte). Bigger nanoparticles however, do not seem to be so sensitive (see figure 6.13 in section 6.7). This effect is even less pronounced for electrolytes with higher valence (see figure 6.14 in section 6.7). As can be seen from Figure 6.6, the maximum SHS intensity in *ppp* polarization combination for the nanoparticles in ultrapure water is detected at $\sim$40 degrees with respect to the incident fundamental light beam. This is at slightly higher scattering angles than that predicted from theory for low ionic strength.[195] The discrepancy between the experimental results and theory could be due to residual SDS concentration in bulk, which is already high enough to screen some of the signal contributions from the diffuse double layer.[195] Similarly, also the maximum SHS intensity in *pss* polarization combination is shifted towards higher scattering angles in the experiments as compared to theory. However, the addition of 10 mM sodium chloride into the bulk of the dispersion does not further shift the maximum SHS intensity towards higher scattering angles. These two findings, the increased sensitivity at 40 degrees scattering and no change in the shape of the scattering
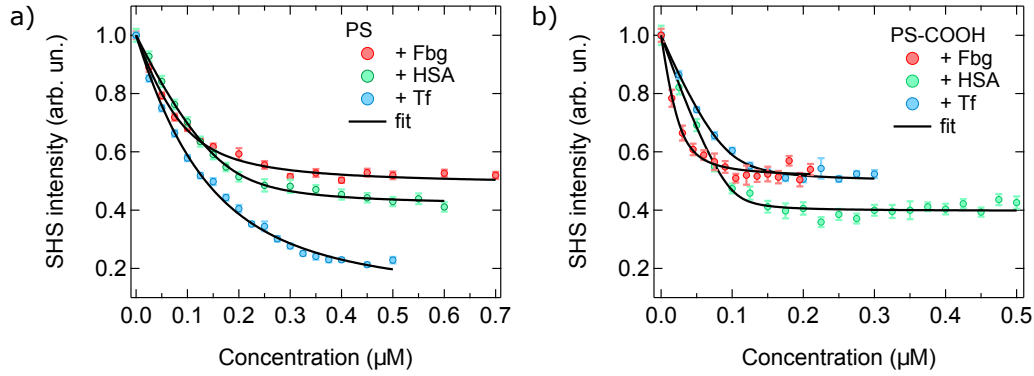
Figure 6.8: SHS intensity as a function of bulk Fbg (red), HSA (green), and Tf (blue) concentration for PS nanoparticles with 100 nm diameter. a) Plain nanoparticles with negative surface charge through residual sulfate ester from synthesis and b) with additional surface carboxyl groups.

pattern are important as they can be exploited for SHS titration experiments at 40 degrees to increase the sensitivity, while not having to worry about possible changes in the scattering pattern shape due to the addition of proteins to the solution.

In the past, SHS titration experiments on gold nanoparticles, exploiting the resonant enhancement from the localized surface plasmon, have been performed at a fixed angle of 90 degrees.[183] However, this choice can lead to a signal that is not sensitive enough to observe protein adsorption, as shown for example in figure 6.7. Here, no change in SHS intensity is observed for amino functionalized PS nanoparticles upon adsorption of Tf at 90 degrees detection, while the detected signal intensity at 40 degrees is reduced. However, whenever a change of signal intensity at 90 degrees scattering angle is observed, the data can be fitted using the same binding constant and saturation concentration as the measurements at 40 degrees detection (see figure 6.15 in section 6.7). Consequently, the same information can be retrieved from measurements at either 90 or 40 degree scattering angle, but measurements at the scattering angle with maximum SHS intensity (∼40 degrees) have an increased sensitivity.

In the next step, we performed SHS titration experiments to study the influence of the nanoparticle surface functionalization on the adsorption of various blood proteins. Figure 6.8 shows representative results for the adsorption of Fbg, HSA, and Tf on plain PS nanoparticles and PS nanoparticles with carboxy functionalization (PS-COOH). Both nanoparticle types are overall negatively charged: the plain PS due to residual sulfate esters from synthesis and the PS-COOH due to deprotona-

Table 6.1: Protein adsorption parameters retrieved from the fit of the SHS experiments. The PS and PS-COOH nanoparticles have diameters of 100 nm and were dispersed in ultrapure water. The experiments were performed at fixed detection angles of 90 or 40 degrees.

Particle & Protein	K_{app} (10^8 mol^{-1})	N_{max} (10^{-8} mol)	N_{max} per particle	ΔG^0_{app} (kJ/mol)
PS + Fbg	19 ± 5	9.8 ± 1.5	130 ± 20	$-(53.0 \pm 0.7)$
PS + HSA	34 ± 16	19 ± 1	251 ± 13	$-(54.5 \pm 1.2)$
PS + Tf	4.9 ± 1.3	14 ± 3	185 ± 40	$-(49.7 \pm 0.7)$
PS-COOH + Fbg	87 ± 51	2.9 ± 0.9	38 ± 12	$-(56.8 \pm 1.5)$
PS-COOH + HSA	270 ± 210	10 ± 0.6	132 ± 8	$-(59.6 \pm 1.9)$
PS-COOH + Tf	94 ± 39	9.9 ± 0.5	132 ± 7	$-(57.0 \pm 1.0)$

tion of the carboxylic groups at neutral pH. For both types of nanoparticles, the SHS intensity is reduced upon increase of the protein concentration in bulk solution and can be described well by the modified Langmuir adsorption model introduced in section 6.3. From the fits it is possible to obtain the saturation concentration N_{max} and the apparent binding constant K_{app} for the individual proteins adsorbing on the respective nanoparticles. The fitting results are summarized in table 6.1. Independent of the nature of the nanoparticle and the protein, we find for all measurements that the apparent Gibbs free energy is in the range of -(50-60) kJ/mol, which is similar to what has been observed for protein adsorption on gold NPs or on planar silica surfaces.[183,196] However, as mentioned in section 6.3 one has to be careful with the interpretation of these apparent values, as the process of protein adsorption is commonly more complex than described by the Langmuir model.[204] Still, the model can give useful insights with respect to the maximum amount of adsorbed protein. Here, we observe differences between the individual proteins and nanoparticles. Similar amounts of Fbg and Tf adsorb on the plain PS nanoparticles, whereas roughly twice as much HSA adsorbs. For the PS-COOH nanoparticles we observe a reduced maximum amount of adsorbed protein for all proteins. The plain and the carboxy functionalized nanoparticles possess very similar ζ-potentials of -42 and -44 mV, respectively. Therefore, this difference cannot be induced by different surface charge densities. Tf is least affected of the three proteins, where N_{max} is roughly the same for the two different types of nanoparticles. Both Fbg and HSA adsorption are more strongly affected, and the maximum number of ad-
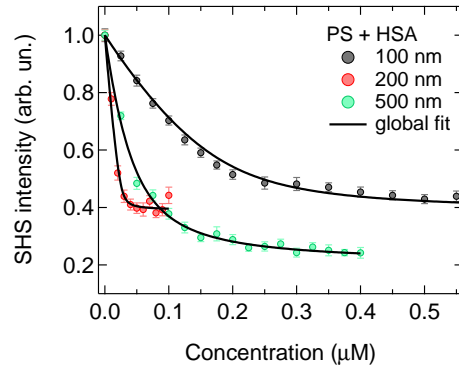
Figure 6.9: SHS intensity as a function of bulk HSA concentration for PS nanoparticles with 100 nm (gray), 200 nm (red), and 500 nm (green) diameter. The black lines represent a global fit to the data.

sorbed proteins reduces to roughly a third and half of the amount on the plain PS nanoparticles, respectively. A possible explanation for this reduction could be that the carboxy functionalization induces a different orientation of the proteins on the surface, where the individual proteins occupy more surface area. The nanoparticle dispersions are stable upon addition of the proteins, as no agglomeration is observed (see figure 6.16 in section 6.7). At pH values close to neutral all three proteins possess a net negative charge and therefore can still stabilize the nanoparticle dispersions upon adsorption. However, if immunoglobulin G (IgG) is added to the plain nanoparticles, this leads to agglomeration of the nanoparticles (see figure 6.16 in section 6.7). The reason for this is probably that IgG has an isoelectric point of ~7.5 and therefore is slightly positively charged at neutral pH. Upon adsorption, IgG neutralizes the surface charge of the nanoparticles, which in turn leads to agglomeration of the nanoparticles.

Finally, we investigate how the nanoparticle size influences the adsorption of HSA. Figure 6.9 shows the SHS signal intensity as a function of bulk HSA concentration for plain PS nanoparticles with diameters of 100 nm, 200 nm, and 500 nm, respectively. The concentration dependent SHS shows again a Langmuir like behavior. The adsorption parameters retrieved from a global fit are summarized in table 6.2. Similar to the previous measurements, the apparent Gibbs free energy for HSA adsorption is again roughly in the range from -(50-60) kJ/mol. With increasing nanoparticle diameter, also the maximum amount of adsorbed HSA increases. This is expected, as the available surface area per nanoparticle scales with the square of

Table 6.2: Protein adsorption parameters retrieved from the global fit of the SHS titration experiments. The experiments were performed at fixed detection angles of 90, 40, 35 or 25 degrees for the different nanoparticle sizes.

Particle diameter (nm)	K_{app} (10^9 mol^{-1})	N_{max} (10^{-8} mol)	N_{max} per particle	ΔG^0_{app} (kJ/mol)
100	1.96 ± 0.03	19.7 ± 8.0	261 ± 106	$-(53.10 \pm 0.04)$
200	82 ± 55	2.7 ± 0.2	1241 ± 92	$-(62.4 \pm 1.7)$
500	2.00 ± 0.03	4.3 ± 0.4	14306 ± 1331	$-(53.15 \pm 0.04)$

the diameter. However, with increasing nanoparticle diameter, the mean area per HSA on the surface of the nanoparticles decreases from 120 nm^2, over 101 nm^2, to 55 nm^2, indicating that the maximum amount of adsorbed protein increases more than the relative surface area per particle. One possible explanation for this could be differences in the surface charge densities of the nanoparticles. As discussed in section 6.3, the surface potential of the nanoparticles is linked to their charge density. Therefore, we measured the ζ-potential of the nanoparticles to obtain an estimate of the surface potential. The ζ-potentials show a normal distribution centered around -42, -50, and -54 mV for the 100, 200, and 500 nm nanoparticles with variances of 8, 7, and 8 mV, respectively. Assuming that the ζ-potential is similar to the surface potential of the nanoparticles, the resulting surface charge densities from small to large nanoparticle sizes are ~ 3.9, ~ 4.8, and ~ 5.3 mC/m^2, respectively. Consequently, the surface charge density for the nanoparticles also increases with the nanoparticle size. This increase of surface charge density seems to favor HSA adsorption. Another possible reason could be curvature of the nanoparticles. The curvature of larger nanoparticles is lower as compared to smaller nanoparticles and the lower curvature could favor HSA adsorption by enabling interaction with multiple binding sites.

6.6 Conclusions

In conclusion, we showed that non-resonant SHS can be successfully applied to observe protein adsorption on nanoparticles *in situ*, by simply exploiting the signal from the water molecules oriented by the field generated by the charges present at the surface of the nanoparticles. Not relying on resonances, such as that of

the localized surface plasmon of gold, this method has potential for widespread applications, as most colloidal nanoparticles are charge-stabilized. The sensitivity of SHS titration experiments can be increased by performing them at a fixed detection angle close to the maximum intensity of the SHS scattering pattern. Furthermore, even by using a simplified model, such as the modified Langmuir model, we were able to obtain quantitative insights on the protein adsorption and retrieve apparent binding constants and therefore the Gibbs free energy for the process. We find that the carboxy functionalization of PS nanoparticles leads to a strong decrease in the amount of adsorbed Fbg and HSA, whereas it has only minor effects on Tf. Finally, from the results on the adsorption of HSA on PS nanoparticles with different sizes, we conclude that an increasing surface charge density in combination with a slightly reduced curvature favors more HSA adsorption.

6.7 Supplementary Information

Figure 6.10 shows that the empirical function for spheres to describe the surface charge density dependent on the surface potential converges to the one for planar surfaces for high salt electrolyte concentrations or large nanoparticle radii.
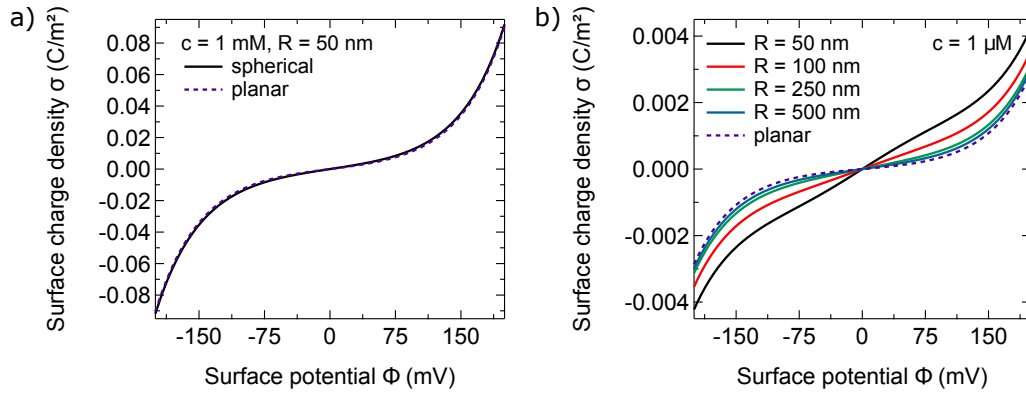

Figure 6.10: The surface charge density σ_0 as a function of the surface potential Φ_0 of the nanoparticles in comparison to the behavior at planar interfaces. a) For a 1:1 electrolyte with bulk concentration of 10^{-3} M and a nanoparticle radius of $R = 50$ nm. b) For a 1:1 electrolyte with bulk concentration of 10^{-6} M and varying nanoparticle radius.
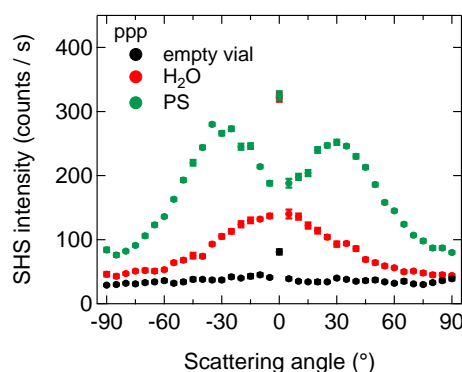
Figure 6.11: Angle-resolved non-resonant SHS pattern for a) the empty Hellma cuvette (black), b) the cuvette filled with ultrapure water (red), and c) after addition of PS nanoparticles with a diameter of 100 nm.

The walls of the quartz cuvette which is used for the SHS experiments, do not contribute to the detected SHS signal intensity, as shown in figure 6.11. The detected signal intensity for the empty cuvette is comparable to the dark counts of the detector. Upon addition of water and the nanoparticles, both the signal shape and intensity are strongly changed.

The detected SHS signal intensity decreases upon screening of the nanoparticle surface charge due to the addition of sodium chloride, as shown in figure 6.12.

Figure 6.12: SHS intensity as a function of bulk sodium chloride concentration for SDS stabilized PS nanoparticles with 100 nm diameter detected at 40 degrees scattering angle.
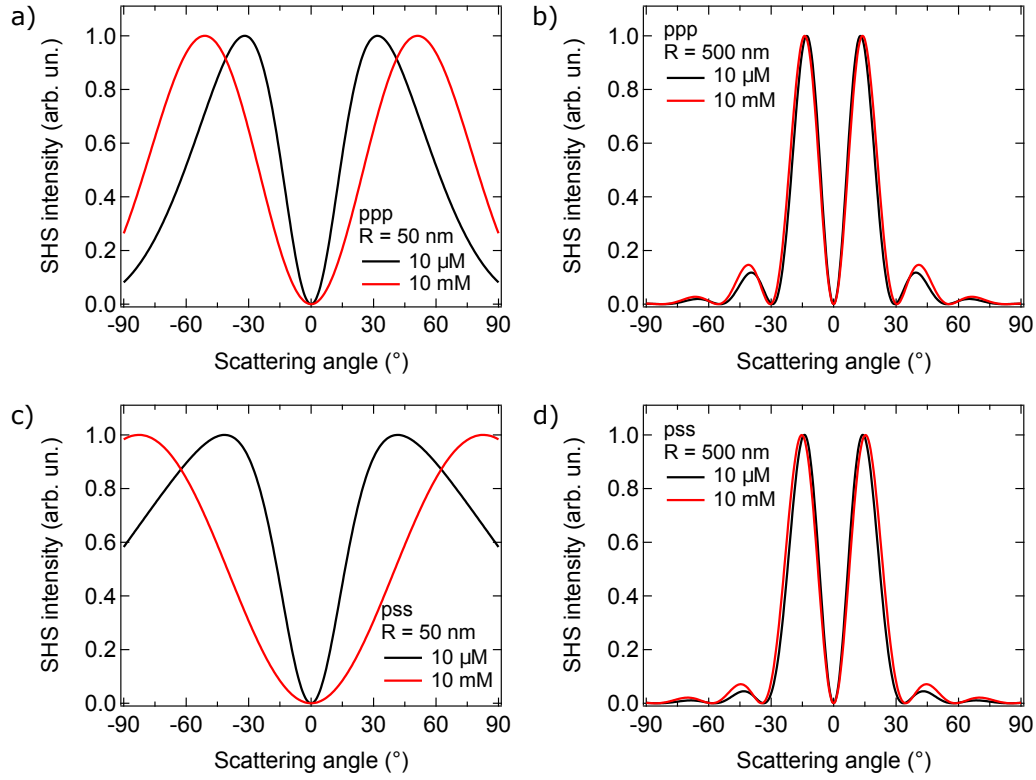
Figure 6.13: Calculated scattering patterns for a 1:1 electrolyte with 10^{-5} M (black) and 10^{-2} M (red) concentration in a-b) *ppp* and c-d) *pss* polarization combination for particles with a,c) 50 nm and b,d) 500 nm radius.

The scattering patterns in figure 6.13 were calculated according to Ref. [195]. For small nanoparticles with a radius of 50 nm, the maximum is shifted towards higher scattering angles upon increase of the electrolyte concentration. This effect is less pronounced for nanoparticles with a larger radius of 500 nm. Here, the shape of the scattering patterns is almost unchanged with increasing electrolyte concentration.
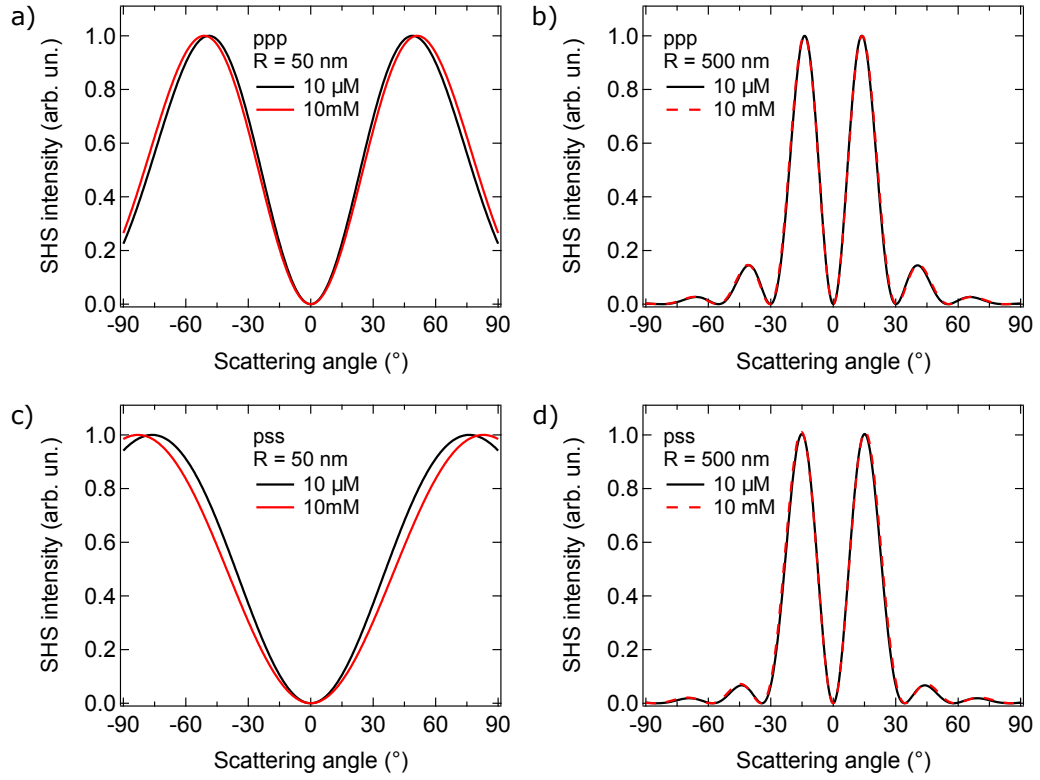
Figure 6.14: Calculated scattering patterns for a 4:4 electrolyte with 10^{-5} M (black) and 10^{-2} M (red) concentration in a-b) *ppp* and c-d) *pss* polarization combination for particles with a,c) 50 nm and b,d) 500 nm radius.

The scattering patterns in figure 6.13 were calculated according to Ref. [195]. For 4:4 electrolytes almost no change in the shape of the scattering patterns is observed even for smaller nanoparticles with a radius of 50 nm. For *pss* polarization combination a shift can still be observed, but less strong as in the case of a 1:1 electrolyte in figure 6.13. Furthermore, no change in the shape of the scattering patterns in both *ppp* and *pss* polarization combination can be observed for larger nanoparticles with a radius of 500 nm.
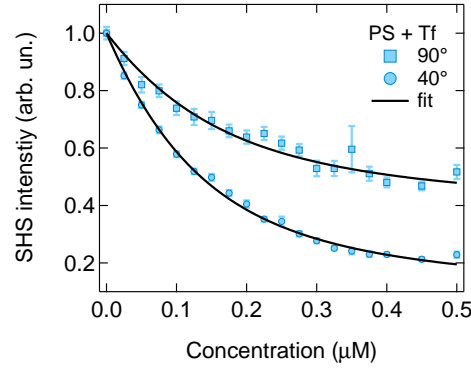
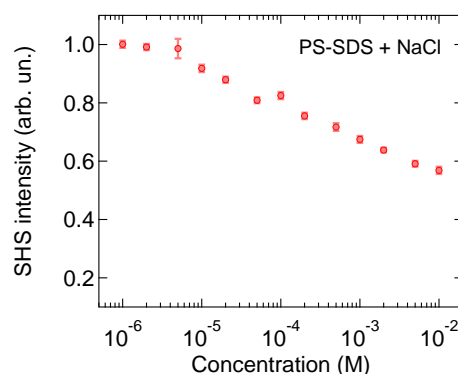**Figure 6.15:** SHS intensity as a function of bulk Tf concentration for PS nanoparticles with 100 nm diameter, detected at 90 degrees (rectangles) and 40 degrees (circles) scattering angle. Solid lines represent fits to the measurements using the same binding constant and maximum amount of protein per unit volume in the fit.

Table 6.3: Tf adsorption parameters on PS nanoparticles with 100 nm diameter retrieved from a global fit of the SHS titration experiments. The experiments were performed at fixed detection angles of 90 and 40 degrees for the different nanoparticle sizes.

Scattering angle (degrees)	A	K_{app} (10^8 mol^{-1})	N_{max} (10^{-7} mol)
90	0.39 ± 0.01	4.9 ± 1.3	1.4 ± 0.3
40	0.72 ± 0.04		

Figure 6.15 shows the SHS intensity as a function of bulk TF concentration for 100 nm diameter PS nanoparticles for detection at both 90 and 40 degrees with respect to the propagation of the fundamental beam. The experimental data can be nicely fitted using the same binding constant and maximum amount of adsorbed protein and they only differ in the amount the initial SHS signal is reduced, as indicated by the different scaling factors A in table 6.3.
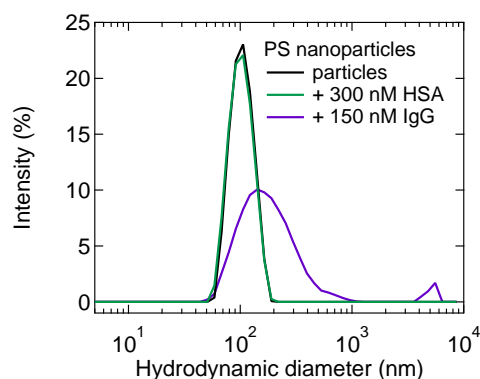
Figure 6.16: Hydrodynamic diameter of the plain 100 nm PS nanoparticles in water (black) and after addition of either 300 nM HSA (green) or 150 nM IgG (purple).

Figure 6.16 shows the determined hydrodynamic diameter from DLS measurements of the pure nanoparticles in water, and after the addition of either HSA or IgG in the solution. The pure nanoparticle dispersion shows a narrow distribution around 100 nm, as expected. Upon addition of HSA in the solution, almost no change is observed. However, the addition of IgG in the solution induces a shift toward bigger hydrodynamic diameter and an additional peak at around 5 μm appears, indicating agglomeration of the dispersion. This agglomeration upon addition of IgG is also visible to the eye, while this is not the case for all the other proteins.

7 Outlook

In this thesis, we covered two different studies of protein-nanoparticle interactions: First, planar model monolayers of protein-repelling materials at the air/water interface, and second protein adsorption on nanoparticles *in situ*. The results we presented in the previous chapters allow some new insights into the protein-repelling properties of PPEs and how protein-adsorption is influenced by surface functionalization. However, the protein corona remains the subject of ongoing research, as many questions have remaind unanswered in this field. Building on this work, there is a plethora of possible pathways that one could follow in the future to deepen the understanding of protein interactions with functionalized nanoparticle surfaces. In the following paragraphs, we will briefly present some ideas for future research projects, which could give insights on some of the open questions in this field.

Our results from chapter 3 showed that the PEG packing density influences both the repelling properties and the Fbg orientation at the surface. However, PEG has been found to trigger immunogenic reactions,[207,208] and to avoid potential side effects of PEGylated drug nanocarriers, it is thus desirable to either look for alternative materials such as the PPEs presented in chapters 4 and 5 or to reduce the degree of PEGylation on nanoparticles. Quite often, the surface chemistry of PEGylated nanoparticles is very complex as not only PEG is present on the sur-
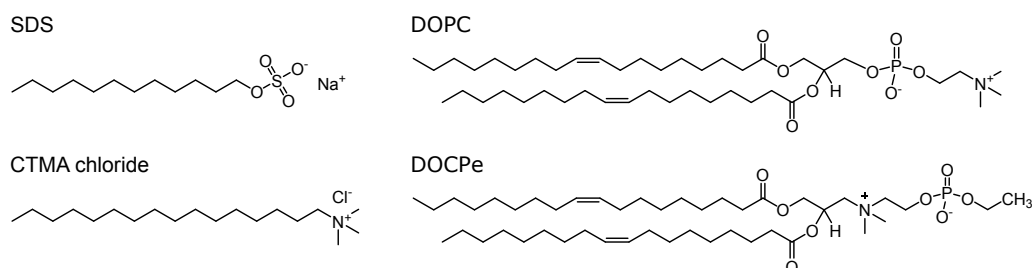

Figure 7.1: Chemical structures of SDS (top left), CTMA chloride (bottom left), DOPC (top right) and DOCPe (bottom right).

face. Other moieties are, for example, residual stabilizing surfactants left over from the synthesis, such as sodium dodecyl sulfate (SDS) and cetyltrimethylammonium (CTMA) chloride (see figure 7.1). In this context, it could be interesting to systematically study how the presence of interfacial SDS and CTMA chloride influences the protein-repelling properties. In particular, it would be interesting to investigate to what extend the degree of PEGylation can be reduced in mixed systems with SDS and/or CTMA chloride, while still preserving the protein-repelling properties.

Another open question is how interfacial water influences the protein-repelling properties of functionalized surfaces. This question has been the focus of many studies in the past where traditionally the hydrogen bonding strength of the interfacial water has been used to characterize the protein-repelling materials.[31] However, apart from that, it is not clear whether the absolute orientation of the interfacial water molecules also influences the protein-repelling properties of materials. So it would be interesting to tune the orientation of interfacial water molecules at a material surface and investigate the influence on the protein-repelling properties. Since zwitterionic materials are generally known to be good protein-repelling candidates,[3] they could offer a possible way to address the question whether the orientation of interfacial water molecules influences the protein-repelling properties of materials. Here, the zwitterionic phospolipids 1,2-dioleoyl-sn-glycero-3-phosphocholine (DOPC) and 2-((2,3-bis(oleoyloxy)propyl)dimethylammonio)ethyl phosphate (DOCPe) (see figure 7.1) could be particularly interesting. DOPC and DOCPe differ in the position of the phosphate and the choline groups within their zwitterionic headgroup and recent data have shown that they induce opposite orientation of interfacial water molecules.[209] Thus, by using these two zwitterionic phospholipids, we could tune the orientation of interfacial water molecules while keeping the rest of the system unaltered. Consequently, it would be interesting to investigate, whether DOPC and DOCPe monolayers possess different protein-repelling properties due to the different orientation of interfacial water molecules.

Additionally, nonlinear optical scattering techniques could be further exploited to improve the understanding of protein-nanoparticle interactions *in situ*. In chapter 6 we showed that it is possible to investigate protein adsorption on functionalized charged nanoparticles with non-resonant SHS. So far, the experiments were performed in ultrapure water and the logical next step would be to move towards more physi-

ologically relevant conditions, which is part of an ongoing project. Furthermore, we have seen that the surface functionalization of the nanoparticles can have a strong influence on the maximum amount of adsorbed proteins. Therefore, it is interesting to investigate how other functional groups such as amino-, sulfonate- or hydroxyl-groups at the surface of the nanoparticles influence the adsorption of blood proteins.

Apart from the huge variety of projects on the system side, there are also possible technical developments which could be utilized in future projects. In this paragraph, we would like to discuss two of them. First, it would be useful to directly probe the proteins adsorbing on the nanoparticles. So far, in chapter 6, we used non-resonant SHS as an indirect reporter on protein adsorption on nanoparticles, as it is sensitive to changes of the interfacial water molecules. Instead, SHS under resonant conditions can exploit the signal directly from the protein itself by probing the electronic transition of aromatic amino acids, for example. The development of such a novel technique is part of an ongoing project, which was started during this PhD work. Finally, another technical approach which might be of interest is sum-frequency scattering (SFS). Up to now, we have used vibrational SFG spectroscopy to investigate planar model systems and non-resonant SHS to study nanoparticle dispersions *in situ*. It would be interesting to combine these two techniques and use SFS to investigate protein adsorption on nanoparticles. SFS has the advantage that it combines the capability of a scattering technique to probe colloidal dispersions *in situ* with the chemical specificity of the vibrational SFG spectroscopy. This would enable further insights into the protein adsorption process and avoid the use of model systems. For example, on could obtain information on the changes of the protein secondary structure upon adsorption and/or information on the orientation of adsorbed proteins at the nanoparticle surface.

References

[1] Berg, J. M.; Tymoczko, J. L.; Stryer, L. *Stryer Biochemie*, 8th ed.; Springer Berlin Heidelberg: Berlin, Heidelberg, 2018.

[2] Voet, D.; Voet, J. G. *Biochemistry*, 4th ed.; John Wiley & Sons, Inc.: Hoboken, 2011.

[3] Vinet, L.; Zhedanov, A. In *Antifouling Surfaces and Materials*; Zhou, F., Ed.; Springer: Berlin, Heidelberg, 2015; Vol. 44.

[4] Nir, S.; Reches, M. *Current Opinion in Biotechnology* **2016**, *39*, 48–55.

[5] Kirschner, C. M.; Brennan, A. B. *Annual Review of Materials Research* **2012**, *42*, 211–229.

[6] Wattendorf, U.; Merkle, H. P. *Journal of Pharmaceutical Sciences* **2008**, *97*, 4655–4669.

[7] Davis, M. E.; Chen, Z. G.; Shin, D. M. *Nature Reviews Drug Discovery* **2008**, *7*, 771–782.

[8] Rahman, M.; Laurent, S.; Tawil, N.; Yahia, L.; Mahmoudi, M. *Protein-Nanoparticle Interactions*; Springer Series in Biophysics; Springer: Berlin, Heidelberg, 2013; Vol. 15.

[9] Cai, R.; Chen, C. *Advanced Materials* **2018**, 1805740.

[10] Tenzer, S.; Docter, D.; Kuharev, J.; Musyanovych, A.; Fetz, V.; Hecht, R.; Schlenk, F.; Fischer, D.; Kiouptsi, K.; Reinhardt, C.; Landfester, K.; Schild, H.; Maskos, M.; Knauer, S. K.; Stauber, R. H. *Nature Nanotechnology* **2013**, *8*, 772–781.

[11] Cedervall, T.; Lynch, I.; Lindman, S.; Berggård, T.; Thulin, E.; Nilsson, H.; Dawson, K. A.; Linse, S. *Proceedings of the National Academy of Sciences of the United States of America* **2007**, *104*, 2050–2055.

References

[12] Mahmoudi, M.; Lynch, I.; Ejtehadi, M. R.; Monopoli, M. P.; Bombelli, F. B.; Laurent, S. *Chemical Reviews* **2011**, *111*, 5610–5637.

[13] Zanganeh, S.; Spitler, R.; Erfanzadeh, M.; Alkilany, A. M.; Mahmoudi, M. *The International Journal of Biochemistry & Cell Biology* **2016**, *75*, 143–147.

[14] Salvati, A.; Pitek, A. S.; Monopoli, M. P.; Prapainop, K.; Bombelli, F. B.; Hristov, D. R.; Kelly, P. M.; Åberg, C.; Mahon, E.; Dawson, K. A. *Nature Nanotechnology* **2013**, *8*, 137–143.

[15] Lynch, I.; Dawson, K. A. *Nano Today* **2008**, *3*, 40–47.

[16] Mirshafiee, V.; Mahmoudi, M.; Lou, K.; Cheng, J.; Kraft, M. L. *Chemical Communications* **2013**, *49*, 2557.

[17] Maiolo, D.; Del Pino, P.; Metrangolo, P.; Parak, W. J.; Baldelli Bombelli, F. *Nanomedicine* **2015**, *10*, 3231–3247.

[18] Corbo, C.; Molinaro, R.; Parodi, A.; Furman, N. E. T.; Salvatore, F.; Tasciotti, E. *Nanomedicine* **2016**, *11*, 81–100.

[19] Ge, C.; Tian, J.; Zhao, Y.; Chen, C.; Zhou, R.; Chai, Z. *Archives of Toxicology* **2015**, *89*, 519–539.

[20] Pino, P. D.; Pelaz, B.; Zhang, Q.; Maffre, P.; Nienhaus, G. U.; Parak, W. J.; del Pino, P.; Nienhaus, P. D. U. *Materials Horizons* **2014**, *1*, 301–313.

[21] Walkey, C. D.; Chan, W. C. W. *Chemical Society Reviews* **2012**, *41*, 2780.

[22] Banerjee, I.; Pangule, R. C.; Kane, R. S. *Advanced Materials* **2011**, *23*, 690–718.

[23] Serrano, Â.; Sterner, O.; Mieszkin, S.; Zürcher, S.; Tosatti, S.; Callow, M. E.; Callow, J. A.; Spencer, N. D. *Advanced Functional Materials* **2013**, *23*, 5706–5718.

[24] Hucknall, A.; Rangarajan, S.; Chilkoti, A. *Advanced Materials* **2009**, *21*, 2441–2446.

[25] Schöttler, S.; Becker, G.; Winzen, S.; Steinbach, T.; Mohr, K.; Landfester, K.; Mailänder, V.; Wurm, F. R. *Nature Nanotechnology* **2016**, *11*, 372–377.

[26] Jeon, S. I.; Lee, J. H.; Andrade, J. D.; De Gennes, P. G. *Journal of Colloid and Interface Science* **1991**, *142*, 149–158.

[27] Jeon, S.; Andrade, J. *Journal of Colloid and Interface Science* **1991**, *142*, 159–166.

[28] Leckband, D.; Sheth, S.; Halperin, A. *Journal of Biomaterials Science, Polymer Edition* **1999**, *10*, 1125–1147.

[29] Harder, P.; Grunze, M.; Dahint, R.; Whitesides, G. M.; Laibinis, P. E. *The Journal of Physical Chemistry B* **1998**, *102*, 426–436.

[30] Herrwerth, S.; Eck, W.; Reinhardt, S.; Grunze, M. *Journal of the American Chemical Society* **2003**, *125*, 9359–9366.

[31] Chen, S.; Li, L.; Zhao, C.; Zheng, J. *Polymer* **2010**, *51*, 5283–5293.

[32] Steinbach, T.; Wurm, F. R. *Angewandte Chemie International Edition* **2015**, *54*, 6098–6108.

[33] Wolf, T.; Steinbach, T.; Wurm, F. R. *Macromolecules* **2015**, *48*, 3853–3863.

[34] Simon, J.; Wolf, T.; Klein, K.; Landfester, K.; Wurm, F. R.; Mailänder, V. *Angewandte Chemie International Edition* **2018**, *57*, 5548–5553.

[35] Prime, K.; Whitesides, G. *Science* **1991**, *252*, 1164–1167.

[36] Prime, K. L.; Whitesides, G. M. *Journal of the American Chemical Society* **1993**, *115*, 10714–10721.

[37] Schwierz, N.; Horinek, D.; Liese, S.; Pirzer, T.; Balzer, B. N.; Hugel, T.; Netz, R. R. *Journal of the American Chemical Society* **2012**, *134*, 19628–19638.

[38] Chapman, R. G.; Ostuni, E.; Takayama, S.; Holmlin, R. E.; Yan, L.; Whitesides, G. M. *Journal of the American Chemical Society* **2000**, *122*, 8303–8304.

[39] Ostuni, E.; Chapman, R. G.; Holmlin, R. E.; Takayama, S.; Whitesides, G. M. *Langmuir* **2001**, *17*, 5605–5620.

[40] Li, L.; Chen, S.; Zheng, J.; Ratner, B. D.; Jiang, S. *The Journal of Physical Chemistry B* **2005**, *109*, 2934–2941.

References

[41] de Gennes, P. G. *Macromolecules* **1980**, *13*, 1069–1075.

[42] de Gennes, P. *Advances in Colloid and Interface Science* **1987**, *27*, 189–209.

[43] McPherson, T.; Kidane, A.; Szleifer, I.; Park, K. *Langmuir* **1998**, *14*, 176–186.

[44] Marsh, D.; Bartucci, R.; Sportelli, L. *Biochimica et Biophysica Acta (BBA) - Biomembranes* **2003**, *1615*, 33–59.

[45] Brittain, W. J.; Minko, S. *Journal of Polymer Science Part A: Polymer Chemistry* **2007**, *45*, 3505–3512.

[46] Alexander, S. *Journal de Physique* **1977**, *38*, 983–987.

[47] Lee, H.; Larson, R. G. *Biomacromolecules* **2016**, *17*, 1757–1765.

[48] Pauling, L.; Corey, R. B.; Branson, H. R. *Proceedings of the National Academy of Sciences of the United States of America* **1951**, *37*, 205–211.

[49] Pauling, L.; Corey, R. B. *Proceedings of the National Academy of Sciences of the United States of America* **1951**, *37*, 251–256.

[50] Buxbaum, E. *Fundamentals of Protein Structure and Function*, 2nd ed.; Springer International Publishing: Cham, 2015.

[51] Thomas, G. J. *Annual Review of Biophysics and Biomolecular Structure* **1999**, *28*, 1–27.

[52] Barth, A.; Zscherp, C. *Quarterly Reviews of Biophysics* **2002**, *35*, 369–430.

[53] Barth, A. *Biochimica et Biophysica Acta (BBA) - Bioenergetics* **2007**, *1767*, 1073–1101.

[54] Parson, W. W. *Modern Optical Spectroscopy*, 2nd ed.; Springer: Berlin, Heidelberg, 2015.

[55] Boyd, R. W. *Nonlinear Optics*, 3rd ed.; Academic Press/Elsevier: Amsterdam, 2008.

[56] Shen, Y. R. *Fundamentals of Sum-Frequency Spectroscopy*; Cambridge University Press: Cambridge, 2016.

[57] Lambert, A. G.; Davies, P. B.; Neivandt, D. J. *Applied Spectroscopy Reviews* **2005**, *40*, 103–145.

[58] Franken, P. A.; Hill, A. E.; Peters, C. W.; Weinreich, G. *Physical Review Letters* **1961**, *7*, 118–119.

[59] Maiman, T. H. *Nature* **1960**, *187*, 493–494.

[60] Zhu, X. D.; Suhr, H.; Shen, Y. R. *Physical Review B* **1987**, *35*, 3047–3050.

[61] Zhuang, X.; Miranda, P.; Kim, D.; Shen, Y. *Physical Review B* **1999**, *59*, 12632–12640.

[62] Nguyen, K. T.; Le Clair, S. V.; Ye, S.; Chen, Z. *The Journal of Physical Chemistry B* **2009**, *113*, 12169–12180.

[63] Shen, Y. R. *The principles of nonlinear optics*; Wiley: New York, 1984.

[64] Guyot-Sionnest, P.; Shen, Y. R. *Physical Review B* **1987**, *35*, 4420–4426.

[65] Yamaguchi, S.; Shiratori, K.; Morita, A.; Tahara, T. *The Journal of Chemical Physics* **2011**, *134*, 184705.

[66] Vogel, V.; Smiley, B. L. Molecular assemblies at liquid interfaces probed by optical second harmonic generation. SPIE Vol. 1922. 1992.

[67] Eisenthal, K. B. *Chemical Reviews* **1996**, *96*, 1343–1360.

[68] Tran, R. J.; Sly, K. L.; Conboy, J. C. *Annual Review of Analytical Chemistry* **2017**, *10*.

[69] Ong, S.; Zhao, X.; Eisenthal, K. B. *Chemical Physics Letters* **1992**, *191*, 327–335.

[70] Geiger, F. M. *Annual Review of Physical Chemistry* **2009**, *60*, 61–83.

[71] Ohno, P. E.; Saslow, S. A.; Wang, H.-f.; Geiger, F. M.; Eisenthal, K. B. *Nature Communications* **2016**, *7*, 13587.

[72] Wang, H.; Yan, E.; Borguet, E.; Eisenthal, K. *Chemical Physics Letters* **1996**, *259*, 15–20.

[73] Eisenthal, K. B. *Chemical Reviews* **2006**, *106*, 1462–1477.

References

[74] Roke, S.; Gonella, G. *Annual Review of Physical Chemistry* **2012**, *63*, 353–378.

[75] Clays, K.; Persoons, A. *Review of Scientific Instruments* **1992**, *63*, 3285–3289.

[76] Dadap, J. I.; Shan, J.; Heinz, T. F. *Journal of the Optical Society of America B* **2004**, *21*, 1328.

[77] Roke, S.; Bonn, M.; Petukhov, A. V. *Physical Review B* **2004**, *70*, 115106.

[78] de Beer, A. G. F.; Roke, S. *Physical Review B* **2009**, *79*, 155420.

[79] Jen, S.-H.; Dai, H.-L.; Gonella, G. *The Journal of Physical Chemistry C* **2010**, *114*, 4302–4308.

[80] de Beer, A. G. F.; Roke, S. *The Journal of Chemical Physics* **2010**, *132*, 234702.

[81] Gonella, G.; Dai, H.-L. *Physical Review B* **2011**, *84*, 121402.

[82] Gonella, G.; Dai, H. L. *Langmuir* **2014**, *30*, 2588–2599.

[83] Backus, E. H. G.; Bonn, D.; Cantin, S.; Roke, S.; Bonn, M. *The Journal of Physical Chemistry B* **2012**, *116*, 2703–2712.

[84] Gomopoulos, N.; Lütgebaucks, C.; Sun, Q.; Macias-Romero, C.; Roke, S. *Optics Express* **2013**, *21*, 815.

[85] Lütgebaucks, C. U. Lipid membrane characterization with second harmonic scattering: surface potentials, ionization, membrane asymmetry and hydration. Ph.D. thesis, École Polytechnique Fédérale de Lausanne, 2017.

[86] Hoenig, D.; Moebius, D. *The Journal of Physical Chemistry* **1991**, *95*, 4590–4592.

[87] Hénon, S.; Meunier, J. *Review of Scientific Instruments* **1991**, *62*, 936–939.

[88] Lheveder, C.; Meunier, J.; Hénon, S. In *Physical chemistry of biological interfaces*; Baszkin, A., Norde, W., Eds.; Dekker: New York; Basel, 2000; Chapter Brewster Angle Microscopy.

[89] Azzam, R. M. A.; Bashara, N. M. *Ellipsometry and polarized light*; North-Holland Publishing Company: Amsterdam - New York - Oxford, 1977.

[90] de Mul, M. N. G.; Mann, J. A. *Langmuir* **1998**, *14*, 2455–2466.

[91] Rodríguez Patino, J. M.; Sánchez, C. C.; Rodríguez Niño, M. R. *Langmuir* **1999**, *15*, 2484–2492.

[92] Winsel, K.; Hönig, D.; Lunkenheimer, K.; Geggel, K.; Witt, C. *European Biophysics Journal* **2003**, *32*, 544–552.

[93] Adamson, A. W.; Gast, A. P. *Physical Chemistry of Surfaces*, 6th ed.; John Wiley & Sons, Inc.: New York, 1997.

[94] Butt, H.-J.; Graf, K.; Kappl, M. *Physics and Chemistry of Interfaces*; Wiley-VCH GmbH & Co. KGaA: Weinheim, 2003.

[95] Magin, C. M.; Cooper, S. P.; Brennan, A. B. *Materials Today* **2010**, *13*, 36–44.

[96] Solano, I.; Parisse, P.; Gramazio, F.; Cavalleri, O.; Bracco, G.; Castronovo, M.; Casalis, L.; Canepa, M. *Phys. Chem. Chem. Phys.* **2015**, *17*, 28774–28781.

[97] Chen, S.; Zheng, J.; Li, L.; Jiang, S. *Journal of the American Chemical Society* **2005**, *127*, 14473–14478.

[98] Ma, H.; Hyun, J.; Stiller, P.; Chilkoti, A. *Advanced Materials* **2004**, *16*, 338–341.

[99] Du, H.; Chandaroy, P.; Hui, S. W. *Biochimica et Biophysica Acta (BBA) - Biomembranes* **1997**, *1326*, 236–248.

[100] Price, M. E.; Cornelius, R. M.; Brash, J. L. *Biochimica et Biophysica Acta (BBA) - Biomembranes* **2001**, *1512*, 191–205.

[101] Michel, R.; Pasche, S.; Textor, M.; Castner, D. G. *Langmuir* **2005**, *21*, 12327–12332.

[102] Gon, S.; Santore, M. M. *Langmuir* **2011**, *27*, 1487–1493.

[103] Hu, Y.; Jin, J.; Han, Y.; Yin, J.; Jiang, W.; Liang, H. *RSC Advances* **2014**, *4*, 7716.

[104] Jin, J.; Jiang, W.; Yin, J.; Ji, X.; Stagnaro, P. *Langmuir* **2013**, *29*, 6624–6633.

[105] Welch, N. G.; Scoble, J. A.; Muir, B. W.; Pigram, P. J. *Biointerphases* **2017**, *12*, 02D301.

References

[106] Weidner, T.; Castner, D. G. *Physical Chemistry Chemical Physics* **2013**, *15*, 12516.

[107] Roy, S.; Covert, P. A.; FitzGerald, W. R.; Hore, D. K. *Chemical Reviews* **2014**, *114*, 8388–8415.

[108] Leng, C.; Hung, H.-C.; Sun, S.; Wang, D.; Li, Y.; Jiang, S.; Chen, Z. *ACS Applied Materials & Interfaces* **2015**, *7*, 16881–16888.

[109] Stein, M. J.; Weidner, T.; McCrea, K.; Castner, D. G.; Ratner, B. D. *The Journal of Physical Chemistry B* **2009**, *113*, 11550–11556.

[110] Wang, R. Y.; Himmelhaus, M.; Fick, J.; Herrwerth, S.; Eck, W.; Grunze, M. *The Journal of Chemical Physics* **2005**, *122*, 164702.

[111] Zolk, M.; Eisert, F.; Pipper, J.; Herrwerth, S.; Eck, W.; Buck, M.; Grunze, M. *Langmuir* **2000**, *16*, 5849–5852.

[112] Leng, C.; Sun, S.; Zhang, K.; Jiang, S.; Chen, Z. *Acta Biomaterialia* **2016**, *40*, 6–15.

[113] Leung, B. O.; Yang, Z.; Wu, S. S. H.; Chou, K. C. *Langmuir* **2012**, *28*, 5724–5728.

[114] Leng, C.; Hung, H.-C.; Sieggreen, O. A.; Li, Y.; Jiang, S.; Chen, Z. *The Journal of Physical Chemistry C* **2015**, *119*, 8775–8780.

[115] Tyrode, E.; Johnson, C. M.; Rutland, M. W.; Claesson, P. M. *The Journal of Physical Chemistry C* **2007**, *111*, 11642–11652.

[116] Wang, J.; Even, M. A.; Chen, X.; Schmaier, A. H.; Waite, J. H.; Chen, Z. *Journal of the American Chemical Society* **2003**, *125*, 9914–9915.

[117] Clarke, M. L.; Wang, J.; Chen, Z. *The Journal of Physical Chemistry B* **2005**, *109*, 22027–22035.

[118] Chen, X.; Wang, J.; Sniadecki, J. J.; Even, M. A.; Chen, Z. *Langmuir* **2005**, *21*, 2662–2664.

[119] Fu, L.; Liu, J.; Yan, E. C. Y. *Journal of the American Chemical Society* **2011**, *133*, 8094–8097.

[120] Ge, A.; Seo, J.-H.; Qiao, L.; Yui, N.; Ye, S. *ACS Applied Materials & Interfaces* **2015**, *7*, 22709–22718.

[121] Kim, J.; Cremer, P. S. *ChemPhysChem* **2001**, *2*, 543–546.

[122] Kim, G.; Gurau, M.; Kim, J.; Cremer, P. S. *Langmuir* **2002**, *18*, 2807–2811.

[123] Franz, J.; van Zadel, M.-J.; Weidner, T. *Review of Scientific Instruments* **2017**, *88*, 053106.

[124] Kuhl, T.; Leckband, D.; Lasic, D.; Israelachvili, J. *Biophysical Journal* **1994**, *66*, 1479–1488.

[125] Majewski, J.; Kuhl, T. L.; Gerstenberg, M. C.; Israelachvili, J. N.; Smith, G. S. *The Journal of Physical Chemistry B* **1997**, *101*, 3122–3129.

[126] Ohe, C.; Goto, Y.; Noi, M.; Arai, M.; Kamijo, H.; Itoh, K. *The Journal of Physical Chemistry B* **2007**, *111*, 1693–1700.

[127] Shahid, M. N.; Tsoukanova, V. *The Journal of Physical Chemistry B* **2011**, *115*, 3303–3314.

[128] Protein data bank (PDB) entry 4F5S. `http://www.rcsb.org`, accessed: 2019-03-03.

[129] Singh, B. *Infrared Analysis of Peptides and Proteins*; American Chemical Society: Washington D.C., 2000.

[130] Stepniewski, M.; Pasenkiewicz-Gierula, M.; Róg, T.; Danne, R.; Orlowski, A.; Karttunen, M.; Urtti, A.; Yliperttula, M.; Vuorimaa, E.; Bunker, A. *Langmuir* **2011**, *27*, 7788–7798.

[131] Protein data bank (PDB) entry 3GHG. `http://www.rcsb.org`, accessed: 2019-03-03.

[132] Köhler, S.; Schmid, F.; Settanni, G. *PLOS Computational Biology* **2015**, *11*, e1004346.

[133] Roeters, S. J.; Van Dijk, C. N.; Torres-Knoop, A.; Backus, E. H. G.; Campen, R. K.; Bonn, M.; Woutersen, S. *Journal of Physical Chemistry A* **2013**, *117*, 6311–6322.

References

[134] Hennig, R.; Heidrich, J.; Saur, M.; Schmüser, L.; Roeters, S. J.; Hellmann, N.; Woutersen, S.; Bonn, M.; Weidner, T.; Markl, J.; Schneider, D. *Nature Communications* **2015**, *6*, 7018.

[135] Weisel, J. In *Advances in Protein Chemistry*; Richardss, F. M., Eisenberg, D. S., Kuriyan, J., Eds.; Elsevier Academic Press: San Diego, London, 2005; pp 247–299.

[136] Bundesärztekammer, *Transfusion Medicine and Hemotherapy*; S. Karger AG: Freiburg, 2009; Vol. 36; pp 399–407.

[137] Meister, K.; Roeters, S. J.; Paananen, A.; Woutersen, S.; Versluis, J.; Szilvay, G. R.; Bakker, H. J. *The Journal of Physical Chemistry Letters* **2017**, *8*, 1772–1776.

[138] Hamm, P.; Lim, M.; DeGrado, W. F.; Hochstrasser, R. M. *Proceedings of the National Academy of Sciences* **1999**, *96*, 2036–2041.

[139] Humphrey, W.; Dalke, A.; Schulten, K. *Journal of Molecular Graphics* **1996**, *14*, 33–38.

[140] Gericke, A.; Flach, C.; Mendelsohn, R. *Biophysical Journal* **1997**, *73*, 492–499.

[141] Knop, K.; Hoogenboom, R.; Fischer, D.; Schubert, U. S. *Angewandte Chemie International Edition* **2010**, *49*, 6288–6308.

[142] Herzberger, J.; Niederer, K.; Pohlit, H.; Seiwert, J.; Worm, M.; Wurm, F. R.; Frey, H. *Chemical Reviews* **2016**, *116*, 2170–2243.

[143] Bauer, K. N.; Tee, H. T.; Velencoso, M. M.; Wurm, F. R. *Progress in Polymer Science* **2017**, *73*, 61–122.

[144] Müller, J.; Bauer, K.; Prozeller, D.; Simon, J.; Mailänder, V.; Wurm, F.; Winzen, S.; Landfester, K. *Biomaterials* **2017**, *115*, 1–8.

[145] Yang, W. J.; Neoh, K.-G.; Kang, E.-T.; Teo, S. L.-M.; Rittschof, D. *Progress in Polymer Science* **2014**, *39*, 1017–1042.

[146] Jung, S.-Y.; Lim, S.-M.; Albertorio, F.; Kim, G.; Gurau, M. C.; Yang, R. D.; Holden, M. A.; Cremer, P. S. *Journal of the American Chemical Society* **2003**, *125*, 12782–12786.

[147] Tyrode, E.; Johnson, C. M.; Kumpulainen, A.; Rutland, M. W.; Claesson, P. M. *Journal of the American Chemical Society* **2005**, *127*, 16848–16859.

[148] Schmüser, L.; Roeters, S.; Lutz, H.; Woutersen, S.; Bonn, M.; Weidner, T. *The Journal of Physical Chemistry Letters* **2017**, *8*, 3101–3105.

[149] Yan, E. C. Y.; Fu, L.; Wang, Z.; Liu, W. *Chemical Reviews* **2014**, *114*, 8471–8498.

[150] Ding, B.; Jasensky, J.; Li, Y.; Chen, Z. *Accounts of Chemical Research* **2016**, *49*, 1149–1157.

[151] Braunschweig, B.; Mukherjee, P.; Kutz, R. B.; Rumpel, A.; Engelhardt, K.; Peukert, W.; Dlott, D. D.; Wieckowski, A. *Vibrational Spectroscopy at Electrified Interfaces*; John Wiley & Sons, Inc.: Hoboken, NJ, USA, 2013.

[152] Haupert, L. M.; Simpson, G. J. *Annual Review of Physical Chemistry* **2009**, *60*, 345–365.

[153] Yan, E. C. Y.; Wang, Z.; Fu, L. *The Journal of Physical Chemistry B* **2015**, *119*, 2769–2785.

[154] Chen, X.; Hua, W.; Huang, Z.; Allen, H. C. *Journal of American Chemical Society* **2010**, *132*, 11336–11342.

[155] Bauer, K. N.; Liu, L.; Andrienko, D.; Wagner, M.; Macdonald, E. K.; Shaver, M. P.; Wurm, F. R. *Macromolecules* **2018**, *51*, 1272–1279.

[156] Bernhard, C.; Roeters, S. J.; Franz, J.; Weidner, T.; Bonn, M.; Gonella, G. *Phys. Chem. Chem. Phys.* **2017**, *19*, 28182–28188.

[157] Protein data bank (PDB) entry 1AO6. http://www.rcsb.org, accessed: 2019-03-03.

[158] Sovago, M.; Campen, R. K.; Wurpel, G. W. H.; Müller, M.; Bakker, H. J.; Bonn, M. *Physical Review Letters* **2008**, *100*, 173901.

[159] Schaefer, J.; Backus, E. H.; Nagata, Y.; Bonn, M. *Journal of Physical Chemistry Letters* **2016**, *7*, 4591–4595.

[160] Nagasawa, D.; Azuma, T.; Noguchi, H.; Uosaki, K.; Takai, M. *The Journal of Physical Chemistry C* **2015**, *119*, 17193–17201.

References

[161] Becker, G.; Marquetant, T. A.; Wagner, M.; Wurm, F. R. *Macromolecules* **2017**, *50*, 7852–7862.

[162] Bauer, K. In-Chain Poly (phosphonate)s: Synthesis, Degradation and Biomedical Applications. Ph.D. thesis, Johannes Gutenberg-Universität Mainz, 2017.

[163] Bhakta, S. A.; Evans, E.; Benavidez, T. E.; Garcia, C. D. *Analytica Chimica Acta* **2015**, *872*, 7–25.

[164] Kirsch, J.; Siltanen, C.; Zhou, Q.; Revzin, A.; Simonian, A. *Chemical Society Reviews* **2013**, *42*, 8733.

[165] Howes, P. D.; Chandrawati, R.; Stevens, M. M. *Science* **2014**, *346*, 1247390–1247390.

[166] Trilling, A. K.; Beekwilder, J.; Zuilhof, H. *Analyst* **2013**, *138*, 1619–1627.

[167] Lin, P. C.; Weinrich, D.; Waldmann, H. *Macromolecular Chemistry and Physics* **2010**, *211*, 136–144.

[168] Jonkheijm, P.; Weinrich, D.; Schröder, H.; Niemeyer, C. M.; Waldmann, H. *Angewandte Chemie - International Edition* **2008**, *47*, 9618–9647.

[169] Tonigold, M.; Simon, J.; Estupiñán, D.; Kokkinopoulou, M.; Reinholz, J.; Kintzel, U.; Kaltbeitzel, A.; Renz, P.; Domogalla, M. P.; Steinbrink, K.; Lieberwirth, I.; Crespy, D.; Landfester, K.; Mailänder, V. *Nature Nanotechnology* **2018**, *13*, 862–869.

[170] Blankenburg, J.; Maciol, K.; Hahn, C.; Frey, H. *Macromolecules* **2019**, *52*, 1785–1793.

[171] Bernhard, C.; Bauer, K. N.; Bonn, M.; Wurm, F. R.; Gonella, G. *ACS Applied Materials & Interfaces* **2019**, *11*, 1624–1629.

[172] Eisele, K.; Gropeanu, R. A.; Zehendner, C. M.; Rouhanipour, A.; Ramanathan, A.; Mihov, G.; Koynov, K.; Kuhlmann, C. R.; Vasudevan, S. G.; Luhmann, H. J.; Weil, T. *Biomaterials* **2010**, *31*, 8789–8801.

[173] Yan, E.; Ding, Y.; Chen, C.; Li, R.; Hu, Y.; Jiang, X. *Chemical Communications* **2009**, 2718.

[174] Barrett, A.; Imbrogno, J.; Belfort, G.; Petersen, P. B. *Langmuir* **2016**, *32*, 9074–9082.

[175] Köhler, S.; Schmid, F.; Settanni, G. *Langmuir* **2015**, *31*, 13180–13190.

[176] Protopopova, A. D.; Barinov, N. A.; Zavyalova, E. G.; Kopylov, A. M.; Sergienko, V. I.; Klinov, D. V. *Journal of Thrombosis and Haemostasis* **2015**, *13*, 570–579.

[177] Roke, S.; Roeterdink, W. G.; Wijnhoven, J. E. G. J.; Petukhov, A. V.; Kleyn, A. W.; Bonn, M. *Physical Review Letters* **2003**, *91*, 258302.

[178] Gan, W.; Gonella, G.; Zhang, M.; Dai, H. L. *Journal of Chemical Physics* **2011**, *134*, 5–8.

[179] Haber, L. H.; Kwok, S. J.; Semeraro, M.; Eisenthal, K. B. *Chemical Physics Letters* **2011**, *507*, 11–14.

[180] Gan, W.; Xu, B.; Dai, H.-L. *Angewandte Chemie International Edition* **2011**, *50*, 6622–6625.

[181] Gonella, G.; Gan, W.; Xu, B.; Dai, H. L. *Journal of Physical Chemistry Letters* **2012**, *3*, 2877–2881.

[182] Xu, B.; Gonella, G.; DeLacy, B. G.; Dai, H.-L. *The Journal of Physical Chemistry C* **2015**, *119*, 5656–5461.

[183] Das, A.; Chakrabarti, A.; Das, P. K. *Phys. Chem. Chem. Phys.* **2016**, *18*, 24325–24331.

[184] Wang, H.; Yan, E. C. Y.; Liu, Y.; Eisenthal, K. B. *The Journal of Physical Chemistry B* **1998**, *102*, 4446–4450.

[185] Wang, H.; Troxler, T.; Yeh, A.-G.; Dai, H.-L. *Langmuir* **2000**, *16*, 2475–2481.

[186] Yang, N.; Angerer, W. E.; Yodh, A. G. *Physical Review Letters* **2001**, *87*, 103902.

[187] Eckenrode, H. M.; Dai, H.-L. *Langmuir* **2004**, *20*, 9202–9209.

[188] Schneider, L.; Schmid, H.; Peukert, W. *Applied Physics B* **2007**, *87*, 333–339.

References

[189] Jen, S.-H.; Gonella, G.; Dai, H.-L. *The Journal of Physical Chemistry A* **2009**, *113*, 4758–4762.

[190] Yan, E. C. Y.; Liu, Y.; Eisenthal, K. B. *The Journal of Physical Chemistry B* **1998**, *102*, 6331–6336.

[191] Liu, Y.; Yan, E. C. Y.; Zhao, X.; Eisenthal, K. B. *Langmuir* **2001**, *17*, 2063–2066.

[192] Sauerbeck, C.; Braunschweig, B.; Peukert, W. *The Journal of Physical Chemistry C* **2014**, *118*, 10033–10042.

[193] Lütgebaucks, C.; Gonella, G.; Roke, S. *Physical Review B* **2016**, *94*, 195410.

[194] Lütgebaucks, C.; Macias-Romero, C.; Roke, S. *Journal of Chemical Physics* **2017**, *146*.

[195] Gonella, G.; Lütgebaucks, C.; de Beer, A. G. F.; Roke, S. *The Journal of Physical Chemistry C* **2016**, *120*, 9165–9173.

[196] Salafsky, J. S.; Eisenthal, K. B. *The Journal of Physical Chemistry B* **2000**, *104*, 7752–7755.

[197] Troiano, J. M.; McGeachy, A. C.; Olenick, L. L.; Fang, D.; Liang, D.; Hong, J.; Kuech, T. R.; Caudill, E. R.; Pedersen, J. A.; Cui, Q.; Geiger, F. M. *Journal of the American Chemical Society* **2017**, *139*, 5808–5816.

[198] Bersohn, R.; Pao, Y.-H.; Frisch, H. *The Journal of Chemical Physics* **1966**, *45*, 3184.

[199] Schürer, B.; Wunderlich, S.; Sauerbeck, C.; Peschel, U.; Peukert, W. *Physical Review B* **2010**, *82*, 241404.

[200] Dreier, L. B.; Bernhard, C.; Gonella, G.; Backus, E. H. G.; Bonn, M. *The Journal of Physical Chemistry Letters* **2018**, 5685–5691.

[201] Wen, Y. C.; Zha, S.; Liu, X.; Yang, S.; Guo, P.; Shi, G.; Fang, H.; Shen, Y. R.; Tian, C. *Physical Review Letters* **2016**, *116*, 1–5.

[202] de Beer, A. G. F.; Roke, S. *Physical Review B* **2007**, *75*, 1–8.

[203] Ohshima, H., Ed. *Theory of Colloid and Interfacial Electric Phenomena*, 1st ed.; Academic Press: Tokyo, 2006; Vol. 12.

[204] Latour, R. A. *Journal of biomedical materials research. Part A* **2015**, *103*, 949–58.

[205] Ramsden, J. J. *Chemical Society Reviews* **1995**, *24*, 73.

[206] Rabe, M.; Verdes, D.; Seeger, S. *Advances in Colloid and Interface Science* **2011**, *162*, 87–106.

[207] Ishida, T.; Maeda, R.; Ichihara, M.; Irimura, K.; Kiwada, H. *Journal of Controlled Release* **2003**, *88*, 35–42.

[208] Tagami, T.; Uehara, Y.; Moriyoshi, N.; Ishida, T.; Kiwada, H. *Journal of Controlled Release* **2011**, *151*, 149–154.

[209] Dreier, L. B. Spectroscopic Studies of Water at Charged Interfaces. Ph.D. thesis, Johannes Gutenberg-Universität Mainz, 2018.

Acknowledgements

This section is not included in this version.